Charles University in Prague

Faculty of Mathematics and Physics

MASTER THESIS

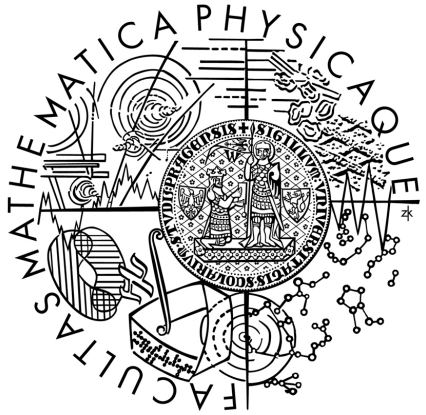

Radomír Chabiniok

Cardiac MRI Data Segmentation Using the Partial Differential Equation of Allen–Cahn Type

Mathematical Institute of Charles University

Supervisor: Doc. Dr. Ing Michal Beneš

Study branch: Mathematical and Computer Modeling in Physics and Engineering

This work was supported by the project MŠMT LC06052 (Nečas Center for Mathematical Modeling) and by grants MŠMT 1M6798582302, MZO 00023001, Czech Republic. The author thanks to the supervisor doc. Dr. Ing. Michal Beneš for fruitful discussions, to Ing. Jaroslav Tintěra, CSc. for introduction to cardiac MRI, to MR departments of hospitals Na Homolce Prague, IKEM Prague and Hradec Králové for providing MR image data and to the French government for funding a short stay in France.

I confirm having prepared the master thesis by my own, and having listed all used sources of information in the bibliography. I agree with lending the master thesis.

In Prague, April 19, 2007 Radomír Chabiniok

Contents

Název práce: Zpracování dat cardiac MRI pomocí parciální diferenciální rovnice Allenova–Cahnova typu
Autor: Radomír Chabiniok
Ústav: Matematický ústav Univerzity Karlovy
Vedoucí práce: doc. Dr. Ing. Michal Beneš, Katedra matematiky, Fakulta jaderná a fyzikálně inženýrská, České vysoké učení technické v Praze
e-mail vedoucího: benes@kmlinux.fjfi.cvut.cz
Konzultant: Ing. Jaroslav Tintěra, CSc., Základna radiodiagnostiky a intervenční radiologie, Institut klinické a experimentální medicíny, Praha
Abstrakt: Práce je věnována úloze segmentace obrazových dat pomocí algoritmu založeném na numerickém řešení geometrické evoluční parciální diferenciální rovnice Allenova–Cahnova typu. Tato rovnice pochází z popisu pohybu fázových rozhraní na základě interakce jejich normálové rychlosti a křivosti a má difúzní charakter. Difúzní proces lze řídit pomocí segmentovaného signálu a docílit tak odhalení hran hledaných objektů nebo oblastí. Zásadní částí práce je praktická aplikace metody při automatické segmentaci levé srdeční komory z posloupnosti obrazů, získaných pomocí zobrazování srdce magnetickou rezonancí (cardiac MRI), s následnou interpretací její dynamiky.
Klíčová slova: zpracování obrazu, segmentace, PDR, Allen-Cahn, cardiac MRI

Title: Cardiac MRI Data Segmentation Using the Partial Differential Equation of Allen–Cahn Type
Author: Radomír Chabiniok
Department: Mathematical Institute of Charles University, Prague
Supervisor: doc. Dr. Ing. Michal Beneš, Department of Mathematics, Faculty of Nuclear Sciences and Physical Engineering, Czech Technical University in Prague
Supervisor's e-mail address: benes@kmlinux.fjfi.cvut.cz
Consultant: Ing. Jaroslav Tintěra, CSc., Department of Diagnostic and Interventional Radiology, Institute for Clinical and Experimental Medicine, Prague
Abstract: The work deals with segmentation of image data using the algorithm based on numerical solution of the geometrical evolution partial differential equation of the Allen-Cahn type. This equation has origin in the description of motion by mean curvature and has diffusive character. The diffusion process can be controlled by the segmented signal so that the edges of the objects or areas can be found. The method is applied to the problem of automated segmentation of the left heart ventricle from the cardiac MRI images with the subsequent interpretation of its dynamics.
Keywords: image processing, segmentation, PDE, Allen-Cahn equation, cardiac MRI

Chapter 1

Introduction

1.1 Digital image processing

The presented work is motivated by the need of the radiological department of the hospital IKEM Prague (see [16]) for evaluation of the dynamical images of the heart obtained by the magnetic resonance imaging (cardiac MRI). One of important aims of cardiac MRI examination is estimation of parameters reflecting current clinical state of patients. These parameters should be measurable in a reproducible way so that progress of a disease can be observed. A typical example could be accurate measurement of heart ventricle volumes during the heart contraction that reflect the contractive ability of the myocardium[1]. In this approach, it is necessary to mark the inner volume of the ventricle in the MR images. It means that the ventricle volume segmentation has to be performed.

In many hospitals cardiac MRI data segmentation is proceeded manually, no matter how time demanding the process is. It is reasoned by the fact that the efficiency of automated segmentation algorithms is not still sufficient and necessary manual corrections afterwards take even more time than a fully manual segmentation. Due to technical development in magnetic resonance imaging, number of images obtained during single examination of the heart is rising (for example due to better temporal resolution). We are aware that automated algorithms for the image segmentation will be more required. Many teams all over the world work on problems in digital image processing and also we are trying to make the automated segmentation process more efficient.

In the work, we try to modify and adapt the segmentation model described in [4] to be applicable in processing of special type of real data.

The model is based on numerical solution of a partial differential equation

[1] Myocardium = heart muscle.

(PDE) of the Allen–Cahn type (see [1]). Although the applications of partial differential equations in image processing are relatively new, we could say that they were used in image processing from its very beginning. As an example we can give the standard convolution of the image with the Gaussian kernel (Gaussian smoothing) for increasing the signal-to-noise ratio (see [24]). This procedure can be represented by the solution of a linear diffusion partial differential equation with a zero Dirichlet boundary condition:

$$\begin{aligned} \partial_t u(t,x) - \Delta u(t,x) &= 0 \quad \text{in} \quad (0,T)\times\mathbb{R}^2 \\ u|_{t=0} &= u_{ini} \quad \text{on} \quad \partial\Omega, \end{aligned}$$

where function u_{ini} stands for the input image and the solution $u(t,x)$ for a smoothed one.

Usage of partial differential equations in the image processing has several advantages. Mathematical background of PDEs is available for justification of such algorithms. Application of nonlinear partial differential equations allowed to formulate more sophisticated models (for example image smoothing dependent on the presence of edges of objects in the image). For applications of nonlinear partial differential equations in image processing see for example books as [2, 22].

In the following introductory sections we give basic information about magnetic resonance imaging (MRI) and describe basis of anatomy and function of the heart. Then we continue with description of the segmentation algorithm and finally we present practical results of its application.

1.2 Magnetic resonance imaging

Magnetic resonance imaging (MRI) is a modern non-invasive imaging technique used in medicine to produce high quality images of the inside of the human body. MRI is based on the phenomenon of the nuclear magnetic resonance (NMR) of nuclei with the non-zero magnetic spin (see [18]). In medical practice, usually nuclei of hydrogen ^{1}H are used. MRI is therefore an excellent diagnostic method for the examination of tissues containing high amount of water, such as brain, joints (with tendons, joint sheath, menisci, etc.) or spine (with respect to spinal cord, intervertebral discs etc.), (see Figures 1.1(a)-(c)). Since all these organs can be examined in a steady state, the acquisition time for the image data is not a limiting factor. On the contrary, for the examination of moving tissues, short acquisition time is necessary. Development of fast imaging MR measurement sequences[2] allowed the examination of such unsteady organs as a

[2]MR (measurement) sequence is a sequence of radiofrequency pulses and magnetic field gradient switching in a special manner so that the acquired MR signal represents an image of the examined tissue.

beating heart (see Figure 1.1(d) and [9] for a detailed description of the heart imaging).

Heart imaging makes possible to visualize the myocardial tissue in a steady state with respect to the wall morphology and tissue characteristics (e.g. inflammation or presence of fat). Using dynamic sequences (CINE), heart movement with a good temporal resolution can be studied. The strain of the myocardium during the contraction may be viewed using tagging by preparatory radiofrequency pulse (see Figure 1.2 and [9], pages 24-25). Finally, paramagnetic contrast agent administration is helpful in diagnosis of defects in perfusion in the myocardium and using the so called late enhancement technique, nonviable tissue[3] or pathological involvements in the myocardium such as amyloid may be seen. For detailed description of the late enhancement technique see [9], pages 187-195, example of this type of image is in Figure 1.11 in Section 1.4.4. Further, we deal principally with the processing of the dynamical data.

Dynamical examination of the heart kinetics stands for a valuable examination of the myocardium. During this examination several hundreds of MR images are measured covering the entire left ventricle volume and recording complete cardiac cycle interval with the temporal resolution of about[4] 40ms (see Figures 1.4 and 1.6). Two types of MR sequences are used for acquisition of dynamic CINE images (see [8]): the FLASH and the trueFISP sequence[5]. Both are triggered by electrocardiogram (or by peripheral pulse) of the examined subject[6]. The FLASH sequence is the older MR sequence and it has been used for longer time in heart imaging. Its major disadvantage is the high dependence on the flow of blood which causes non constant MR signal inside ventricles during the cardiac cycle. Also, the signal in the myocardial wall is not homogeneous. On the contrary, the trueFISP sequence offers better signal-to-noise ratio and excellent homogeneity of the signal inside the ventricle during the whole cardiac cycle (see Figure 1.3). Although the FLASH sequence has some disadvantages, it is still used even in radiological departments equipped with modern MR systems since the FLASH data[7] are technically easier to acquire.

Segmentation of the heart ventricle volume and of the wall of the ventricle is an important part of the cardiac MRI data postprocessing. Hemodynamic parameters, such as the ejection fraction, stroke volume or kinetic parameters

[3]Usually result of myocardial infarction.

[4]The temporal resolution on a current modern MR system can be shortened approximately to 5 ms, the usual spatial resolution is 1.2 x 1.2 x 5mm (voxel size).

[5]The trueFISP sequence is also known as the bSSFP sequence.

[6]Examined subject is either a patient or a volunteer undergoing the cardiac MRI examination.

[7]By the FLASH data or images (the trueFISP data or images respectively) we mean MR images obtained using the FLASH acquisition sequence (the trueFISP sequence respectively).

(a) Examination of the brain. (b) Examination of the spine. (c) Examination of joints.

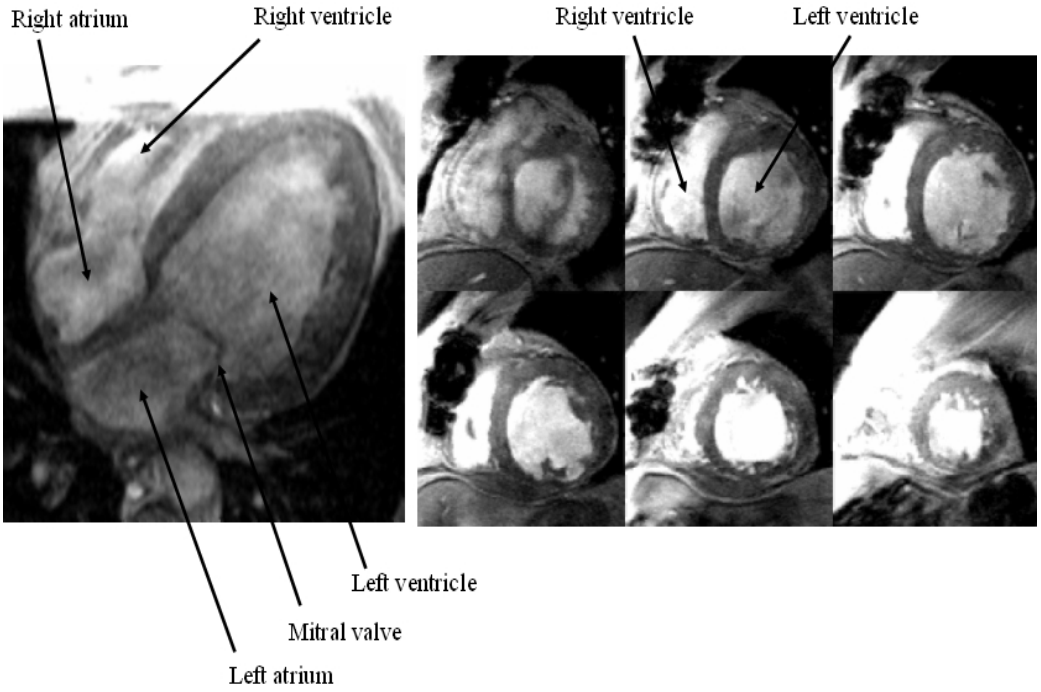

(d) Examination of the heart (cardiac MRI), bright blood technique. On the left, long axes view of the heart (4-chamber view), on the right short axes view.

Figure 1.1: Examples of MR images.

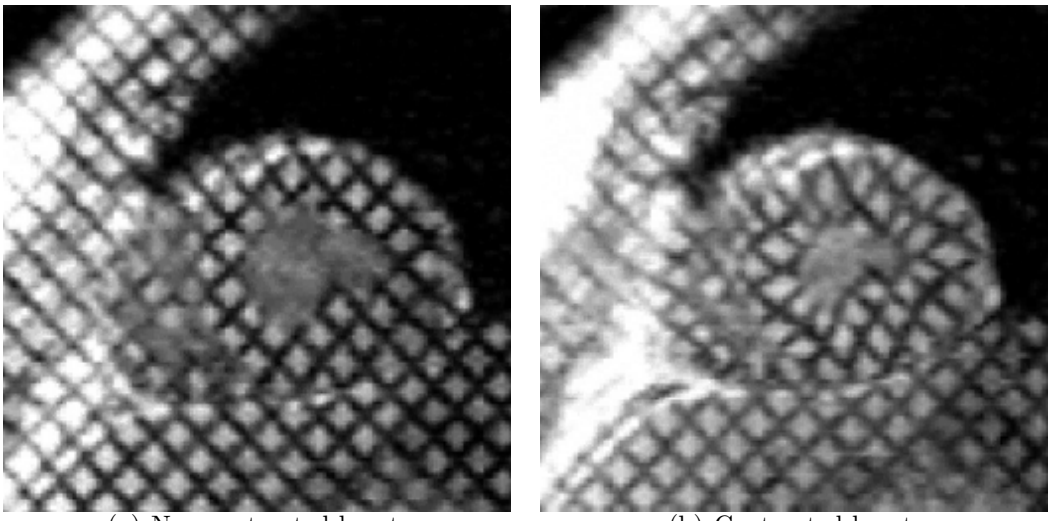

(a) Non-contracted heart. (b) Contracted heart.

Figure 1.2: Tagging of the myocardium using SPAMM technique (spatial modulation of magnetization). The grid deforms with the contracting myocardium. The strain of the contracting tissue may be measured.

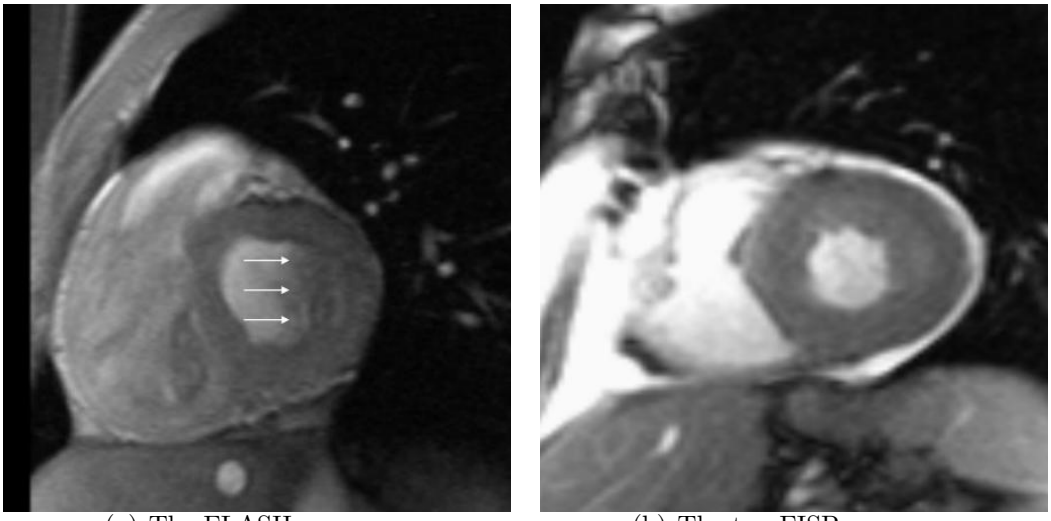

(a) The FLASH sequence. (b) The trueFISP sequence.

Figure 1.3: Short axes view of the contracted heart. The heart is filled by bright blood (*bright blood technique*). Part of the inner contour of ventricles in the image acquired by the FLASH sequence is indistinguishable (arrows). The signal homogeneity inside ventricles in the image obtained by the up-to-date trueFISP sequence makes the inner contour of the ventricle to be clear.

of the wall thickening, can be estimated from the segmented images (see Section 1.3). Compared to the echocardiography (usual technique for the heart examination which is based on the ultrasound emission and detection), MRI provides a better spatial resolution and allows for quantification of the function of myocardium in a reproducible way. Since the number of images from a single cardiac MRI dynamical examination exceeds 200 (number of slices times number of time frames), automation of the segmentation procedure is necessary. The goal of the presented work is the automated segmentation of the cardiac MR images.

1.3 Overview of the heart anatomy and the physiology of the cardiac cycle

In this section we describe basic anatomy of the heart and the cardiac cycle physiology. For detailed information, see for example [15], pages 96-262.

The heart is the central organ of the circulatory system. It is a hollow muscular[8] organ which is situated in the thorax between two lungs (in the space called *mediastinum*). The function of the heart is to pump the blood.

The heart cavity is divided into the left and right part by a longitudinal septum (see Figure 1.5). Each part consists of the atrium and the ventricle. Atrium and the ventricle of either side of the heart are divided by the atrioventricle (AV) valve. On the right side, the valve consists of three cusps (*tricuspidal valve*), on the left side the valve consists of two cusps (*bicuspidal valve*, more often called *mitral valve*). Fibrous structures called *chordae tendineae* prevent folding of the cusps of the AV valves to the atria during the myocardial contraction. The chordae are fixed to the ventricle wall through the *papillary muscles*. One papillary muscle belongs to one cusp of the AV valves. Therefore, in the right heart ventricle there are three papillary muscles whereas in the left heart ventricle there are two of them. We deal with the problem of distinguishing of these structures from the cardiac MR images in Section 3.3.

Atria are filled by the blood from the veins and serve as a weak pump for the ventricles. The ventricles pump the blood into the circulation. The task of the right ventricle is to get the deoxygenated blood from the systemic veins (superior and inferior venae cavae) into the lungs where the oxygenation process takes place. The left ventricle pumps the oxygenated blood into the systemic circulation so that all the tissues of the human body get nutrients and the oxygen and end-products of the metabolism can be taken out.

The period between two successive heart beats is called the *cardiac cycle*.

[8]Heart muscle is histologically similar to a skeletal muscle (see [17], pages 182–204).

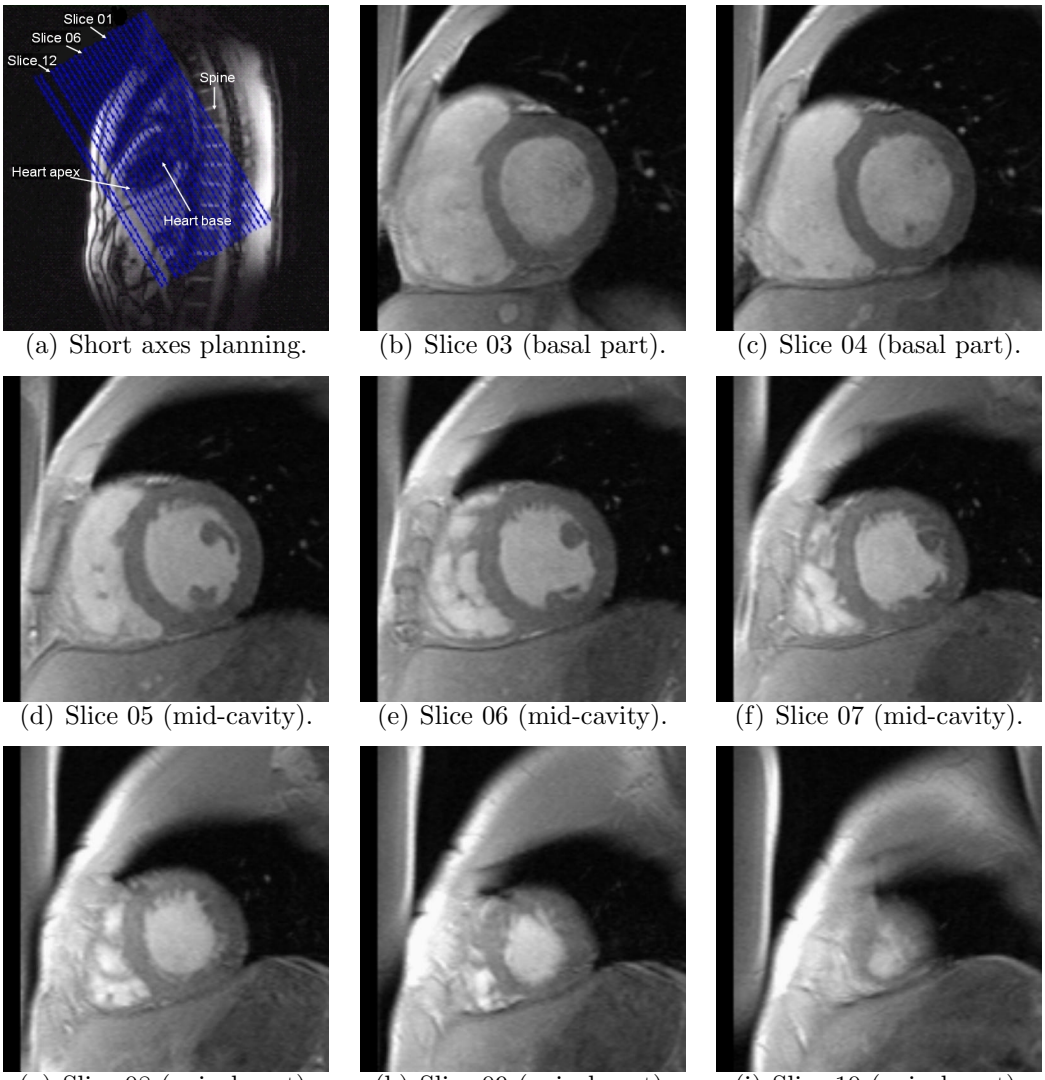

(a) Short axes planning. (b) Slice 03 (basal part). (c) Slice 04 (basal part).

(d) Slice 05 (mid-cavity). (e) Slice 06 (mid-cavity). (f) Slice 07 (mid-cavity).

(g) Slice 08 (apical part). (h) Slice 09 (apical part). (i) Slice 10 (apical part).

Figure 1.4: (a) Sagital view of the body – planning for the data acquisition of the heart in short axes. The whole ventricle volume is covered by approximately 12 slices that we denote Slice 01 – Slice 12 (from the base to apex of the heart). In (b)-(i) selected slices are depicted in the end-diastolic phase (maximal volume of the ventricle).

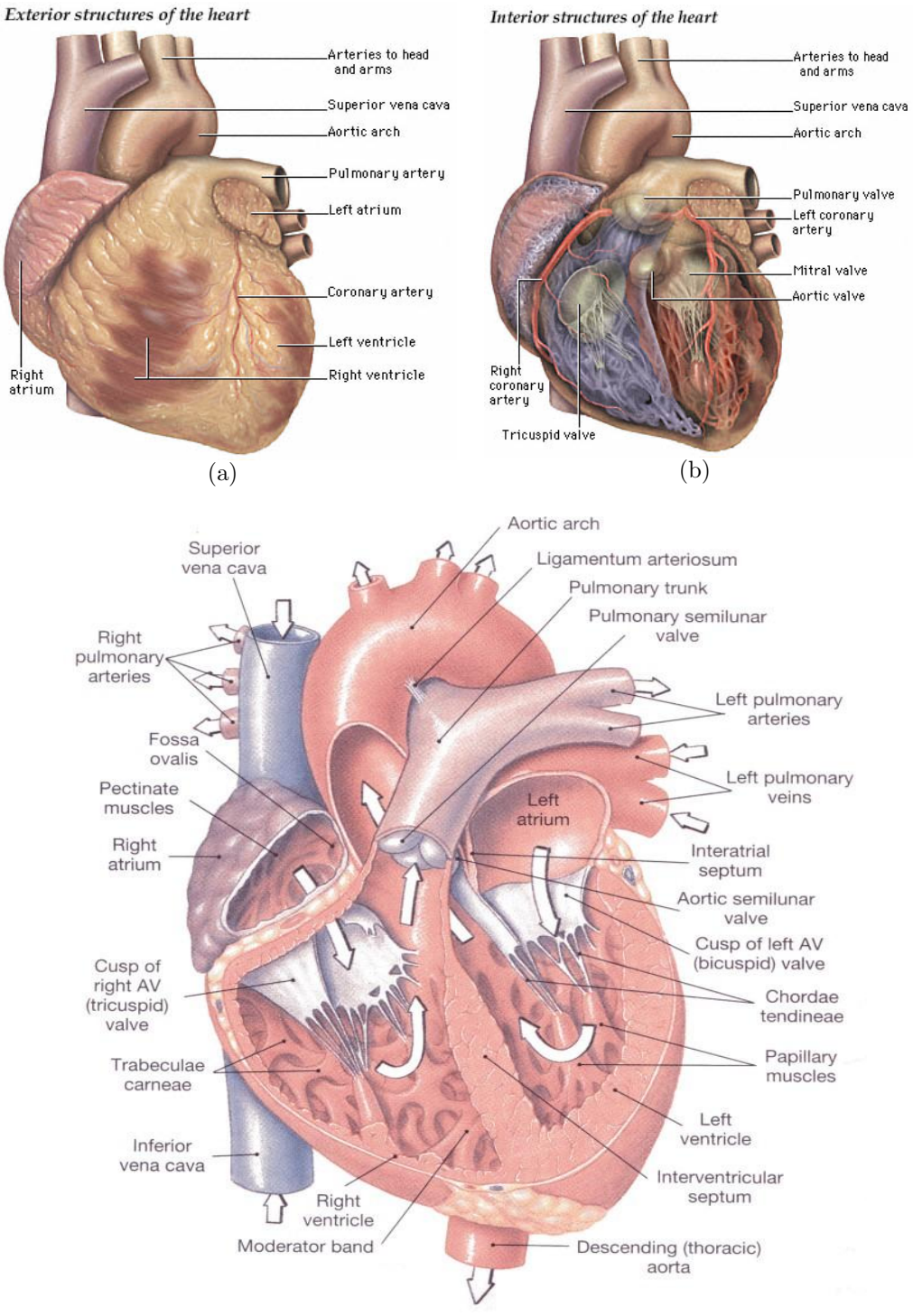

Figure 1.5: Anatomy of the heart. (a-b) adopted from `http://www.ynhh.org/`, (c) from [20].

The cardiac cycle consists of the period of the contraction of ventricles – *systole* when AV valves are closed, and of the relaxation of the ventricles – *diastole*. During the diastole, AV valves are opened and the ventricles are filled by the blood from the atria.

Right heart ventricle pumps the blood against the mean pressure of 15 Torr[9] (the low pressure – pulmonary circulation), while the left heart ventricle pumps the blood against the mean pressure of 100 Torr[10] (the high pressure – systemic circulation). These mechanical features of the circulatory system have an effect in the thickness of the ventricle walls and in the energetic needs of the ventricles. While the thickness of the wall of the right ventricle is approximately 3–4 millimeters, the thickness of the left ventricle is 12–15 millimeters and it has higher energetic needs. This also reasons why the ischemic heart disease (the disease caused by the lack of the oxygen and nutrients inflow and the waste products storing in the tissues) usually concerns the left ventricle and why mechanical parameters of the left heart ventricle are crucial for many people.

We are concerned by the last physiological fact. The heart of an adult person (left and right ventricle separately) has to pump approximately 5 liters of the blood each minute (so called *minute heart volume* – MV). This value can increase even sevenfold in a healthy person undergoing a physical stress (the heartrate can increase threefold and the rest is caused by increased contractility of the myocardium). This *cardiac reserve* is very limited in the nonhealthy myocardium which may lead to a symptomatic cardiac disease under the stressful circumstances. Next, we describe some clinical parameters used for the description of the ventricle function.

1.4 Clinical parameters of the myocardial function

The parameters of the myocardial function may describe clinical situation of the myocardium. It is certain that the primary source of the information about the clinical status comes from the interview between physician and patient and from the physical examination of patient (for example general aspection or the heart auscultation using stethoscope). Examination methods such as electrocardiography (ECG) belong to a standard examination protocol not only for the cardiac patients. Viewing of heart using imaging techniques such as the ultrasound echocardiography (ECHO) or magnetic resonance imaging (cardiac

[9]Clinical physicians usually represent a pressure as 15 Torr = 15mm of the mercury column, that matches approximately 2kPa.

[10]100 Torr matches approximately 15kPa.

MRI) are much more specialized modalities. If properly indicated, they are very valuable since they show the morphological images of the organ.

The evaluation of these images needs years of practice since sometimes even small morphological discrepancies may represent serious pathology. Primarily the detailed description of the current result of the examination for every patient with the consideration to his clinical status has to be done. Many patients are later re-examined so that the evolution of the clinics may be observed. For this purpose, some reproducible parameters that can reflect the healing or the evolution of the disease are needed.

In our work we evaluate the morphological parameters of the ventricle – the ejection fraction and the kinetic parameters of the wall thickening during the cardiac cycle. This is a standard approach in many radiological departments for the imaging of the cardiovascular system. Unfortunately, necessity of the human assistance during the estimation of these parameters (for example for manual marking of the contours of the organ in the images), makes the process to be very time demanding.

1.4.1 Ejection fraction

The *ejection fraction* – EF is the global parameter of the contractive ability of the heart ventricle. The ejection fraction is defined by the following formula:

$$EF = \frac{EDV - ESV}{EDV}, \tag{1.1}$$

where EDV stands for the *end-diastolic volume* (the volume of the fully filled ventricle by the blood) and ESV stands for the *end-systolic volume* (the volume of the blood that remains in the ventricle after its evacuation to the arteries).

A normal value of the ejection fraction ranges between 55% and 80%. Pathologically decreased value means insufficient reserve for the increase in the minute volume (MV). This may be symptomatic only during the physical stress but in more progressive stages it can appear even during the rest. The basic pathophysiological principle is blood stagnation in front of the ventricle during the heart failure. In case of the insufficiency of the right heart ventricle, swellings appear on the extremities. The liver and the lien are filled by the extra blood. In case of the left heart ventricle insufficiency, the clinical status may be even more serious. The pressure in the pulmonary circulation increases and acute pulmonary hypertension develops. The fluid from the capillaries can be effused to the lung alveoli and the patient can undergo a progressive dyspnoea during life threatening pulmonary oedema. It is not rare that due to high load on the right heart ventricle (in course of the pulmonary hypertension) subsequent right heart ventricle failure can appear.

From the above written facts we can see that the ejection fraction is an important value, especially for the cardiac patients. Therefore it is necessary to be able to estimate this value. For the estimation of EF we have to estimate the above described volumes (EDV and ESV). This is routinely done using ultrasound examination (echocardiography). Although this method has limiting accuracy and reproducibility, it is sufficient for the clinical estimation of the approximate values of EF.

Another possibility how to estimate EDV and ESV is the volume calculation from the cardiac magnetic resonance dynamic CINE images (see Figure 1.6). The estimation of the ventricle volumes from the cardiac MRI images stands for a reference method. Thanks to a good temporal resolution it is possible to describe a dynamics of the left heart ventricle volume not only by using the values of EDV and ESV, but also by estimation of the variable ventricle volume during the cardiac cycle.

1.4.2 Ventricle volume estimates

The ventricle volume is usually estimated using short axes images. The heart is covered with a series of approximately 10–12 parallel slices (see Figure 1.4). Each slice evolves during a cardiac cycle. We usually obtain this evolution with the temporal resolution of 10ms to 40ms. This means that whole cardiac cycle is divided e.g. into 20 *time frames*[11] (see Figure 1.6). The heart function is finally represented by approximately 200 two dimensional images (10 slices times 20 time frames). For the estimation of the heart volume we have to mark the inner contour of the ventricle in each image – we have to segment the heart ventricle volume (see Figure 1.7(a)). It means that we have to mark picture elements that are localized inside of the ventricle and those outside of the ventricle. Summing these areas over all the spatial images and multiplying by the slice thickness we obtain the volume of the ventricle that is changing during the cardiac cycle (see Figure 1.8).

The segmentation of the ventricle can be proceeded manually. This is a very time demanding process since number of input images is high. That is the reason why we try to apply the automated segmentation procedure.

1.4.3 Parameters of wall thickening

In addition to heart volume segmentation, we can perform segmentation of the ventricle wall. For this we have to segment both – the inner and the outer contour of the ventricle wall (see Figure 1.7(b)). The ventricle wall thickens

[11] We denote the time images as Time frame 01 – Time frame 20.

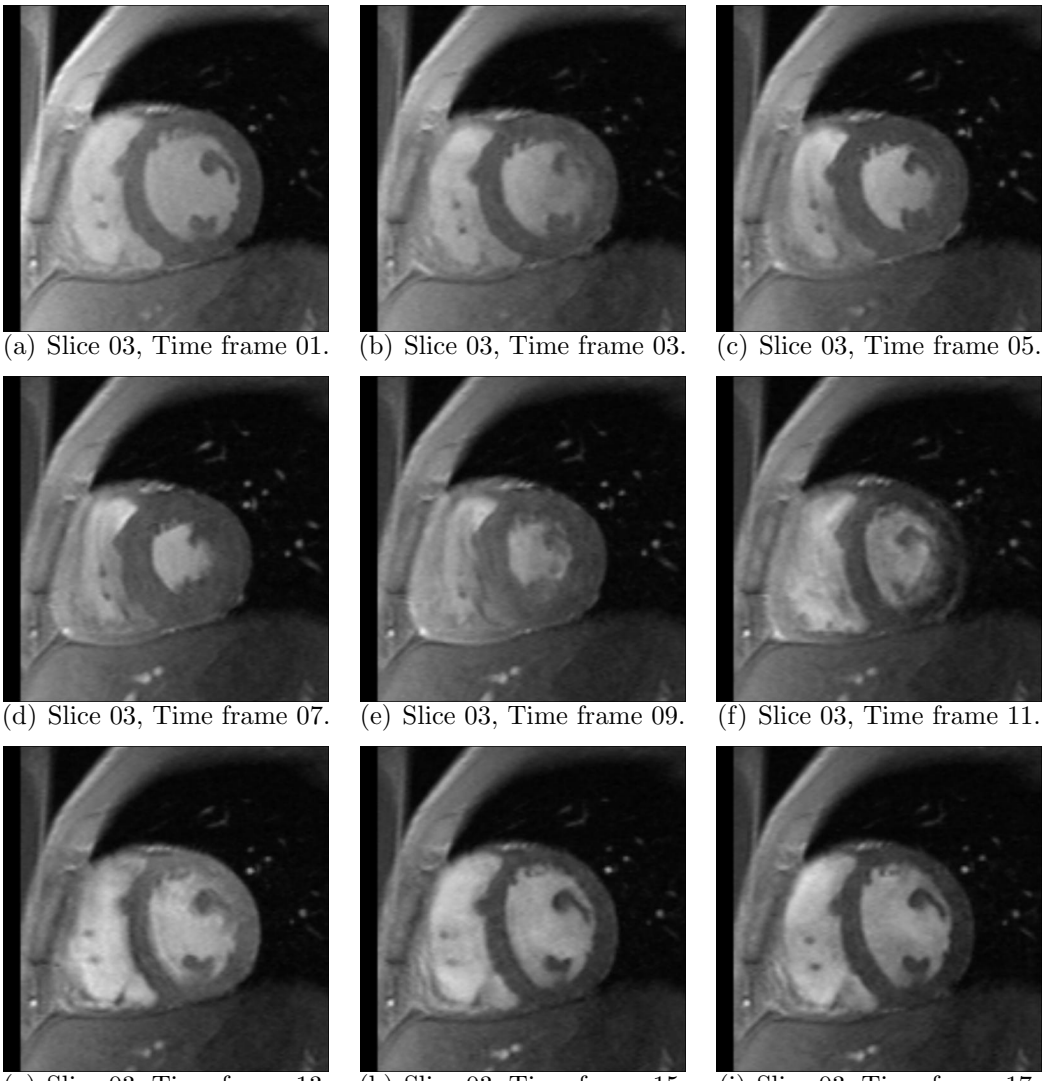

(a) Slice 03, Time frame 01. (b) Slice 03, Time frame 03. (c) Slice 03, Time frame 05.

(d) Slice 03, Time frame 07. (e) Slice 03, Time frame 09. (f) Slice 03, Time frame 11.

(g) Slice 03, Time frame 13. (h) Slice 03, Time frame 15. (i) Slice 03, Time frame 17.

Figure 1.6: Example of cardiac MR images – dynamic CINE series of the heart in short axes. Slice 03 during cardiac cycle. The cycle is divided into 20 time frames. Time frame 01 corresponds to end-diastole (maximal ventricle volume), Time frame 09 in this case to the end-systole (minimal ventricle volume).

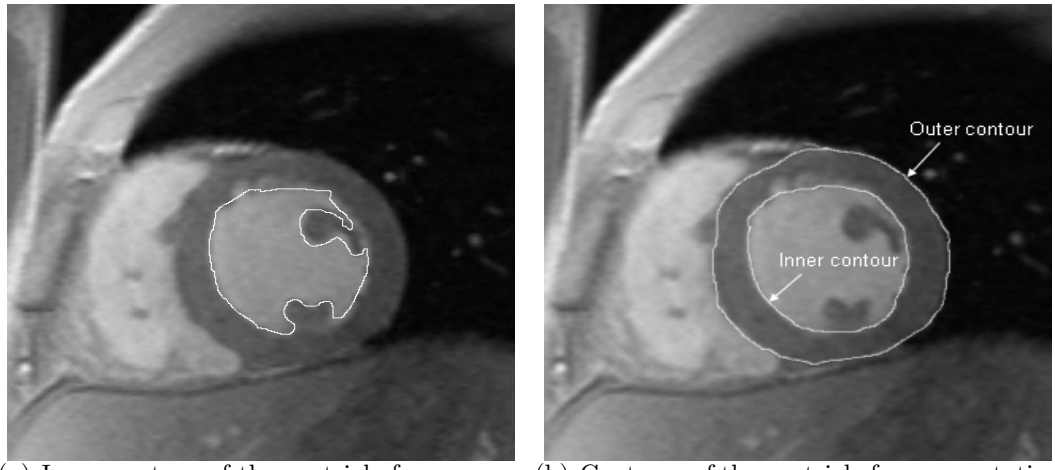

(a) Inner contour of the ventricle for segmentation of the volume (papillary muscles excluded).

(b) Contours of the ventricle for segmentation of the wall.

Figure 1.7: Contours of left ventricle detected for the ventricle volume and wall segmentation.

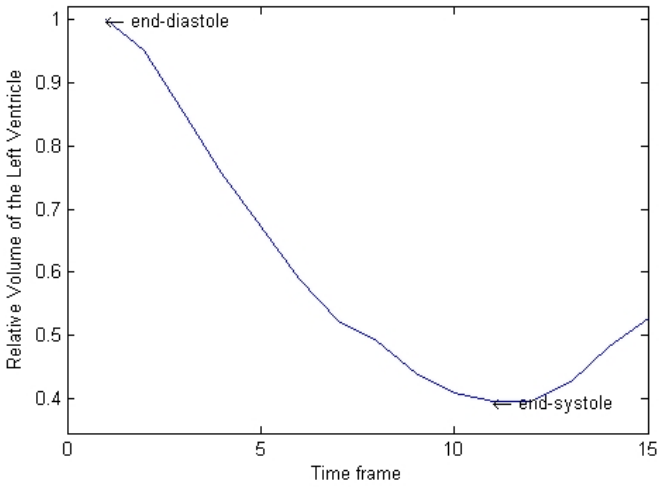

Figure 1.8: Example of estimation of relative volumes of the left heart ventricle during the cardiac cycle. The ejection fraction (EF) is about 60%, that is a normal value.

during the period of heart contraction. From the relative value of the ventricle thickening we can estimate local parameters of the heart ventricle function.

For good reproducibility, the ventricle is divided into 17 segments according to the convention of *The American Heart Association Writing Group on Myocardial Segmentation and Registration for Cardiac Imaging (AHA model)* (see Figure 1.9 and [10]). In each segment the average relative thickening of the ventricle wall in radial direction is estimated to determine the kinetics of the segment. Clinical interpretation is according to Table 1.1. An example of wall thickening estimation is depicted in Figure 1.10.

Table 1.1: Relative thickening of the ventricle wall during myocardial contraction and its clinical interpretation

Relative thickening	Clinical interpretation
$> 30\%$	normokinesis
$> 20\%$ and $< 30\%$	mild hypokinesis
$> 10\%$ and $< 20\%$	severe hypokinesis
$< 10\%$	akinesis
movement in the opposite direction	dyskinesis

1.4.4 Other parameters of the myocardial function

At the end of the introductory chapter we give a few references to another heart functional parameters.

First, we mention the reproducible evaluation of the extent of the fibrous scar after myocardial infarction. This nonviable tissue may be viewed using MRI after administration of the contrast agent (so called late enhancement technique, see Figure 1.11 and Section 1.2). It is the morphological parameter that reflects the development of the infarcted tissue and can be helpful for example in describing the effect of the reperfusion therapy. For details on this work you can see [12]. Also in this case, the segmentation of the fibrous scar is necessary.

Although the parameters described above reflect the function of the myocardium, they are more or less morphological parameters and cannot be used for description of the exact heart mechanics. For describing such phenomena as remodeling of the myocardium after myocardial infarction, we need to have real mechanical parameters. To obtain for example the stress distribution over the myocardium, we have to use constitutive laws. For such a biomechanical approach, see [28].

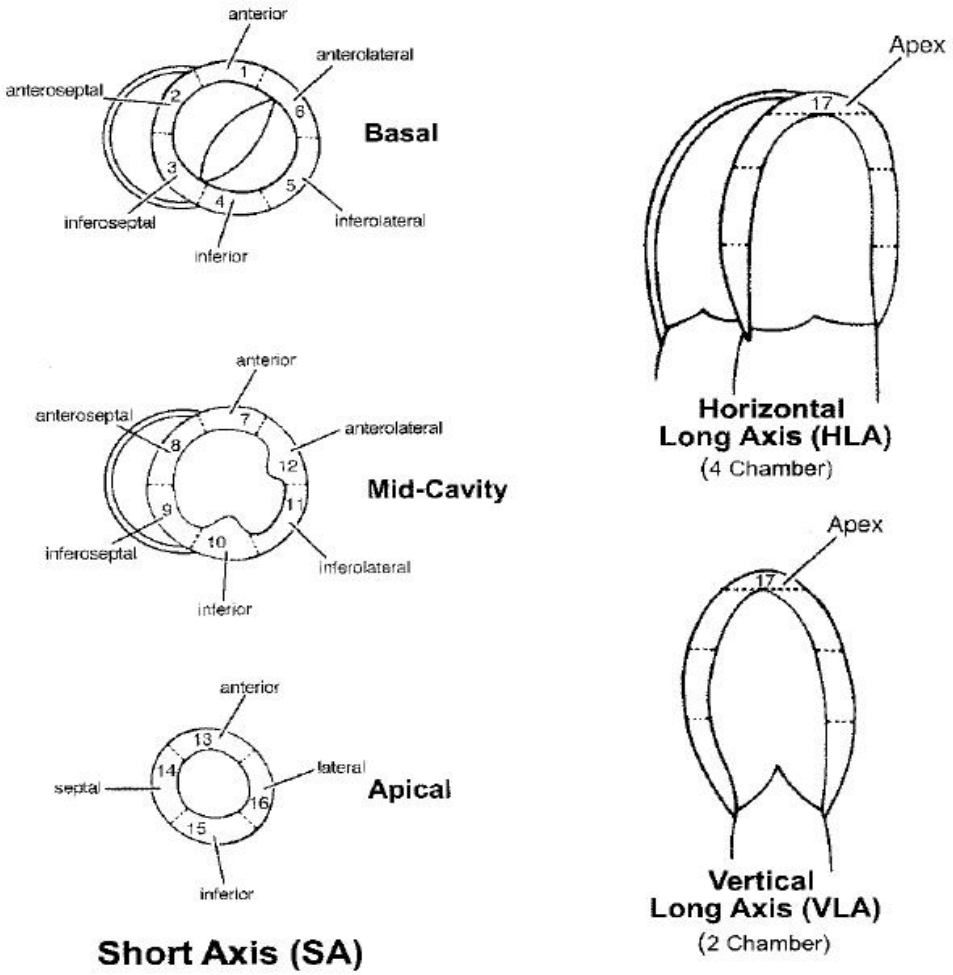

(a) Segments of the left ventricle.

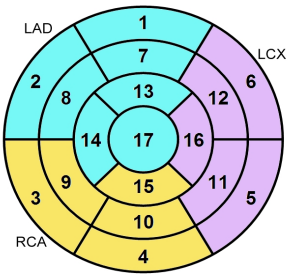

(b) 'Bull eye'.

Figure 1.9: (a) Division of the myocardium of the left heart ventricle into 17 segments according to American Heart Association (AHA). (b) A schematic polar map of the segments (so called 'bull eye'). Blue and purple colors correspond to drainage area of left coronary artery (LAD – left anterior descending branch, LCx – left circumflex branch), yellow color corresponds to the drainage area of right coronary artery (RCA). Adopted from [10].

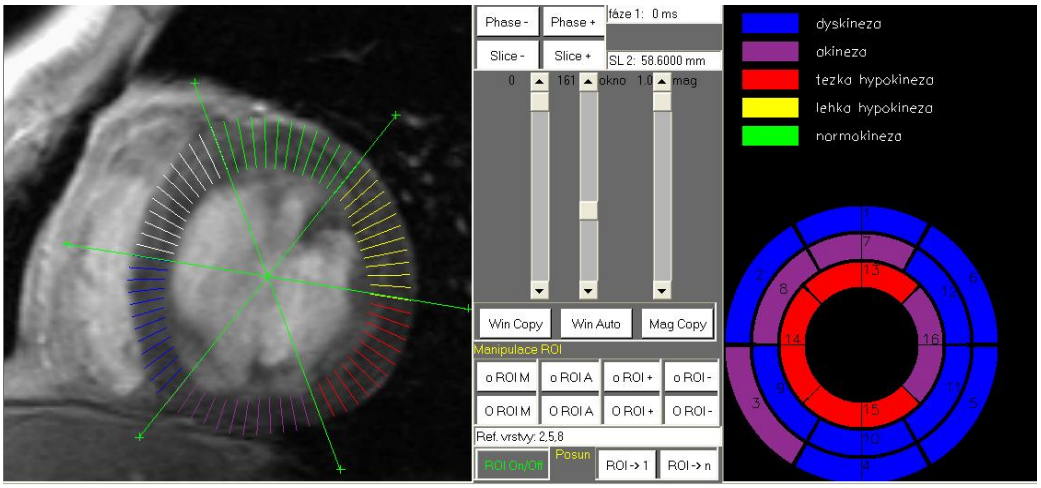

Figure 1.10: Example of the relative thickening of the wall in a radial direction. Result of the examination of the patient with severe myocardial dysfunction (the ejection fraction $< 15\%$). On the left a measurement of the wall thickening from the segmented wall of the left heart ventricle. On the right a 17-segment polar map of the left heart ventricle myocardium ('bull eye')). Color scale from blue – dyskinetic myocardium, purple – akinetic myocardium, red – severely hypokinetic myocardium to green color – normokinetic myocardium.

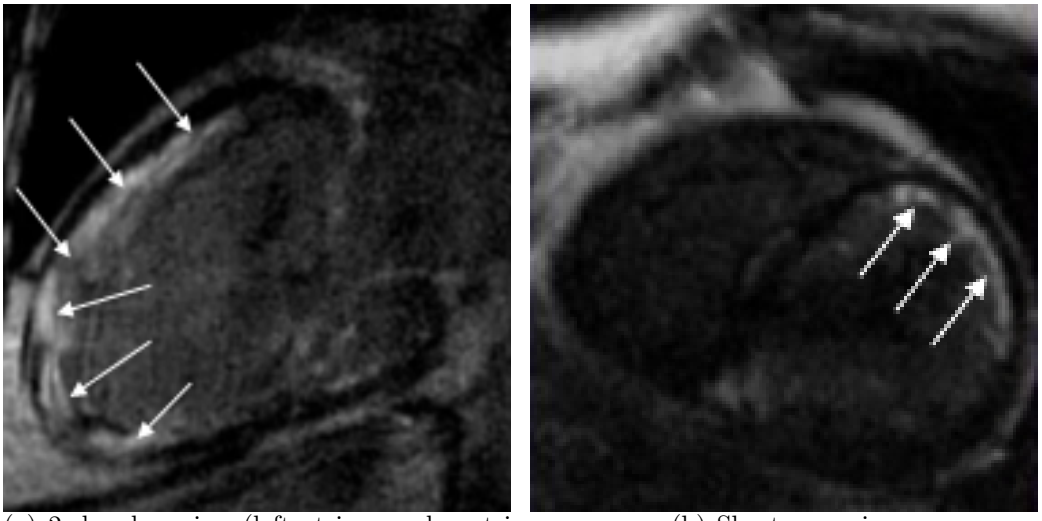

(a) 2-chamber view (left atrium and ventricle).

(b) Short axes view.

Figure 1.11: Late enhancement effect – approximately 10 minutes after the paramagnetic contrast agent administration, the contrast agent is captured into the nonviable tissue (white dye marked with arrows). The images demonstrate status after huge myocardial infarction with the extension over the major part of the anterior wall of left ventricle.

Chapter 2

Image segmentation

2.1 Problem formulation

The goal of the presented work is semiautomated segmentation of the left heart ventricle from the images acquired by magnetic resonance imaging (MRI). In the introductory chapter we have described what kind of information we can obtain from the segmented data and we emphasized the necessity of the automatization of the process.

Our input data are dynamic MR images of the heart in short axis. Number of parallel slices covering the whole ventricle volume varies from 9 to 12, number of time frames into which the cardiac cycle is divided exceeds 20 (both depend on the anatomy, heart rate of the examined subject and on the type of the image acquisition). Our task is to segment heart ventricle volume and the wall of the ventricle in an automated way.

In the image segmentation we will use the model of nonlinear diffusion. The segmented area is characterized by a spatially and time dependent segmentation function $p(t, x)$ with values in the closed interval $[0, 1]$. The segmented area evolves in a time. The border of the segmented area is given by the level-set $\frac{1}{2}$ of the function $p(t, x)$.

The initial segmented area is given by a characteristic function p_{ini} of this area, or its approximation. The function p_{ini} is an initial condition for the development of the segmentation function

$$p(0, x) = p_{ini}(x).$$

The initial guess p_{ini} can be localized either inside the desired segmented area or outside. In the former case, the initial area is expanded by a diffusion process, in the latter case it shrinks to the image boundaries. The function $P_0(x)$ stands for a signal intensity of the MR images (input data).

Basic requirement for the evolution of the segmented area is that evolution has to slow down near the image boundaries. After suitable evolution time T, the segmented area should cover exactly area of the interest (details for the choice of the stopping time T are in Section 2.7.3).

Next, we introduce the mean curvature flow segmentation methods and we briefly describe one model used for the image segmentation. Compared to the model used in the presented work, we denote a segmentation function in the next section by $u(t, x)$. Then, we will deal with our segmentation model, with the mathematical analysis of the model and design a numerical scheme for the solution.

2.2 Segmentation by mean curvature flow

Detection of objects boundaries in an image, that are given by the magnitude of the spatial gradient is a known approach to the image segmentation. The level set method is applicable in this problem (see [21, 2, 22]). In this section we briefly describe another model used in image segmentation.

A segmentation function $u(t, x)$ evolves from the initial condition given by $u(0, x) = u_{ini}(x)$ under a law described by the equation:

$$\frac{\partial u}{\partial t} = |\nabla u| \, \nabla \cdot \left(g(|\nabla u_0|) \frac{\nabla u}{|\nabla u|} \right), \tag{2.1}$$

where $u_0(x)$ stands for the input image (intensity of MR signal in the input image), $g : \mathbb{R}_0^+ \to \mathbb{R}^+$ is a non-increasing edge detector function (the Perona–Malik function) for which $g(0) > 0$, $g(s) \to 0$ for $s \to +\infty$. The evolution of level sets of the function u according to equation (2.1) can be used to the detection of object boundaries.

We can re-write (2.1) into an advection–diffusion form:

$$\frac{\partial u}{\partial t} = \underbrace{g(|\nabla u_0|) \, |\nabla u| \, \nabla \cdot \left(\frac{\nabla u}{|\nabla u|} \right)}_{(A)} + \underbrace{\nabla g(\nabla |u_0|) \cdot \nabla u}_{(B)}. \tag{2.2}$$

The vector field $-\nabla g(|\nabla u_0|)$ in the advective term (B) in equation (2.2) has an important geometrical meaning. It points towards regions in the image where the magnitude of the spatial gradient of the intensity signal u_0 is large and makes level sets of the segmentation function u concentrate in these areas.

To segment such noisy images like cardiac MR images, the advection itself would not be sufficient. It would lead to detection of spurious edges. The term (A) in equation (2.2) avoids such a false detection. It describes motion by mean curvature. It adds a curvature dependence to the level set flow and regularizes

the evolution in the normal direction. Sharp irregularities are smoothed and the curve length in regions with missing edge information is minimized. The process can be also interpreted as an intrinsic diffusion of the curves dependent on $|\nabla u_0|$.

A semi-implicit method of discretization of equation (2.2) using co-volume scheme is described in [21].

2.3 Edge detection using Allen–Cahn equation

In the presented work we use the algorithm based on the phase–field approach to the mean curvature flow (see [4]). We change the notation of the segmentation function back to $p(t,x)$. The function $p(t,x)$ evolves according to the modified Allen–Cahn equation:

$$\begin{aligned} \xi\frac{\partial p}{\partial t} &= \xi\nabla\cdot\Big(g\left(|\nabla G_\sigma * P_0|\right)\nabla p\Big) + g\left(|\nabla G_\sigma * P_0|\right)\Big(\frac{1}{\xi}f_0(p) + \xi F|\nabla p|\Big) \quad \text{in } (0,T)\times\Omega, \\ p\,|_{\partial\Omega} &= 0 \qquad \text{on } (0,T)\times\partial\Omega, \\ p|_{t=0} &= p_{ini} \quad \text{in } \overline{\Omega}, \end{aligned} \tag{2.3}$$

where $|\cdot|$ means the Euclidian norm in $\mathbb{R}^2$, $\Omega = (0,L_1)\times(0,L_2) \subset \mathbb{R}^2, L_1, L_2 > 0$ is a rectangular area that represents the input image, $x = [x_1, x_2] \in \Omega$ is a spatial variable, $t \in (0,T)$ time, $0 < \xi \ll 1$ is a small parameter (connection to level-set segmentation methods for $\xi \to 0_+$ – see [3] and Section 2.6).

The function $p(t,x) \in [0,1]$ is related to the characteristic function of a segmented area. The boundary of the segmented area is at the the level set $\{x \in \Omega : p(t,x) = \frac{1}{2}\}$. An initial guess of the segmented area $p(0,x) = p_{ini}(x)$ can be given by:

$$p(0,x) = p_{ini}(x) = \begin{cases} 1 & \text{for } x \in \text{initial guess of segmented area,} \\ 0 & \text{for } x \in \text{elsewhere,} \end{cases}$$

(see Figure 2.1, automated choice of p_{ini} is discussed in Section 2.7.2). The segmentation function $p(t,x)$ evolves under a diffusion process described by equation (2.3). The diffusion process slows down near edges of the objects in the image. Finally after a certain time T the segmented area p covers the area of our interest (see Figure 2.2).

Intensity of the MR signal in the segmented image enters our model by means of the function $P_0(x)$. Values of the input data signal P_0 are normalized to the interval $[0,1]$. Other terms in equation (2.3) are as follows:

- G_σ is Gauss smoothing kernel, $G_\sigma = \frac{1}{(4\pi\sigma)}e^{-\frac{|x|^2}{4\sigma}}$. The convolution with the piecewise constant function P_0 (input digital image) converts P_0 to

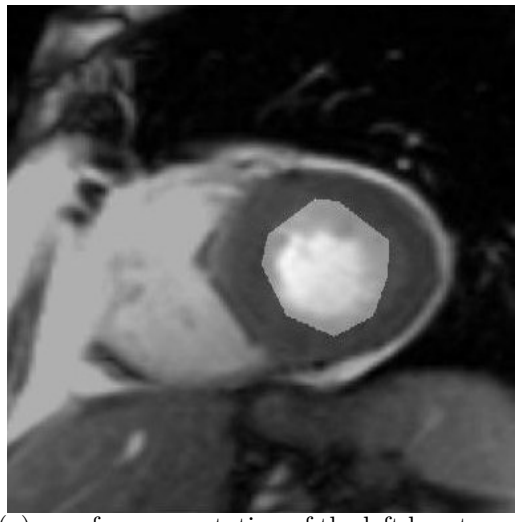

(a) p_{ini} for segmentation of the left heart ventricle volume.

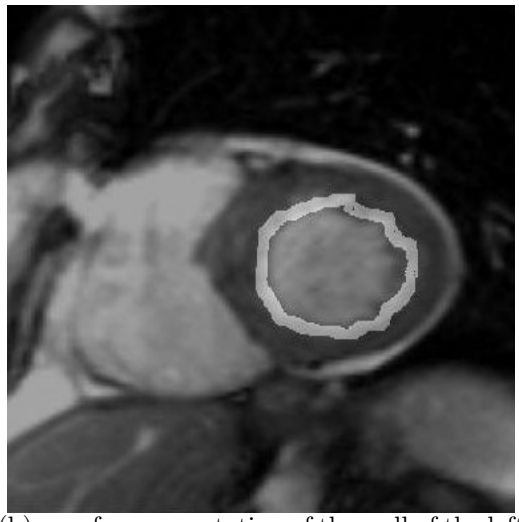

(b) p_{ini} for segmentation of the wall of the left heart ventricle.

Figure 2.1: Examples of the initial guess p_{ini} for the segmentation of the left heart ventricle volume and for the ventricle wall segmentation.

an infinitely smooth function and also removes some spurious structures (increase of the signal-to-noise ratio).

- $g : \mathbb{R}_0^+ \to \mathbb{R}^+$ is a non-increasing Perona–Malik function for which $g(0) > 0$, $g(\sqrt{s})$ is smooth, $g(s) \to 0$ for $s \to +\infty$. The term $g\left(|\nabla G_\sigma * P_0|\right)$ makes the diffusion process to slow down near edges in the image. Our choice of this function: $g(s) = \frac{1}{1+\lambda s^2}$, parameter $\lambda > 0$. We use a suitable value of the parameter λ according to Section 2.7.1.

- F has meaning of an external force that influences motion of the curves. The sign of F causes either expanding of the segmented area (for $F > 0$) or its shrinking (for $F < 0$). We deal with the choice of the external force F in Section 2.7.2.

- f_0 is a polynomial related to the motion of phase–fields by mean curvature (see [7]). It is derived from the double-well potential w_0 as $w_0' = f_0$. With the choice $f_0 = p(1-p)(p-\frac{1}{2})$, we obtain the potential w_0 with two stable minima in 0 and 1 and one unstable maximum in $\frac{1}{2}$.

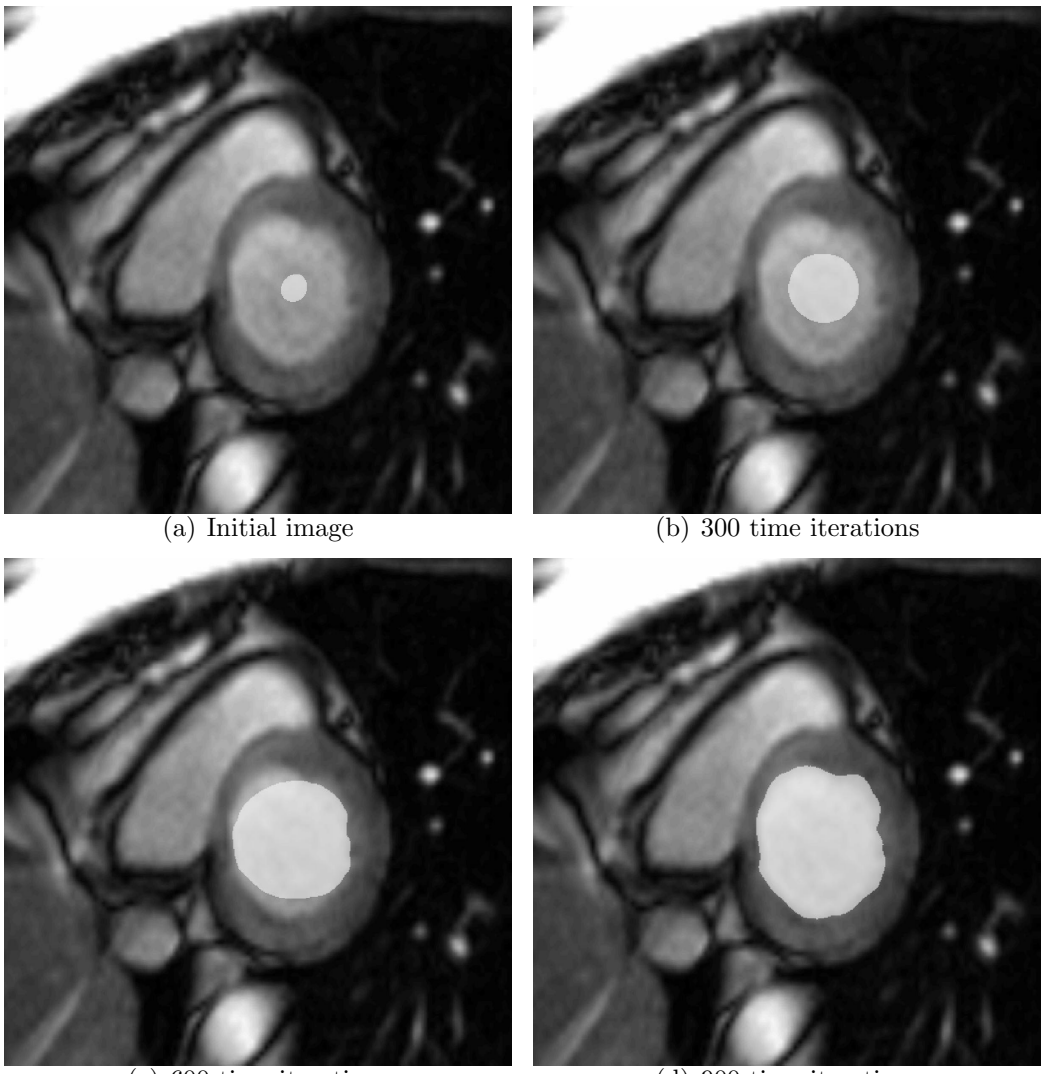

(a) Initial image (b) 300 time iterations

(c) 600 time iterations (d) 900 time iterations

Figure 2.2: Evolution of the initial area p_{ini} according to equation (2.3). Parameters of equation (2.3): $\xi = 0.09$, $\lambda = 30$, $F = 2$, time step $\tau = 0.005$. The process can be viewed as a nonlinear diffusion dependent on a magnitude of the spatial gradient of the input image ($|\nabla g(P_0(x))|$).

2.4 Mathematical analysis

The initial–boundary–value problem (2.3) is investigated by means of the weak formulation. We use the notation: $(u,v) = \int_\Omega u(x)v(x)\mathrm{d}x$, $p^m = p^m(t,x)$, $\partial_t p^m = \frac{\partial p^m}{\partial t}(t,x)$, $g = g(|\nabla P_0|)$, $\|\cdot\|$ if not specified means the L^2 norm in the sense of $\|\cdot\|^2 = \int_\Omega |\cdot|^2 \mathrm{d}x$. Following lemmas will be used:

Lemma 1 (Compact imbedding.)[1] *Be $\mathcal{B}_0 \subset \mathcal{B} \subset \mathcal{B}_1$ Banach spaces where $\mathcal{B}_0$ and $\mathcal{B}_1$ are reflexive, $p_0, p_1 \in (1,+\infty)$ and $\mathcal{B}_0 \hookrightarrow\hookrightarrow \mathcal{B}_0$. Define a set*

$$\mathcal{Y} = \{v | v \in L^{p_0}(0,T;\mathcal{B}_0) \wedge \dot{v} \in L^{p_1}(0,T;\mathcal{B}_1)\},$$

which is endowed by the norm

$$\|v\|_{\mathcal{Y}} = \|v\|_{L^{p_0}(0,T;\mathcal{B}_0)} + \|\dot{v}\|_{L^{p_1}(0,T;\mathcal{B}_1)},$$

for $v \in \mathcal{Y}$. Then

$$\mathcal{Y} \hookrightarrow\hookrightarrow L^{p_0}(0,T;\mathcal{B}).$$

Lemma 2 (Nemytskiĭ mappings in Lebesgue spaces).[2] *If $a : \Omega \times \mathbb{R}^{m_1} \times \cdots \times \mathbb{R}^{m_j} \to \mathbb{R}^{m_0}$ is a Carathéodory mapping and the functions $u_i : \Omega \to \mathbb{R}^{m_i}, i = 1,\ldots,j$ are measurable. We define Nemytskiĭ mapping $\mathcal{N}_a(u_1,\ldots,u_j) : \Omega \to \mathbb{R}^{m_0}$*

$$[\mathcal{N}_a(u_1,\ldots,u_j)](x) = a\left(x, u_1(x), u_j(x)\right). \tag{2.4}$$

Then $\mathcal{N}_a(u_1,\ldots,u_j)$ is measurable. Moreover, if a satisfies the growth condition

$$|a(x,r_1,\ldots,r_j)| \le \gamma(x) + C\sum_{i=1}^{j} |r_i|^{p_i/p_0} \text{ for some } \gamma \in L^{p_0}(\Omega), \tag{2.5}$$

with $1 \le p_i \le +\infty$, $1 \le p_0 < +\infty$, then $\mathcal{N}_a$ is a bounded continuous mapping $L^{p_1}(\Omega;\mathbb{R}^{m_1}) \times \cdots \times L^{p_j}(\Omega;\mathbb{R}^{m_j}) \to L^{p_0}(\Omega;\mathbb{R}^{m_0})$. If some $p_i = +\infty, i = 1,\ldots,j$, the same holds if the respective term $|\cdot|^{p_i/p_0}$ is replaced by any continuous function.

We follow [3] to formulate and prove the main theorem:

Theorem 1 *Let $p_{ini} \in H_0^1(\Omega)$, then there exists a unique solution of the weak formulation of the initial–boundary–value problem (2.3)*

$$\begin{aligned} \xi\frac{\mathrm{d}}{\mathrm{d}t}(p,q) + \xi\Big(g(|\nabla P_0|)\nabla p, \nabla q\Big) &= \frac{1}{\xi}\Big(g(|\nabla P_0|)f_0(p), q\Big) + \xi\Big(g(|\nabla P_0|)F|\nabla p|, q\Big), \\ p(0,x) &= p_{ini}(x), \end{aligned} \tag{2.6}$$

[1] See [19].
[2] See [26], pages 19–20.

a.e. $t \in (0,T)$, $\forall x \in \Omega, \forall q \in \mathcal{D}(\Omega)$, *which satisfies:*

$$\begin{aligned} p &\in L^2\left(0,T;H^2\left(\Omega\right)\cap H_0^1\left(\Omega\right)\right), \\ \frac{\partial p}{\partial t} &\in L^2\left(0,T;L^2\left(\Omega\right)\right). \end{aligned}$$

Proof We derive a sequence of approximate solutions to the problem (2.6) by means of the Faedo-Galerkin method. Assume that there is an orthonormal basis $\{v_i\}_{i\in\mathbb{N}}$ of $L^2(\Omega)$ consisting of eigenvectors of the operator $-\Delta$ coupled with homogeneous Dirichlet boundary conditions.
Let $V_m = \mathrm{span}\{v_i\}_{i\in\mathbb{N}_m}$ be a finite-dimensional subspace ($\mathbb{N}_m = \{1,\dots,m\}$) and $\mathcal{P}_m : L^2 \to V_m$ be the L^2-projection operator (coinciding with the H^1 projection). We seek for a solution p^m from $[0,T)$ to V_m of an auxiliary problem

$$\begin{aligned} \xi\frac{\mathrm{d}}{\mathrm{d}t}(p^m,v_j) + \xi\Big(g(|\nabla P_0|)\nabla p^m,\nabla v_j\Big) &= \frac{1}{\xi}\Big(g(|\nabla P_0|)f_0(p^m),v_j\Big) \\ &\quad + \xi\Big(g(|\nabla P_0|)F|\nabla p^m|,v_j\Big), \\ &\quad \text{a.e.in}(0,T),\forall j=1,\dots,m, \\ p^m(0,x) &= \mathcal{P}_m p_{ini}(x). \end{aligned} \tag{2.7}$$

Using the basis functions of the finite dimensional space V_m, we express the solution of (2.7) as

$$p^m(t) = \sum_{i\in\mathbb{N}_m} \gamma_i^m(t) v_i$$

and substitute it to (2.7). We obtain a system of ordinary differential equations with the unknowns functions $\gamma_i(t)$. The theory of ordinary differential equations gives us the unique solution $\gamma_i(t)$ on $(0,T)$ for $T>0$. We will derive the a priori estimates for the solution of the finite-dimension problem p^m of (2.7) and pass to a weak limit p.

We multiply (2.7) by $\mathrm{d}\gamma_m/\mathrm{d}t$ and sum for $j \in \mathbb{N}_m$

$$\xi\left\|\partial_t p^m\right\|^2 = \xi\Big(\nabla\cdot(g\nabla p^m),\partial_t p^m\Big) + \frac{1}{\xi}\Big(g f_0(p^m),\partial_t p^m\Big) + \xi\Big(gF|\nabla p^m|,\partial_t p^m\Big). \tag{2.8}$$

We apply Gauss–Green–Ostrogradskiy theorem on the first term of the right side (2.8) (with the assumption of zero Dirichlet boundary condition)

$$\xi\Big(\nabla\cdot(g\nabla p^m),\partial_t p^m\Big) = -\xi\Big(g\nabla p^m,\partial_t(\nabla p^m)\Big) = -\xi\frac{1}{2}\frac{\mathrm{d}}{\mathrm{d}t}\Big(g\nabla p^m,\nabla p^m\Big). \tag{2.9}$$

We choose w_0 in a form: $w_0' = -f_0$, f_0 is a polynomial of the third grade and w_0 is a polynomial of the fourth grade for which $(gw_0(p), 1) \geq 0$. The second term of the right side (2.8) is

$$\frac{1}{\xi}\Big(gf_0(p^m), \partial_t p^m\Big) = -\frac{1}{\xi}\Big(g\partial_t w_0(p^m), 1\Big) = -\frac{1}{\xi}\frac{\mathrm{d}}{\mathrm{d}t}\Big(gw_0(p^m), 1\Big). \tag{2.10}$$

We substitute (2.9) and (2.10) to the equation (2.8) and we obtain

$$\xi\Big\|\partial_t p^m\Big\|^2 + \frac{\xi}{2}\frac{\mathrm{d}}{\mathrm{d}t}\Big(g\nabla p^m, \nabla p^m\Big) + \frac{1}{\xi}\frac{\mathrm{d}}{\mathrm{d}t}\Big(gw_0(p^m), 1\Big) = \underbrace{\xi\Big(gF|\nabla p^m|, \partial_t p^m\Big)}_{(*)}. \tag{2.11}$$

We suppose that g and F are bounded in a sense: There exist constants $g_0, g_1, C_F > 0$ such that

$$\begin{aligned} 0 < g_0 \leq g(|\nabla P_0|) &\leq g_1, \\ |F| &\leq C_F. \end{aligned} \tag{2.12}$$

Then we estimate $(*)$ using Cauchy–Schwarz inequality and Young inequality for $\varepsilon = \frac{1}{2}$

$$\begin{aligned} (*) &\leq \xi g_1 C_F \|\nabla p^m\| \cdot \|\partial_t p^m\| \leq \frac{\xi}{4}\|\partial_t p^m\|^2 + \xi g_1^2 C_F^2 \underbrace{\|\nabla p^m\|^2}_{\leq \frac{1}{g_0}(g\nabla p^m, \nabla p^m)} \\ &\leq \frac{\xi}{4}\|\partial_t p^m\|^2 + \xi\frac{g_1^2 C_F^2}{g_0}(g\nabla p^m, \nabla p^m). \end{aligned} \tag{2.13}$$

After the substitution of the estimate (2.13) to the equation (2.11), applying $(gw_0(p), 1) \geq 0$, we obtain

$$\begin{aligned} &\frac{3}{4}\xi\Big\|\partial_t p^m\Big\|^2 + \frac{\mathrm{d}}{\mathrm{d}t}\underbrace{\Big\{\frac{\xi}{2}\Big(g\nabla p^m, \nabla p^m\Big) + \frac{1}{\xi}\Big(gw_0(p^m), 1\Big)\Big\}}_{\mathbf{U}(t)} \\ &\leq \xi\frac{g_1^2 C_F^2}{g_0}\Big(g\nabla p^m, \nabla p^m\Big) \\ &\leq \underbrace{\frac{2g_1^2 C_F^2}{g_0}}_{\mathrm{D}}\underbrace{\Big\{\frac{\xi}{2}\Big(g\nabla p^m, \nabla p^m\Big) + \frac{1}{\xi}\Big(gw_0(p^m), 1\Big)\Big\}}_{\mathbf{U}(t)}. \end{aligned} \tag{2.14}$$

In (2.14) we see

$$\frac{\mathrm{d}}{\mathrm{d}t}\mathbf{U}(t) \leq \mathrm{D}\mathbf{U}(t). \tag{2.15}$$

Applying Gronwall lemma on (2.15), we obtain

$$\mathbf{U}(t) \leq U(0)e^{\mathrm{D}t}. \tag{2.16}$$

We substitute D and $\mathbf{U}(t)$ to (2.16) by means of terms from (2.14)

$$\begin{aligned}&\Big\{\frac{\xi}{2}\Big(g\nabla p^m, \nabla p^m\Big) + \frac{1}{\xi}\Big(gw_0(p^m), 1\Big)\Big\}(t)\\ &\quad\leq \Big\{\frac{\xi}{2}\Big(g\nabla p^m, \nabla p^m\Big) + \frac{1}{\xi}\Big(gw_0(p^m), 1\Big)\Big\}(0)\cdot e^{\frac{2g_1^2C_F^2}{g_0}t}.\end{aligned} \tag{2.17}$$

We integrate (2.14) over $(0,T)$ with the same notation for $\mathbf{U}(t)$ as in (2.14). Applying (2.16) we get

$$\begin{aligned}&\frac{3}{4}\xi\int_0^T \Big\|\partial_t p^m\Big\|^2 \mathrm{d}t + \mathbf{U}(T)\\ &\quad\leq \mathbf{U}(0) + \mathrm{D}\int_0^T \mathbf{U}(t)\mathrm{d}t\\ &\quad\leq \mathbf{U}(0) + \mathrm{D}\mathbf{U}(0)\frac{1}{\mathrm{D}}\Big(e^{\mathrm{D}T} - 1\Big)\\ &\quad= e^{\mathrm{D}T}\mathbf{U}(0).\end{aligned} \tag{2.18}$$

From (2.18) we finally obtain an estimate

$$\begin{aligned}&\frac{3}{4}\xi\int_0^T \Big\|\partial_t p^m\Big\|^2 + \Big\{\frac{\xi}{2}\Big(g\nabla p^m, \nabla p^m\Big) + \frac{1}{\xi}\Big(gw_0(p^m), 1\Big)\Big\}(T)\\ &\quad\leq e^{\mathrm{D}T}\Big\{\frac{\xi}{2}\Big(g\nabla p^m, \nabla p^m\Big) + \frac{1}{\xi}\Big(gw_0(p^m), 1\Big)\Big\}(0).\end{aligned} \tag{2.19}$$

If $\Big\{\frac{\xi}{2}\Big(g\nabla p, \nabla p\Big) + \frac{1}{\xi}\Big(gw_0(p), 1\Big)\Big\}(0)$ is bounded (that means $\nabla p_{ini} \in L^2(\Omega)$, $p_{ini} \in L^4(\Omega)$), then from (2.19) we have an a priori estimate

$$\int_0^T \Big\|\partial_t p^m\Big\|^2 \leq C_1, \tag{2.20}$$

where C_1 is a constant not dependent on m.
In a similar way, by integration of the equation (2.14) over $(0,t)$ we have

$$\frac{3}{4}\xi\int_0^t \Big\|\partial_t p^m\Big\|^2 + \Big\{\frac{\xi}{2}\Big(g\nabla p^m, \nabla p^m\Big) + \frac{1}{\xi}\Big(gw_0(p^m), 1\Big)\Big\}(t) \leq C_2, \tag{2.21}$$

where C_2 is a constant not dependent on m.
From (2.21) we have for *a.a.* $t \in [0,T]$

$$\|\nabla_x p^m(t,x)\|^2 \leq C_3, \tag{2.22}$$

$$\int_\Omega w_0(p^m) \leq C_4, \tag{2.23}$$

again C_2 and C_3 are constants not dependent on m.
Using derived a priori estimates we have:

- $\partial_t p^m$ is bounded in $L^2(0,T;L^2)$ independently on m according to (2.20).
- ∇p^m is bounded in $L^\infty(0,T;L^2(\Omega))$ independently on m according to (2.22).
- p^m is bounded in $L^\infty(0,T;L^4(\Omega))$ independently on m according to (2.23).

Due to the Lemma 1 (compact imbedding) with assumptions $p_0 = 4, p_1 = 2, \mathcal{B}_0 = L^4(\Omega), \mathcal{B} = L^4(\Omega), \mathcal{B}_1 = L^2(\Omega)$

$$\begin{aligned} \{\partial_t p^m\}_{m=1}^\infty &\text{ is bounded in } L^2(0,T;L^2(\Omega)), \\ \{p^m\}_{m=1}^\infty &\text{ is bounded in } L^4(0,T;H_0^1 \cap L^4(\Omega)), \end{aligned}$$

we can pass to the strong limit p in $L^4(0,T;L^4(\Omega)$.
For testing by arbitrary function $v \in D(\Omega)$ we can approximate v by the sequence $v^m \in V_m$, so that $v^m \to v$ strongly in $\mathcal{D}(\Omega)$. Following lemmas will be used to pass to the limit in (2.6).

Lemma 3 *Let $p^m \rightharpoonup p$ in $L^2(0,T;L^2(\Omega))$. If q_1 denotes weak limit of $\frac{d}{dt}p^m$ in $L^2(0,T;L^2(\Omega))$, then $\frac{d}{dt}p = q_1$.*

Proof Let $v \in \mathcal{D}(\Omega)$ and $\psi(t) \in \mathcal{C}^1[0,T], \psi(0) = \psi(T) = \dot{\psi}(0) = \dot{\psi}(T) = 0$. We multiply $(\partial_t p^m, v)$ by $\psi(t)$ and integrate over $(0,T)$. Using integration by parts, Lebesgue dominated theorem (p^m is majorized according to estimate (2.23)) and definition of the weak limit we obtain:

$$\begin{aligned} \int_0^T (\partial_t p^m, v)\,\psi(t)\mathrm{d}t &= \int_0^T \frac{\mathrm{d}}{\mathrm{d}t}(p^m, v)\,\psi(t)\mathrm{d}t \\ &= -\int_0^T (p^m, v)\,\dot{\psi}(t)\mathrm{d}t \to -\int_0^T (p, v)\,\dot{\psi}(t)\mathrm{d}t \\ &= \int_0^T \frac{\mathrm{d}}{\mathrm{d}t}(p, v)\,\psi(t)\mathrm{d}t. \end{aligned} \tag{2.24}$$

□

Lemma 4 *If p denotes strong limit of p^m in $L^4(0,T;L^4(\Omega))$, then $f_0(p^m) \rightharpoonup f_0(p)$ weakly in $L^{4/3}(0,T;L^{4/3}(\Omega))$.*

Proof We have the strong convergence of p^m in $L^4(0,T;L^4(\Omega))$ according to Lemma 1 (compact imbedding). Furthermore we know that p^m is bounded in $L^\infty(0,T;L^4(\Omega))$ according to (2.23). That is why

$$\begin{aligned} ||f_0(p^m)||_{L^{4/3}(\Omega)} &= \left\| -\frac{1}{2}p^m + \frac{3}{2}(p^m)^2 - (p^m)^3 \right\|_{L^{4/3}(\Omega)} \\ &\leq \frac{1}{2}\left\|p^m\right\|_{L^{4/3}(\Omega)} + \frac{3}{2}\|(p^m)^2\|_{L^{4/3}(\Omega)} + \|(p^m)^3\|_{L^{4/3}(\Omega)} \\ &\leq \frac{1}{2}\left\|p^m\right\|_{L^{4/3}(\Omega)} + \frac{3}{2}\left\|p^m\right\|^2_{L^{8/3}(\Omega)} + \left\|p^m\right\|^3_{L^4(\Omega)} \end{aligned} \tag{2.25}$$

and $f_0(p^m)$ is bounded in $L^\infty(0,T;L^{4/3}(\Omega))$ independently on m. Due to reflexivity of this space, we can choose a weakly convergent subsequence, which we denote again by the index m:

$$f_0(p^m) \rightharpoonup q_2 \quad \text{in } L^{4/3}(0,T;L^{4/3}(\Omega)). \tag{2.26}$$

It remains to show that $f_0(p) = q_2$. We will use Lemma 2 (the continuity of the Nemytskiĭ mapping). Let $\mathcal{N}_{f_0}(\bar{x},r) = a(\bar{x},r)$ be a Nemytskiĭ mapping induced by f_0, for $\bar{x} = (t,x)$ and $r = p(\bar{x})$. Since

$$\begin{aligned} |a(\bar{x},r)| = |f_0(r)| &= \left| -\frac{1}{2}r + \frac{3}{2}r^2 - r^3 \right| \\ &\leq \frac{1}{2}|r| + \frac{3}{2}|r|^2 + |r|^3 \leq \underbrace{C|r|^{4/3}}_{C|r|^3}. \end{aligned} \tag{2.27}$$

Using the growth condition (2.27), the Nemytskiĭ mapping $\mathcal{N}_{f_0}$ is a bounded continuous mapping from $L^4(0,T;L^4(\Omega))$ (strong topology) to $L^{4/3}(0,T;L^{4/3}(\Omega))$ (weak topology), according to Lemma 2. It reasons that $f_0(p) = q_2$. □

Lemma 5 *The sequence ∇p^m converges strongly to ∇p in $L^2(0,T;L^2(\Omega;\mathbb{R}^n))$ and $|\nabla p^m|$ converges weakly to $|\nabla p|$ in $L^2(0,T;L^2(\Omega;\mathbb{R}^n))$.*

Proof We test the equation (2.6) by $p^m - p$ and integrate over $(0,T)$

$$\begin{aligned} &\xi \int_0^T \left(\frac{\partial p^m}{\partial t}, p^m - p \right) \mathrm{d}t + \xi \int_0^T \left(g\nabla p^m, \nabla\left(p^m - p\right)\right) \mathrm{d}t \\ &\quad = \frac{1}{\xi}\int_0^T \left(g f_0\left(p^m\right), p^m - p\right) \mathrm{d}t + \xi \int_0^T \left(gF|\nabla p^m|, p^m - p\right) \mathrm{d}t. \end{aligned} \tag{2.28}$$

We add and subtract a term

$$\xi \int_0^T (g\nabla p, \nabla(p^m - p))\mathrm{d}t, \tag{2.29}$$

to the equality (2.28). Since $\nabla(p^m - p) \rightharpoonup 0$ weakly in $L^2(0,T;L^2(\Omega;\mathbb{R}^n))$, we know that (2.29) tends to 0. We repeat that $p^m - p \to 0$ in $L^4(0,T;L^4(\Omega))$. Then we have

$$\begin{aligned}
&\xi \int_0^T (g\nabla(p^m - p), \nabla(p^m - p))\mathrm{d}t \\
&\quad = -\xi \int_0^T (\frac{\partial p^m}{\partial t}, p^m - p) + \frac{1}{\xi}\int_0^T (g f_0(p^m), p^m - p)\mathrm{d}t \\
&\qquad + \xi \int_0^T (gF|\nabla p^m|, p^m - p)\mathrm{d}t + \xi \int_0^T (g\nabla p, \nabla(p^m - p))\mathrm{d}t. \quad (2.30)
\end{aligned}$$

Since all the terms on the right-side of (2.30) tend to 0 and

$$\begin{aligned}
&\xi g_0 \int_0^T \|\nabla(p^m - p)\|^2 \mathrm{d}t = \xi g_0 \int_0^T (\nabla(p^m - p), \nabla(p^m - p))\mathrm{d}t \\
&\quad \leq \xi \int_0^T (g\nabla(p^m - p), \nabla(p^m - p))\mathrm{d}t \to 0,
\end{aligned}$$

we have

$$\int_0^T \|\nabla(p^m - p)\|^2 \mathrm{d}t \to 0, \text{ for } m \to \infty,$$

and we proved the strong convergence of ∇p^m in $L^2(0,T;L^2(\Omega;\mathbb{R}^n))$. Finally, Lemma 2 (continuity of the Nemytskiĭ operator induced by $|\cdot|$) gives us weak convergence of $|\nabla p^m|$ to $|\nabla p|$ in $L^2(0,T;(\Omega;\mathbb{R}^n))$. □

Due to reflexivity of the spaces, after a multi-step selection from the sequence $\{p^m\}_{m=1}^{\infty}$, we can choose a subsequence $\{p^{m'}\}_{m'=1}^{\infty}$ with the following properties:

- $p^{m'} \rightharpoonup$ weakly in $L^4(0,T;H_0^1(\Omega) \cap L^4(\Omega))$,
- $p^{m'} \to$ strongly in $L^4(0,T;L^4(\Omega))$ due to Lemma 1 (compact imbedding),
- $\partial_t p^{m'} \rightharpoonup$ weakly in $L^2(0,T;L^2(\Omega))$ according to Lemma 3,
- $f_0(p^{m'}) \rightharpoonup$ weakly in $L^{4/3}(0,T;L^{4/3}(\Omega))$ according to Lemma 4,

- $|\nabla p^{m'}| \rightharpoonup$ weakly in $L^2(0,T;L^2(\Omega;\mathbb{R}^n))$ according to Lemma 5,

We denote the subsequence again by index m. Using these convergence results we are able to pass to the limit in (2.7) under the following scheme:

$$\begin{array}{ccccccc}
\underbrace{\xi\frac{\mathrm{d}}{\mathrm{d}t}\left(p^m,v\right)} & + & \underbrace{\xi\Big(g(|\nabla P_0|)\nabla p^m,\nabla v\Big)} & = & \underbrace{\frac{1}{\xi}\Big(g(|\nabla P_0|)f_0(p^m),v\Big)} & + & \underbrace{\xi\Big(g(|\nabla P_0|)F|\nabla p^m|,v\Big)} \\
\downarrow & & \downarrow & & \downarrow & & \downarrow \\
\xi\frac{\mathrm{d}}{\mathrm{d}t}\left(p,v\right) & + & \xi\Big(g(|\nabla P_0|)\nabla p,\nabla v\Big) & = & \frac{1}{\xi}\Big(g(|\nabla P_0|)f_0(p),v\Big) & + & \xi\Big(g(|\nabla P_0|)F|\nabla p|,v\Big) \\
\text{due to Lemma 3} & & \text{due to weak convergence of } \nabla p^m & & \text{due to Lemma 4} & & \text{due to Lemma 5}
\end{array}$$

Figure 2.3: Scheme of the convergence of the Faedo–Galerkin approximations p^m.

Regarding the satisfaction of the initial condition of the weak solution, we multiply the equation (2.7) by the function $\psi(t) \in \mathcal{C}^1[0,T]$ for which $\psi(T) = 0$ and converge under the scheme from Figure 2.3. After integration by parts we have $\forall v \in \mathcal{D}(\Omega)$:

$$\begin{aligned}
&\xi(p_{ini},v)\psi(0) - \int_0^T \xi(p,v)\dot{\psi}\mathrm{d}t \\
&\quad - \int_0^T \psi\left[-\xi(gp,v) + \frac{1}{\xi}(gf_0(p),v) + \xi(gF|\nabla p|,v)\right]\mathrm{d}t = 0. \quad (2.31)
\end{aligned}$$

In a similar way, after multiplying (2.6) by a scalar function $\psi(t) \in \mathcal{C}^1[0,T]$, for which $\psi(0) = 0$ and integrating by parts we have $\forall v \in \mathcal{D}(\Omega)$:

$$\begin{aligned}
&\xi(p(0),v)\psi(0) - \int_0^T \xi(p,v)\dot{\psi}\mathrm{d}t \\
&\quad - \int_0^T \psi\left[-\xi(gp,v) + \frac{1}{\xi}(gf_0(p),v) + \xi(gF|\nabla p|,v)\right]\mathrm{d}t = 0. \quad (2.32)
\end{aligned}$$

We subtract the equations (2.31) and (2.32) and obtain $\forall v \in \mathcal{D}(\Omega), \forall \psi \in \mathcal{C}^1[0,T], \psi(T) = 0$:

$$(p_{ini} - p(0), v)\,\psi(0) = 0. \quad (2.33)$$

The last equality means that $p(0) = p_{ini}$ in $L^2(\Omega)$. This is the proof of the existence of the weak solution.

For the uniqueness we consider two solutions by p_1 and p_2 of the problem (2.6). We denote $p_{12} = p_1 - p_2$ and use it as a test function in (2.6) with either $p = p_1$ or $p = p_2$. After the subtraction of the equations we have

$$\begin{aligned}
&\xi \frac{\mathrm{d}}{\mathrm{d}t}\|p_{12}\|^2 + \xi(g\nabla p_{12}, \nabla p_{12}) \\
&\quad = \frac{1}{\xi}(g(f_0(p_1) - f_0(p_2)), p_{12}) + \xi(gF(|\nabla p_1| - |\nabla p_2|), p_{12}) \text{ in } (0,T), \\
&p_{12}(0) = 0.
\end{aligned} \tag{2.34}$$

Lemma 6 *Let $p_1, p_2 \in \mathbb{R}$ and $p_{12} = p_1 - p_2$. Then for a polynomial $f_0(p) = p(1-p)(p-\frac{1}{2})$ the following inequality holds:*

$$(f_0(p_1) - f_0(p_2), p_{12}) \leq \frac{7}{4}(p_{12})^2. \tag{2.35}$$

Proof Since f_0 is a polynomial of the the form

$$f_0(p) = p(1-p)(p-\frac{1}{2}) = -p^3 + \frac{3}{2}p^2 - \frac{1}{2}p,$$

we have

$$\begin{aligned}
f_0(p_1) - f_0(p_2) &= -\frac{1}{2}(p_1 - p_2) + \frac{3}{2}(p_1^2 - p_2^2) - (p_1^3 - p_2^3) \\
&= p_{12}\left(-\frac{1}{2} + \frac{3}{2}(p_1 + p_2) - (p_1^2 + p_1 p_2 + p_2^2)\right) \\
&= p_{12}\left(-\frac{1}{2}(p_1 + p_2)^2 - \frac{1}{2}p_1^2 + \frac{3}{2}p_1 - \frac{1}{2}p_2^2 + \frac{3}{2}p_2 - \frac{1}{2}\right) \\
&= p_{12}\left(-\frac{1}{2}(p_1 + p_2)^2 - \frac{1}{2}\left(p_1 - \frac{3}{2}\right)^2 - \frac{1}{2}\left(p_2 - \frac{3}{2}\right)^2 + \frac{9}{8} + \frac{9}{8} - \frac{1}{2}\right) \\
&\leq \frac{7}{4}p_{12}.
\end{aligned} \tag{2.36}$$

Then

$$(f_0(p_1) - f_0(p_2), p_{12}) \leq \left(\frac{7}{4}p_{12}, p_{12}\right) \leq \frac{7}{4}(p_{12})^2. \tag{2.37}$$

□

Due to Lemma 6, boundeness of g and F according to (2.12) and since the triangular inequality yields

$$\left|\,|\nabla p_1| - |\nabla p_2|\,\right| \leq |\nabla p_{12}|\,, \tag{2.38}$$

we obtain from (2.34)

$$\xi\frac{\mathrm{d}}{\mathrm{d}t}\|p_{12}\|^2+\xi g_0\|\nabla p_{12}\|^2\leq\frac{1}{\xi}g_1\frac{7}{4}\|p_{12}\|^2+\xi F_C g_1(|\nabla p_{12}|,p_{12})\ \text{ in } (0,T),$$
$$p_{12}(0)=0. \tag{2.39}$$

Using Cauchy–Schwarz inequality we have

$$\xi\frac{\mathrm{d}}{\mathrm{d}t}\|p_{12}\|^2+\xi g_0\|\nabla p_{12}\|^2\leq\frac{7g_1}{4\xi}\|p_{12}\|^2+\xi F_C g_1\|\nabla p_{12}\|\|p_{12}\|\ \text{ in } (0,T),$$
$$p_{12}(0)=0, \tag{2.40}$$

Applying Young inequality on the last term, we obtain

$$\xi\frac{\mathrm{d}}{\mathrm{d}t}\|p_{12}\|^2+\frac{\xi g_0}{2}\|\nabla p_{12}\|^2\leq\|p_{12}\|^2\underbrace{\left(\frac{7g_1}{4\xi}+\frac{\xi F_C^2 g_1^2}{2g_0}\right)}_{A}\ \text{ in } (0,T),$$
$$p_{12}(0)=0. \tag{2.41}$$

Since $\xi g_0\geq 0$, and a constant $A\geq 0$ we have

$$\begin{aligned}\xi\frac{\mathrm{d}}{\mathrm{d}t}\|p_{12}\|^2 &\leq A\|p_{12}\|^2\ \text{ in } (0,T),\\ p_{12}(0) &= 0.\end{aligned} \tag{2.42}$$

Applying Gronwall lemma we finally get:

$$\|p_{12}\|^2\leq 0 \text{ for all } t\in(0,T). \tag{2.43}$$

From (2.43) we obtain $p_{12}=p_1-p_2=0$, for all $t\in(0,T)$ that proves the uniqueness of the solution of (2.6).

Finally, the regularity of the solution p is proved in Lemma 8. □

Remark 1 Since $\Omega\subset\mathbb{R}^2$ with Lipschitz boundary, $H^1(\Omega)$ can be continuously imbedded [13]:

$$H^1(\Omega)\hookrightarrow L^p,\quad \forall p\in(1,+\infty). \tag{2.44}$$

Lemma 7 *Let $\Omega\in\mathbb{R}^2$ be a rectangular domain. Then the Laplacian operator maps surjectively.*

$$\Delta: H_0^1(\Omega)\cap H^2(\Omega)\to L^2(\Omega) \tag{2.45}$$

Proof: For the proof, see [14]. It is based on the following equality (for the rectangular domain Ω):

$$\int_\Omega |\Delta u|^2 = \sum_{|\alpha|=2} \int_\Omega |D^\alpha u|^2.$$

Lemma 8 *Under the assumption of Theorem 1, the function p belongs to $L^2(0,T;H^2(\Omega)\cap H_0^1(\Omega))$.*

Proof The weak formulation of the problem (2.3) using a test function $q \in \mathcal{D}(\Omega)$:

$$\xi(\partial_t p, q) + \xi(\nabla\cdot(g\nabla p), q) = \frac{1}{\xi}(g f_0(p), q) + \xi(gF|\nabla p|, q). \tag{2.46}$$

In the sense of $\mathcal{D}'(0,T)$ we can write

$$\xi\partial_t p + \xi\nabla\cdot(g\nabla p) = \frac{1}{\xi} g f_0(p) + \xi F|\nabla p|. \tag{2.47}$$

We recall that under the a priori estimates (2.20), (2.22) and (2.23), we have $\partial_t p \in L^2(0,T;L^2(\Omega))$, $p \in L^\infty(0,T;L^s(\Omega))$ for $s \in (1,+\infty)$ (due to Remark 1), $f_0(p) \in L^2(0,T;L^2(\Omega))$, $\nabla p \in L^\infty(0,T;L^2(\Omega))$.
As $\partial_t p$, $f_0(p)$, $|\nabla p|$ belong to $L^2(\Omega)$, this means that $\nabla\cdot(g\nabla p) \in L^2(\Omega)$.
Since

$$\nabla\cdot(g\nabla p) = g\Delta p + \nabla g\cdot\nabla p, \tag{2.48}$$

and

$$\begin{aligned} \nabla p &\in L^2(0,T;L^2(\Omega)), \\ g &\in \mathcal{C}^\infty(\Omega), \end{aligned}$$

we have

$$g\Delta p + \underbrace{\nabla g\cdot\nabla p}_{\in L^2(L^2)} \in L^2(0,T;L^2(\Omega)).$$

Therefore

$$g\Delta p \in L^2(0,T;L^2(\Omega)). \tag{2.49}$$

Using the boundeness of g (2.12), we obtain the following inequality

$$\int_0^T \int_\Omega |g\Delta p|^2 \geq g_0 \int_0^T \int_\Omega |\Delta p|^2.$$

That is why

$$\Delta p \in L^2(0,T;L^2(\Omega)).$$

Applying Lemma 7 we finally get

$$p \in L^2(0,T;H^2(\Omega)\cap H_0^1(\Omega)).$$

□

2.5 Numerical solution

2.5.1 Numerical analysis

The detailed numerical analysis of the problem is in [5]. The treatment of the discretized equation is similar to the analysis in Section 2.4.

We discretize the problem (2.3) in space and time on a regular rectangular grid

$$\begin{aligned}\overline{\omega_h} &= \{[ih_1, jh_2] : i = 0, \ldots, N_1; \quad j = 0, \ldots, N_2\}, \\ \omega_h &= \{[ih_1, jh_2] : i = 0, \ldots, N_1 - 1; \quad j = 0, \ldots, N_2 - 1\},\end{aligned}$$

where $h = (h_1, h_2)$ stands for size of the mesh, N_1, N_2 for size of the grid. The following notations for discretization of variables are introduced:

$$\begin{aligned} u_{\bar{x}_1,ij} &= \tfrac{u_{i,j}-u_{i-1,j}}{h_1}, & u_{x_1,ij} &= \tfrac{u_{i+1,j}-u_{i,j}}{h_1}, \\ u_{\bar{x}_2,ij} &= \tfrac{u_{i,j}-u_{i,j-1}}{h_2}, & u_{x_2,ij} &= \tfrac{u_{i,j+1}-u_{i,j}}{h_2}, \\ u_{\bar{x}_1x_1,ij} &= \tfrac{1}{h_1^2}(u_{i+1,j} - 2u_{i,j} + u_{i-1,j}), \end{aligned}$$

$$\bar{\nabla}_h u = [u_{\bar{x}_1}, u_{\bar{x}_2}], \nabla_h u = [u_{x_1}, u_{x_2}].$$

The semi-discrete scheme of the equation (2.3) according to the above notations has the form

$$\begin{aligned} \xi\partial_t p^h &= g\xi\nabla_h \cdot g\bar{\nabla}_h p^h + \frac{1}{\xi} g f_0(p^h) + \xi|\bar{\nabla}_h p^h| F \text{ on } \omega_h \\ p^h(0) &= \mathcal{P}_h p_{ini}, \end{aligned} \tag{2.50}$$

where the solution is a map $p^h : \bar{\omega}_h \to \mathbb{R}$. First, the properties and relations of the grid functions are investigated. Then, similarly as in Section 2.4 we derive necessary a priori estimates and we will use them for the proof of convergence of the scheme to the weak solution. In Section 2.5.2 we describe the numerical scheme for the computational solution.

Functions on a grid
Let $\mathcal{H}_h = \{f | f : \omega_h \to \mathbb{R}\}$ be a set of grid functions. Basic definitions and properties will be given:

Definition 1 Let ω_h be an uniform rectangular grid imposed on a domain $\Omega \in \mathbb{R}^2$. Let $h = (h_1, h_2)$ is the mesh size. Then the dual grid is a set

$$\bar{\omega}_h^* = \Big\{\Sigma_{ij} \in \bar{\Omega} | \Sigma_{ij} = \big(x_i^1 - \tfrac{h_1}{2}, x_i^1 + \tfrac{h_1}{2}\big) \times \big(x_j^2 - \tfrac{h_2}{2}, x_j^2 + \tfrac{h_2}{2}\big) \cap \bar{\Omega} \text{ for } [x_i^1, x_j^2] \in \bar{\omega_h}\Big\}.$$

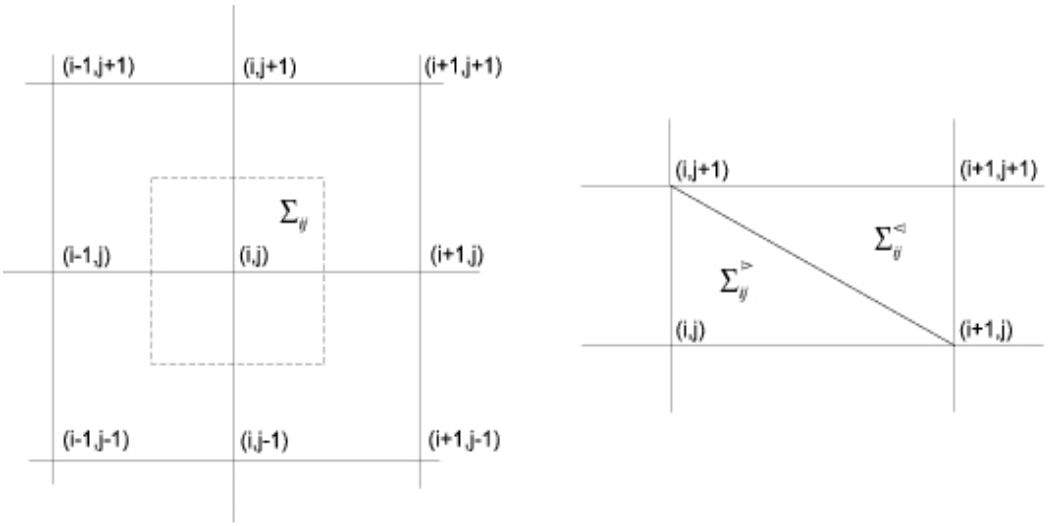

Figure 2.4: Definition of dual grid, adopted from [6].

The dual simplicial grid is a set

$$\bar{\omega}_h^{*s} = \bar{\omega}_h^{*\triangleleft} \cup \bar{\omega}_h^{*\triangleright},$$

with

$$\begin{aligned} \bar{\omega}_h^{*\triangleleft} &= \left\{ \Sigma_{ij}^{\triangleleft} \in \bar{\Omega} | \Sigma_{ij}^{\triangleleft} = [x_{i,j}, x_{i-1,j}, x_{i,j-1}]_\kappa \cap \bar{\Omega} \text{ for } [x_i^1, x_j^2] \in \bar{\omega}_h \right\}, \\ \bar{\omega}_h^{*\triangleright} &= \left\{ \Sigma_{ij}^{\triangleright} \in \bar{\Omega} | \Sigma_{ij}^{\triangleright} = [x_{i-1,j-1}, x_{i-1,j}, x_{i,j-1}]_\kappa \cap \bar{\Omega} \text{ for } [x_i^1, x_j^2] \in \bar{\omega}_h, \right\}, \end{aligned}$$

where $[z_1, z_2, z_3]_\kappa = \left\{ x \in \mathbb{R}^2 | x = \sum_{j=1}^3 \gamma_j z_j, \sum_{j=1}^3 \gamma_j = 1, \gamma_{1,2,3} \geq 0 \right\}$ is the convex hull of the set $\{z_1, z_2, z_3\}$.

Definition 2 Let $\mathcal{H}_h$ is a set of grid functions on $\bar{\omega}_h$. The following mappings are defined:

- $\mathcal{Q}_h : \mathcal{H}_h \to \mathcal{C}(\bar{\Omega})$ such that for each $u \in \mathcal{H}_h$ (extension to Ω by the Lagrange interpolation)

  $$(\mathcal{Q}_h u)(x_1, x_2) = u_{i-1,j-1} + \nabla_h u_{i-1,j-1} \cdot [x^1 - x^1_{i-1,j-1}, x^2 - x^2_{i-1,j-1}],$$

  for $[x_1, x_2] \in \Sigma_{ij}^{\triangleright},\ \Sigma_{ij}^{\triangleright} \in \bar{\omega}_h^{*\triangleright}$
  and

  $$(\mathcal{Q}_h u)(x_1, x_2) = u_{i,j} + \bar{\nabla}_h u_{i,j} \cdot [x^1 - x^1_{i-1,j-1}, x^2 - x^2_{i,j}],$$

  for $[x_1, x_2] \in \Sigma_{ij}^{\triangleright}, \quad \Sigma_{ij}^{\triangleright} \in \bar{\omega}_h^{*\triangleright}$.

- $\mathcal{S}_h : \mathcal{H}_h \to L^1(\Omega)$ such that for each $u \in \mathcal{H}_h$ (extension to Ω by a stepwise constant function)

$$(S_h u)(x^1, x^2) = u_{i,j},$$

for $[x_1, x_2] \in \Sigma_{ij}, \quad \Sigma_{ij} \in \bar{\omega}_h^*$.

- $\mathcal{P}_h : \mathcal{C}(\bar{\Omega}) \to \mathcal{H}_h$ (operator of projection)

$$(P_h u)_{i,j} = u(x_{i,j}),$$

for $x_{i,j} \in \bar{\omega}_h$.

We summarize some basic properties of the above defined mappings (see [6], pages 34–42):

- Let ω_h be a grid on the domain Ω, $u, v \in \mathcal{H}_h$ such that $u, v|_{\partial\Omega} = 0$, then

$$\begin{aligned}
\int_\Omega \mathcal{S}_h u \mathcal{S}_h v \mathrm{d}x &= (u, v)_h, && (2.51)\\
(\nabla(\mathcal{Q}_h u), \nabla(\mathcal{Q}_h v)) &= (\bar{\nabla}_h u, \bar{\nabla}_h v], && (2.52)\\
||\mathcal{Q}_h u||_{L^2(\Omega)} &\leq ||\mathcal{S}_h u||_{L^2(\Omega),} && (2.53)\\
\int_\Omega |\mathcal{Q}_h u - \mathcal{S}_h u|^2 &\leq \frac{h^2}{6} ||\bar{\nabla}_h u]|^2, && (2.54)
\end{aligned}$$

where

$$\begin{aligned}
(u, v)_h &= \sum_{i,j=1}^{N_1-1, N_2-1} h_1 h_2 u_{ij} v_{ij}, \quad ||u||_h^2 = (u, u)_h && (2.55)\\
(\mathbf{f}, \mathbf{g}] &= (f^1, g^1\rfloor + (f^2, g^2\rceil, && (2.56)\\
(f^1, g^1\rfloor &= \sum_{i,j=1}^{N_1, N_2-1} h_1 h_2 f_{ij}^1 g_{ij}^1, && (2.57)\\
(f^2, g^2\rceil &= \sum_{i,j=1}^{N_1-1, N_2} h_1 h_2 f_{ij}^2 g_{ij}^2. && (2.58)
\end{aligned}$$

We define the space

$$l^p(\omega_h) = \{\mathcal{H}_h, ||\cdot||_{ph}\},$$

where

$$||u||_{ph}^p = \sum_{i,j=1}^{N_1-1, N_2-1} h_1 h_2 |f_{ij}|^p,$$

- Let $u \in H_0^1(\Omega) \cap H^2(\Omega)$. Then

$$\mathcal{Q}_h(\mathcal{P}_h)u \to u \tag{2.59}$$

  in $H^1(\Omega)$, if $h \to 0$.

- Let $p \in \mathcal{C}^{0,\nu}(\Omega), \nu \in (0,1)$. Then

$$\mathcal{S}_h(\mathcal{P}_h p) \to p \text{ in } \mathrm{L}^s(\Omega), \text{ if } h \to 0, \text{ for } s > 1. \tag{2.60}$$

Theorem 2 *Consider the problem (2.6). If $p_{ini} \in H^2(\Omega) \cap H_0^1(\Omega)$ then the solutions of semi-discrete scheme (2.50) converge in $L^2(0,T;L^2(\Omega))$ to the unique solution p of (2.6) for which*

$$p \in L^2(0,T;H^2(\Omega) \cap H_0^1(\Omega)), \quad \partial_t p \in L^2(0,T;L^2(\Omega)).$$

Proof The theory of ordinary differential equations implies existence and uniqueness of the maximal solution p^h on a time interval $[0,T_h)$, if $\bar{\omega}_h$ remains fixed. We derive a priori estimates allowing to show the convergence of p^h if $h \to 0$.

The necessary estimates are obtained in the same way as in Section 2.4 (a test by $\partial_t p^h$). Finally we get

$$\begin{array}{rclrcl} \bar{\nabla} p^h & \in & L^\infty(0,T;l^2(\omega_h)), & \bar{\nabla} p^h & \in & L^2(0,T;l^2(\omega_h)), \\ p^h & \in & L^\infty(0,T;l^4(\omega_h)), & p^h & \in & L^4(0,T;l^4(\omega_h)), \\ \partial_t p^h & \in & L^2(0,T;l^2(\omega_h)), & & & \end{array}$$

are bounded independently on h.
Let h^n be a sequence of mesh sizes tending to 0. It produces a sequence p^{h^n} of semi-discrete solutions to (2.50) which are defined on $[0,T)$. Then, $\bar{\nabla}_{h_n}\mathcal{P}_{h_n}p_{ini} \to \nabla p_{ini}$ in $L^2(\Omega)$ by (2.59) and $\mathcal{S}_{h_n}(\mathcal{P}_{h_n}p_{ini}) \to p_{ini}$ in $L^4(\Omega)$ by (2.60). Following (2.51), (2.52) and (2.53) we find a subsequence after a multi-step selection, that will be denoted again as n for which:

$$\begin{array}{rl} \{\mathcal{S}_{h^n} p^{h^n}\}_{n=1}^\infty & \text{converges weakly in } L^2(0,T;H_0^1(\Omega)), \\ \{\mathcal{S}_{h^n} \partial_t p^{h^n}\}_{n=1}^\infty & \text{converges weakly in } L^2(0,T;L^2(\Omega)), \\ \{\mathcal{Q}_{h^n} p^{h^n}\}_{n=1}^\infty & \text{converges weakly in } L^2(0,T;H_0^1(\Omega)), \\ \{\mathcal{Q}_{h^n} \partial_t p^{h^n}\}_{n=1}^\infty & \text{converges weakly in } L^2(0,T;L^2(\Omega)). \end{array}$$

Using compact imbedding theorem (Lemma 1) we have strong convergence of $\mathcal{Q}_{h^n}p^{h^n}$ in $L^2(0,T;L^2(\Omega))$ and using (2.54) we have the strong convergence of $\mathcal{S}_{h^n}p^{h^n}$ in the same space.

Lemma 9 *If p denotes the weak limit of $\mathcal{S}_h p^{h_n}$ in $L^2(0,T;L^2(\Omega))$, then $f_0(\mathcal{S}_h p^{h_n})$ converges weakly to $f_0(p)$ in $L^{4/3}(0,T;L^{4/3}(\Omega))$.*

Proof $S_{h_n} p^{h_n}$ converges strongly in $L^2(0,T;L^2(\Omega))$ according to the compact imbedding theorem. It can be considered to converge a.e. in this space (see [13]). Since $S_{h_n} p^{h_n}$ is bounded in $L^\infty(0,T;L^4(\Omega))$, we derive the estimate

$$\begin{aligned}
&\left\| f_0(\mathcal{S}_{h_n} p^{h_n}) \right\|_{L^{4/3}(\Omega)} \\
&= \left\| -\frac{1}{2}\mathcal{S}_{h_n} p^{h_n} + \frac{3}{2}(\mathcal{S}_{h_n} p^{h_n})^2 - (\mathcal{S}_{h_n} p^{h_n})^3 \right\|_{L^{4/3}(\Omega)} \\
&\le \frac{1}{2}\left\| \mathcal{S}_{h_n} p^{h_n} \right\|_{L^{4/3}(\Omega)} + \frac{3}{2}\|(\mathcal{S}_{h_n} p^{h_n})^2\|_{L^{4/3}(\Omega)} + \|(\mathcal{S}_{h_n} p^{h_n})^3\|_{L^{4/3}(\Omega)} \\
&\le \frac{1}{2}\left\| \mathcal{S}_{h_n} p^{h_n} \right\|_{L^{4/3}(\Omega)} + \frac{3}{2}\left\| \mathcal{S}_{h_n} p^{h_n} \right\|^2_{L^{8/3}(\Omega)} + \left\| \mathcal{S}_{h_n} p^{h_n} \right\|^3_{L^4(\Omega)}. \qquad (2.61)
\end{aligned}$$

That is why $f_0(S_{h_n} p^{h_n})$ is bounded in $L^\infty(0,T;L^{4/3}(\Omega))$. Applying Aubin–Lions lemma (see [25]) we get the final result. □

Lemma 10 *The sequence $\nabla \mathcal{Q}_{h_n} p^{h_n}$ converges strongly to ∇p in $L^2(0,T;L^2(\Omega;\mathbb{R}^2))$ and $\mathcal{S}_{h_n}|\bar{\nabla}_{h_n} p^{h_n}|$ converges weakly to $|\nabla p|$ in $L^2(0,T;L^2(\Omega;\mathbb{R}^2))$.*

Proof Analogous to the proof of Lemma 5. □

Using the above derived estimates and Lemmas 9 and 10 (for treating the nonlinear terms) we we will pass to the limit in the main problem. We multiply equation (2.50) by a test function $\mathcal{P}_{h_n} v$, where $v \in \mathcal{D}(\Omega)$ and integrate over ω_h. In terms of $L^2(\Omega)$ we have

$$\begin{aligned}
&\xi(\mathcal{S}_{h_n}\partial_t p^{h_n}, \mathcal{S}_{h_n}\mathcal{P}_{h_n} v) + \xi(g\nabla \mathcal{Q}_{h_n} p^{h_n}, \nabla \mathcal{Q}_{h_n}\mathcal{P}_{h_n} v) \\
&\quad = \frac{1}{\xi}(g f_0(\mathcal{S}_{h_n} p^{h_n}), \mathcal{S}_{h_n}\mathcal{P}_{h_n} v) + \xi(gF|\bar{\nabla}_{h_n} p^{h_n}|, \mathcal{S}_{h_n}\mathcal{P}_{h_n} v). \qquad (2.62)
\end{aligned}$$

We multiply (2.62) by a scalar function $\psi(t) \in \mathcal{C}^1[0,T]$, for which $\psi(T) = 0$ and integrate by parts

$$\begin{aligned}
&\xi(\mathcal{S}_{h_n} p^{h_n}(0), v)\psi(0) - \int_0^T \xi(\mathcal{S}_{h_n}\partial_t p^{h_n}, v)\dot{\psi}\mathrm{d}t \\
&\quad + \int_0^T \xi(g\nabla \mathcal{Q}_{h_n} p^{h_n}, \nabla v) - \frac{1}{\xi}(g f_0(\mathcal{S}_{h_n} p^{h_n}), v) - \xi(gF|\bar{\nabla}_{h_n} p^{h_n}|, v)]\mathrm{d}t = 0.
\end{aligned}$$

We use the previous convergence results and $\mathcal{S}_{h^n} p^{h_n}(0) = \mathcal{S}_{h^n}\mathcal{P}_{h^n} p_{ini}$. Finally we obtain

$$\begin{aligned}
&\xi(p_{ini}, w)\psi(0) - \int_0^T \xi(gp, w)\dot{\psi}\mathrm{d}t \\
&\quad + \int_0^T \xi(g\nabla p, \nabla w) - \frac{1}{\xi}(g f_0(p), w) - \xi(gF|\nabla p|, w)]\mathrm{d}t = 0.
\end{aligned}$$

If $\psi \in \mathcal{D}(0,T)$, we have

$$\xi \frac{\mathrm{d}}{\mathrm{d}t}(p,w) + \xi(g\nabla p, \nabla w) = \frac{1}{\xi}(gf_0(p), w) + \xi(gF|\nabla p|, w). \tag{2.63}$$

Regarding the satisfaction of the initial condition of the weak solution we multiply (2.6) by a scalar function $\psi(t) \in \mathcal{C}^1[0,T]$, for which $\psi(0) = 0$, integrating by parts and subtracting from (2.62), we have

$$(p_{ini} - p(0), w)\psi(0) = 0 \quad \forall w \in \mathcal{D}(\Omega), \tag{2.64}$$

that means $p(0) = p_{ini}$ in $L^2(\Omega)$.

□

2.5.2 Numerical scheme

The discretization is designed according to [4]. We approximate the initial–boundary–value problem (2.3) on a rectangular grid that corresponds with the initial image (MR image of size 512 x 512 pixels). Every picture element has a corresponding node in this grid. For the refinement of the grid we use bilinear interpolation of the initial picture data. Next, we will describe a semi-implicit[3] numerical scheme in a finite difference formulation[4].
We denote $p_{i,j}^k$ the value of $p(x,t)$ in the node $x = [ih_1, jh_2]$, in time $t = k\tau$, where τ is the time step of the numerical method. The discretization of the variables according to Section 2.5.1:

$$\begin{array}{lcl}
\frac{\partial p}{\partial t}|_{t=k\tau} & \rightarrow & \frac{p^k - p^{k-1}}{\tau} \\
\nabla p|_{i,j}^k & \rightarrow & \left(\frac{p_{i+1,j}^k - p_{i,j}^k}{h_1}, \frac{p_{i,j+1}^k - p_{i,j}^k}{h_2}\right) \\
\bar{\nabla} p|_{i,j}^k & \rightarrow & \left(\frac{p_{i,j}^k - p_{i-1,j}^k}{h_1}, \frac{p_{i,j}^k - p_{i,j-1}^k}{h_2}\right) \\
(\nabla \cdot g)|_{i,j} & \rightarrow & \left(\frac{g_{i+1,j}^1 - g_{i,j}^1}{h_1} + \frac{g_{i,j+1}^2 - g_{i,j}^2}{h_2}\right), \quad \text{kde} \quad g = (g^1, g^2)
\end{array}$$

After the discretization we get a system of nonlinear algebraic equation, that can be written in the form:

$$\xi \mathbf{A}\mathbf{p} - \frac{\tau}{\xi}\mathbf{f}(\mathbf{p}) = \xi \mathbf{F}, \tag{2.65}$$

[3]Semi-implicitness in sense that nonlinear terms of the equation are treated from the previous time step, the linear terms are considered on the current time level.

[4]Finite elements scheme is practically identical, for easy implementation we are describing the scheme based on finite differences.

where

$$\begin{aligned}
\mathbf{p} &= \left(p_{i,j}^k\right)_{i=1,j=1}^{N_1-1,N_2-1}, \\
\mathbf{Ap} &= \left(p_{i,j}^k - \tau\nabla\cdot\left(g\bar{\nabla}p^k\right)_{i,j}\right)_{i=1,j=1}^{N_1-1,N_2-1}, \\
\mathbf{f}(\mathbf{p}) &= \left(g_{i,j}f_0\left(p_{i,j}^k\right)\right)_{i=1,j=1}^{N_1-1,N_2-1}, \\
\mathbf{F} &= \left(p_{i,j}^{k-1} + \tau g_{i,j}F_{i,j}\left|\left(\bar{\nabla}p^{k-1}\right)_{i,j}\right|\right)_{i=1,j=1}^{N_1-1,N_2-1}.
\end{aligned}$$

We decompose a linear operator $\mathbf{A}$ into diagonal operator, lower and upper triangular operators, so that $\mathbf{A} = \mathbf{D} + \mathbf{L} + \mathbf{U}$.

$$\begin{aligned}
\mathbf{Dp} &= \left(p_{i,j}^k + \tau\left(\frac{g_{i+1,j}+g_{i,j}}{h_1^2} + \frac{g_{i,j+1}+g_{i,j}}{h_2^2}\right)p_{i,j}^k\right)_{i=1,j=1}^{N_1-1,N_2-1}, \\
\mathbf{Lp} &= \left(-\tau\frac{g_{i,j}}{h_1^2}p_{i-1,j}^k - \tau\frac{g_{i,j}}{h_2^2}p_{i,j-1}^k\right)_{i=1,j=1}^{N_1-1,N_2-1}, \\
\mathbf{Up} &= \left(-\tau\frac{g_{i+1,j}}{h_1^2}p_{i+1,j}^k - \tau\frac{g_{i,j+1}}{h_2^2}p_{i,j+1}^k\right)_{i=1,j=1}^{N_1-1,N_2-1}.
\end{aligned}$$

We solve (2.65) using Gauss-Seidel nonlinear iterative method in the form:

$$\xi(\mathbf{D}+\mathbf{L})\mathbf{p}^{l+1} = \xi\mathbf{F} - \left(\xi\mathbf{U}\mathbf{p}^l - \frac{\tau}{\xi}\mathbf{f}(\mathbf{p}^l)\right), \tag{2.66}$$

where the index l denotes number of the Gauss-Seidel iteration. For the initial guess we choose the previous time level:

$$\mathbf{p}^0 = \left(p_{i,j}^{k-1}\right)_{i=1,j=1}^{N_1-1,N_2-1}.$$

The size of the mesh either exactly corresponds with the size of the input MR image or we use bilinear interpolation for the mesh refinement.

2.6 Relationship to level-set methods

In this section we describe connection of the equation (2.3) to level–set methods. More detailed description is in [3]. The mean–curvature flow can be expressed by a law from differential geometry

$$v_\Gamma = -\kappa_\Gamma + F, \tag{2.67}$$

where v_Γ stands for a velocity of a motion of a closed curve Γ in $\mathbb{R}^2$, κ_Γ is a curvature of Γ and F has a meaning of an external force that influences

the motion. This is a central law for reasoning the segmentation models from Sections 2.2 and 2.3.

Describing the motion of the level set $\Gamma(t) = \{x \in \Omega : p(t,x) = 0\}$ under the law given by the equation (2.67), using the notation:

A normal to the level set Γ	...	$\vec{n_\Gamma} = -\frac{\nabla p}{\lvert\nabla p\rvert}$,
a normal velocity to the level set Γ	...	$v_\Gamma = \frac{1}{\lvert\nabla P\rvert} \cdot \frac{\partial p}{\partial t}$,
the mean curvature of Γ	...	$\kappa_\Gamma = \nabla \cdot (\vec{n_\Gamma}) = -\nabla \cdot \frac{\nabla p}{\lvert\nabla p\rvert}$.

We obtain a level set equation:

$$\frac{\partial p}{\partial t} = |\nabla p| \, \nabla \cdot \frac{\nabla p}{|\nabla p|} + F, \tag{2.68}$$

which describes mean curvature flow of level sets. The segmentation model (2.1) described in section 2.2 is based on the equation (2.68).

Now, the Allen–Cahn equation (2.3) in a context of the law described by (2.68):

For $\xi \to 0_+$ the level set $\Gamma(t) = \{x \in \Omega : p(t,x) = \frac{1}{2}\}$ is evolving under a law of the mean–curvature flow. Connection of the problem (2.3) to the law described by the equation (2.67) for $\xi \to 0_+$ can be expressed by the scheme:

$$\begin{array}{ccccccc} \underbrace{\xi \frac{\partial p}{\partial t}} & = & \underbrace{\xi \nabla \cdot (\nabla p) + \frac{1}{\xi} f_0(p)} & + & \underbrace{\xi F |\nabla p|.} & & \\ \downarrow & & \downarrow & & \downarrow & & \\ v_\Gamma & = & -\kappa_\Gamma & + & F & & \end{array}$$

2.7 Cardiac MRI data segmentation using the Allen–Cahn equation

To apply the model described in previous sections for the segmentation of the real cardiac MRI data we have to specify correct values of parameters of the equation (2.3). We also describe some modifications that increase the efficiency of the segmentation procedure.

2.7.1 The parameter λ

Information from the input image enters the model by means of the Perona–Malik function g (see [23]). The argument of the function g is the spatial

gradient of the image intensity signal ($|\nabla P_0|$). High values of $|\nabla P_0|$ correspond with the edges in the image. The property $g(|\nabla P_0|) \to 0$ for $|\nabla P_0| \to +\infty$ causes the edge detection.

The usual choice for the Perona–Malik function is:

$$g(s) = \frac{1}{1 + \lambda s^2}, \tag{2.69}$$

where λ is a parameter. The sensitivity of the edge detector depends on the value of this parameter λ. The smaller the parameter λ is, the more sensitive is the detector given by the equation (2.3). This means that too low value of λ can cause not detection of the edge. On the other hand, very high value of λ can cause detection of spurious edges which are caused mainly by inhomogeneities of the signal due to the limited signal-to-noise ratio, blood flow artifacts, etc. Not optimal choices of the parameter λ are shown in Figure 2.5.

The equation (2.3) has the intrinsic smoothing property. It causes the boundary of the segmented area to be smooth. This is an important property for the practical application on the segmentation of cardiac MR images. In these images the inhomogeneities can even cause partial edge missing (again due to the limited signal-to-noise ratio and also due to the limited time resolution). Due to this smoothing property, the resulted segmented area can be very close to partially missing edge. For the keeping of the smoothing property of the equation (2.3), the parameter λ has to be low enough. At the same time it has to be chosen high enough, so that the edges will be detected (see Figures 2.5(b) and 2.6).

In our work we finally used values $5 < \lambda < 30$. These values makes the boundary of the resulted segmented area to be smooth. We raised the proper detection of the edges by varying value of parameters λ and F over the image domain. The magnitude of the parameter λ in a spatial point may be dependent on the variability of the input signal in this point and in its small neighborhood. In case of the higher signal variability (the higher probability of the edge presents) the higher magnitude of the parameter λ is chosen. We deal with the varying of the parameter F in the next section.

2.7.2 The external force F and automatically given initial segmented area p_{ini}

The velocity of the expansion or the shrinkage of the segmented area is given by the equation (2.67). In this section we explain the meaning of the member including F.

According to the law $v_\Gamma = -\kappa + F$ (see Section 2.6), F has the meaning of the external force that influence the evolution process. Depending on the

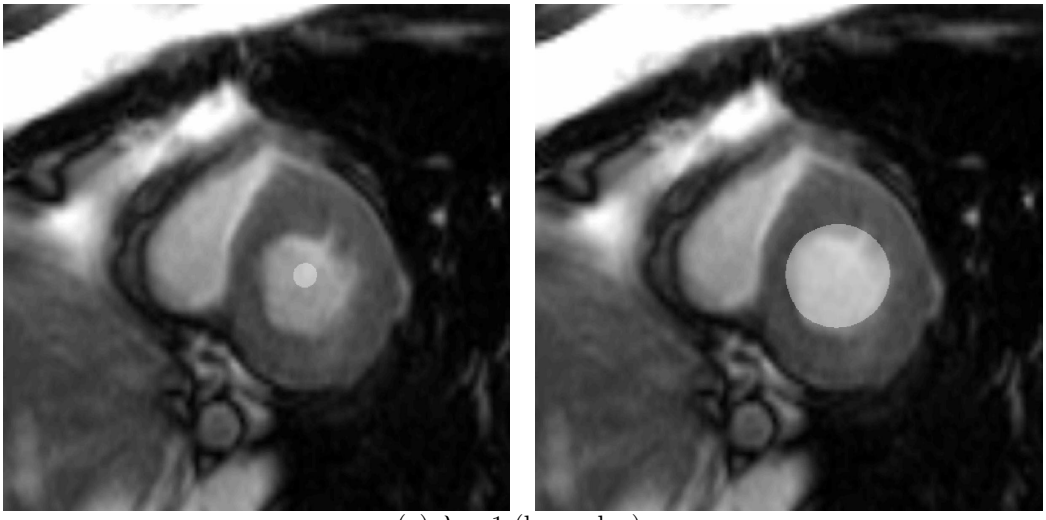

(a) $\lambda = 1$ (low value).

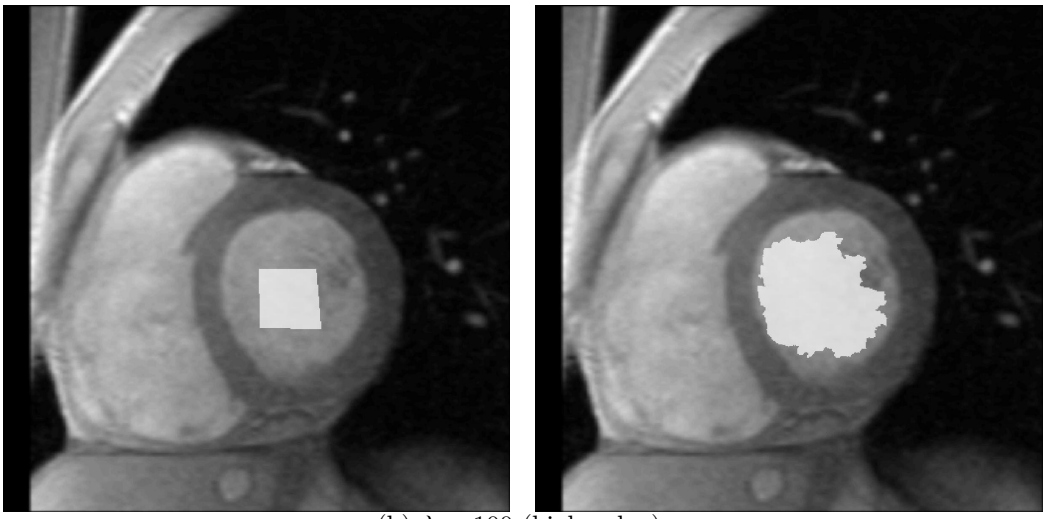

(b) $\lambda = 100$ (high value).

Figure 2.5: The evolution with not optimal parameter λ. On the left – initial segmented area p_{ini}, on the right result of the segmentation. In case (a) low value of λ caused not detection of the inner contour of the myocardium, in case (b) high value of λ caused detection of spurious edges (resulted segmented area has 'non-smoothed' boundary).

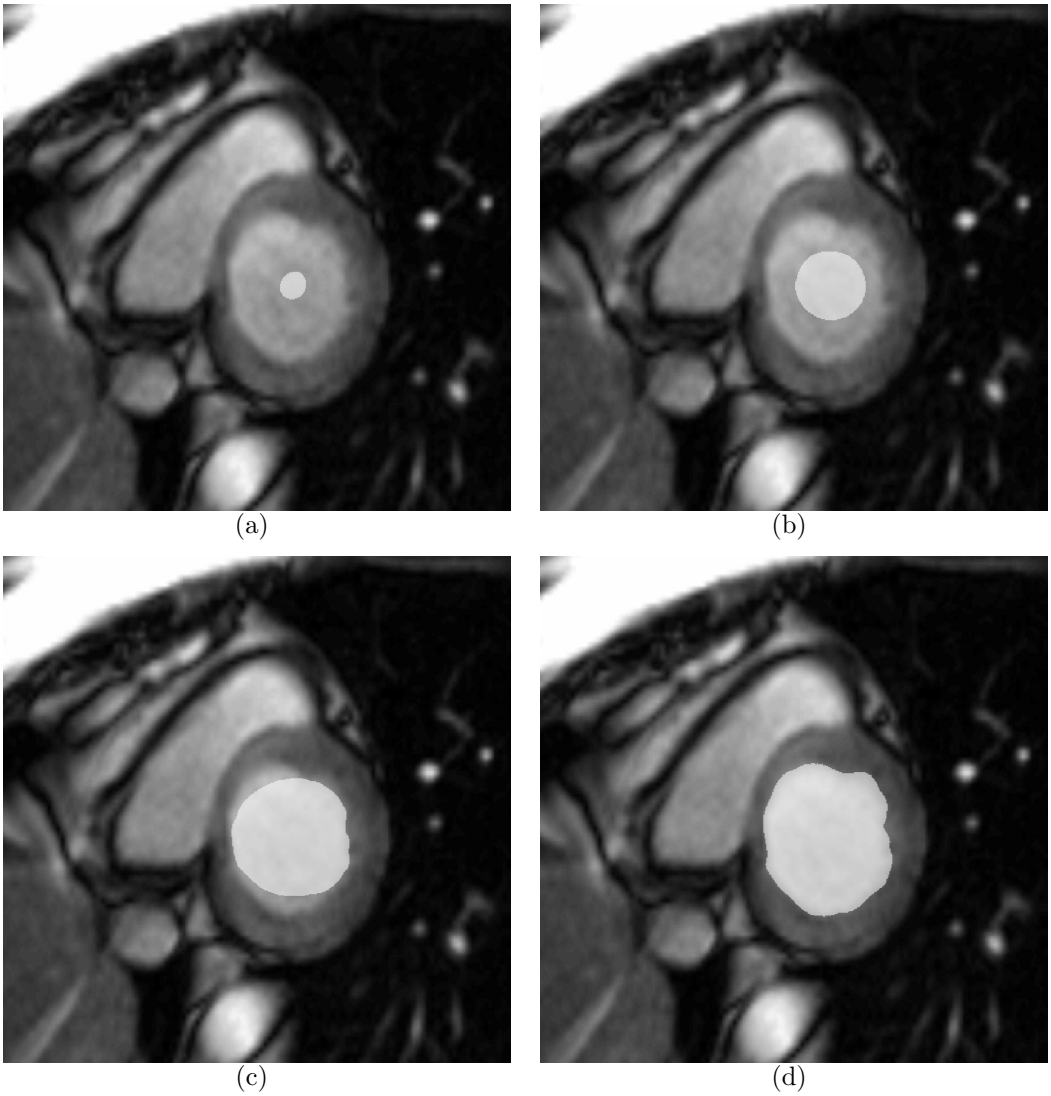

Figure 2.6: Evolution of the segmented area from (a) to (d) according to equation (2.3) with $\lambda = 30$. Smoothing property is present.

signature of v_Γ, the segmented area either expands or shrinks. The velocity of the evolution of the segmented area is given by the magnitude of v_Γ.

For the constant value of F over the whole domain Ω (input image) the initial segmented area p_{ini} must either cover the whole object of interest (then the initial area shrinks to the edges) or it must be localized inside the segmented object (initial area then expands to the edges, see Figure 2.7).

In Figure 2.8 the initial segmented area covers part of the ventricle volume and part of the ventricle wall myocardium and the external force F remains constant over the image. Locally the detector has found some edges. These edges are either part of the inner or of the outer contour of the myocardium. Since we need to detect the whole inner contour of the myocardium (or the whole outer contour respectively), the ventricle was not finally segmented.

In case of the cardiac MR images segmentation the initial segmented area has to be given automatically from the known segmentations of the neighbouring images (in either time or spatial domain). Images of different slices are obtained in different breath-hold of the examined subject. Since the breath-hold is not absolutely reproducible, the neighbouring slices are not exactly aligned one to another. That is why the automatically given initial segmented area p_{ini} is not of the type as depicted in Figure 2.7 but often of the less convenient type as in Figure 2.8. These figures explain the reason why the value of F cannot be constant in the whole image domain.

In the cardiac MR images obtained using so called bright blood technique (see [9], pages 61–62), the blood in the ventricle is lighter than the myocardium or the surrounding tissue. Using the information that the blood has the highest intensity and the surrounding lung tissue the lowest intensity we can set a threshold I_{in} for the picture elements certainly inside the ventricle and a threshold I_{out} for picture elements certainly in the lung tissue.

Then we can define F in case of the ventricle volume segmentation by the following formula:

$$F(x) = \begin{cases} -1 & \text{in } \{x \in \Omega; P_0(x) > I_{in}\} \\ 2 & \text{elsewhere,} \end{cases} \tag{2.70}$$

and F in case of the ventricle volume segmentation by the formula:

$$F(x) = \begin{cases} -1 & \text{in } \{x \in \Omega; P_0(x) < I_{out}\} \\ 2 & \text{elsewhere.} \end{cases} \tag{2.71}$$

By this definition we modify the model (2.3), so that the segmentation process is not dependent only on the spatial gradient of the input image signal but also on the magnitude of the input signal. Thanks to this modification we obtain a model which contains the movement by mean curvature in means of

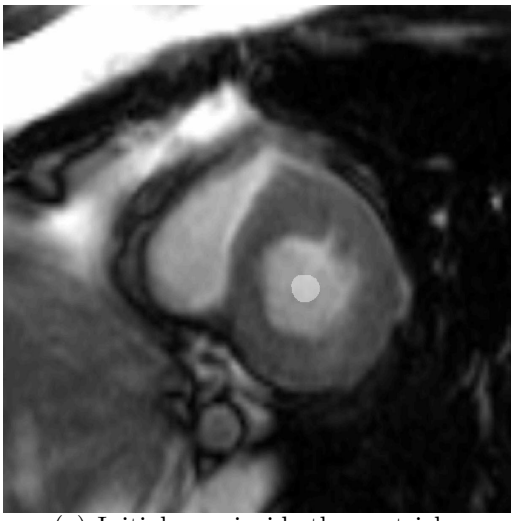

(a) Initial area inside the ventricle.

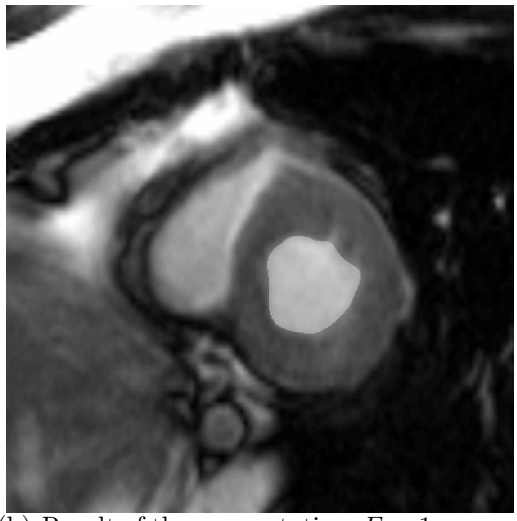

(b) Result of the segmentation, $F = 1$, expansion of p_{ini}.

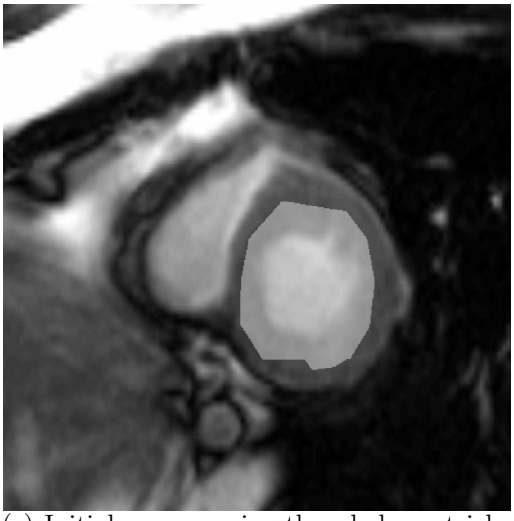

(c) Initial area covering the whole ventricle.

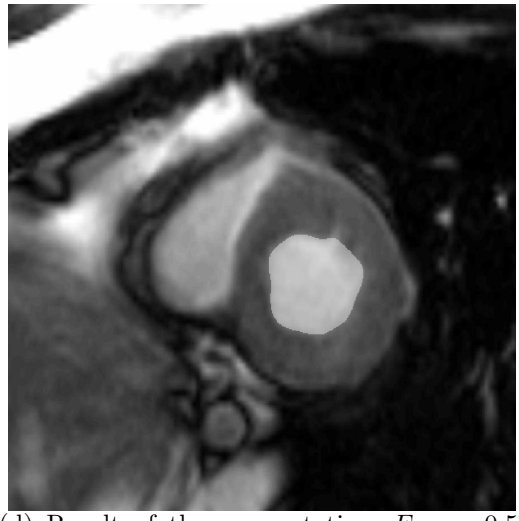

(d) Result of the segmentation, $F = -0.5$, shrinkage of p_{ini}.

Figure 2.7: Successful segmentation with constant value F over the image.

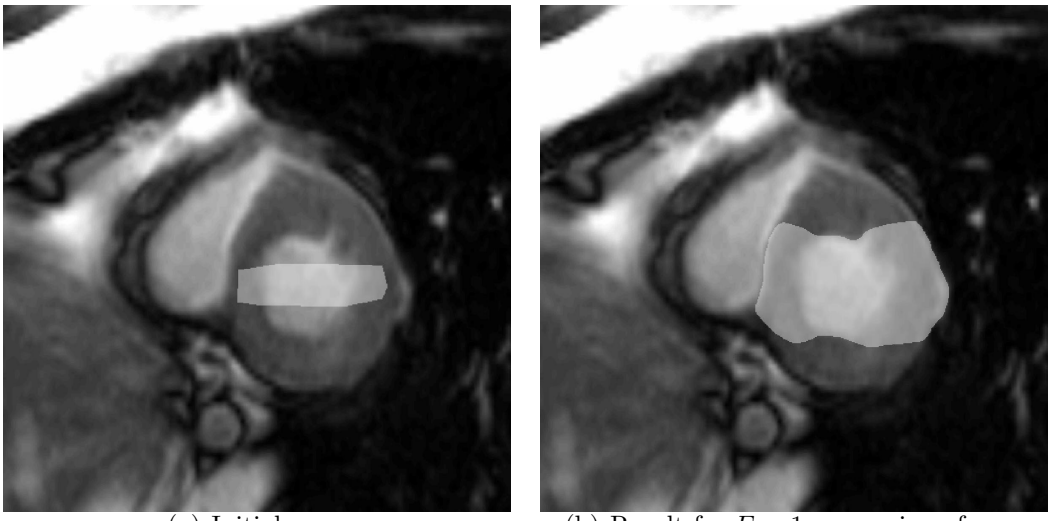

(a) Initial area.

(b) Result for $F = 1$, expansion of p_{ini}.

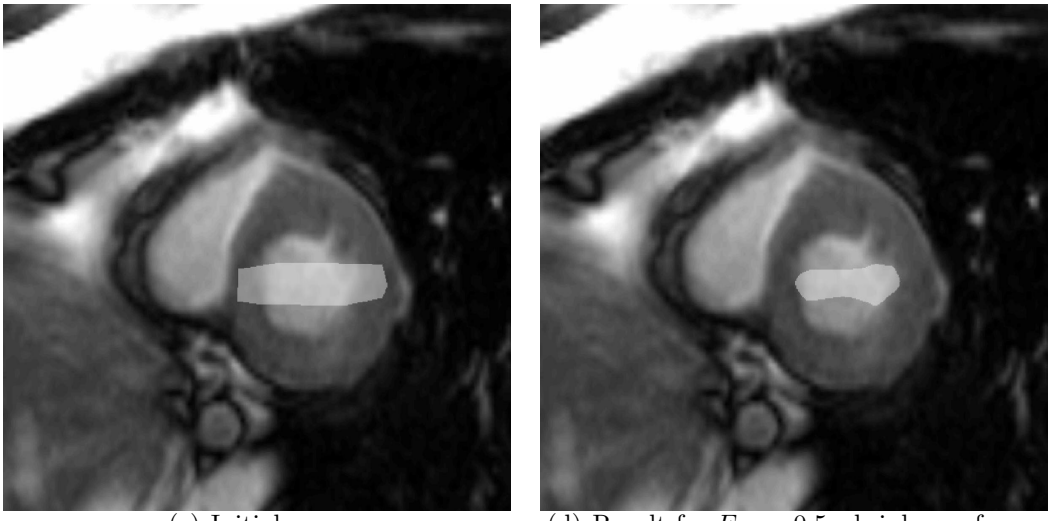

(c) Initial area.

(d) Result for $F = -0.5$, shrinkage of p_{ini}.

Figure 2.8: Unsuccessful segmentation with constant value F over the image.

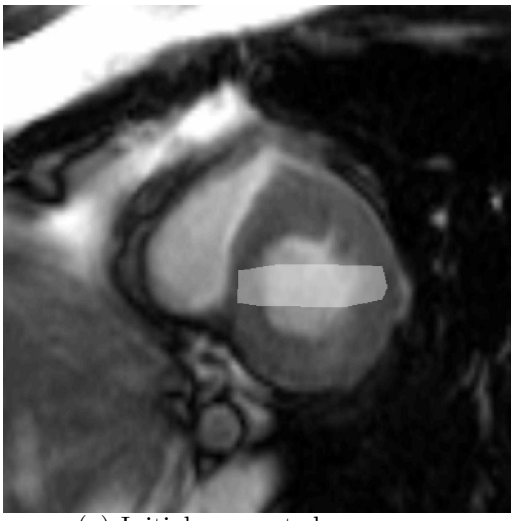

(a) Initial segmented area p_{ini}.

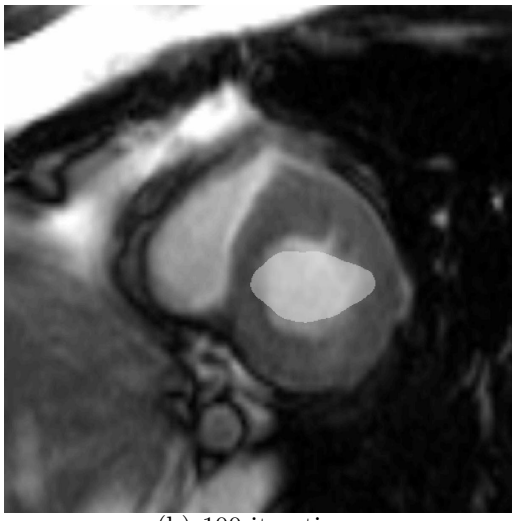

(b) 100 iterations

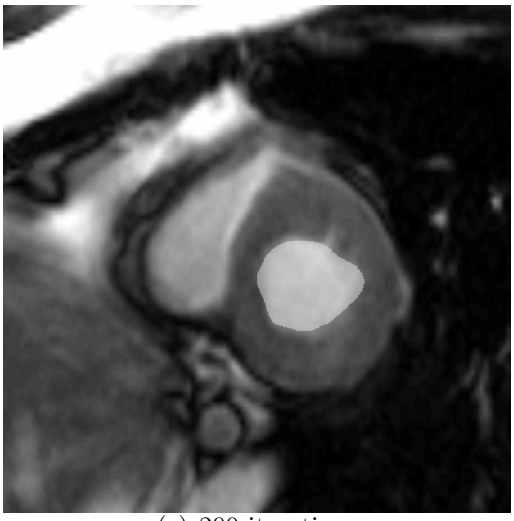

(c) 200 iterations

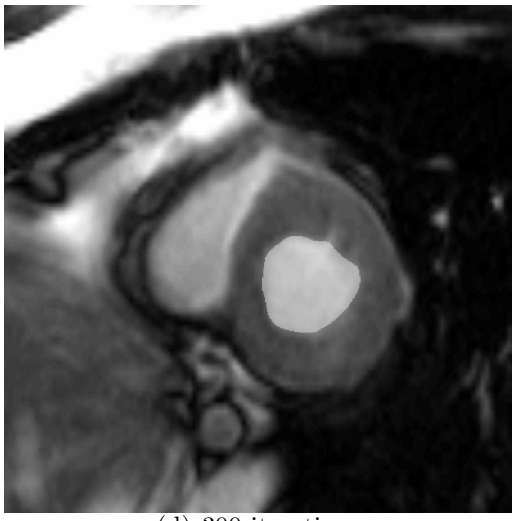

(d) 300 iterations

Figure 2.9: Segmentation with non-constant external force F. F is dependent on the intensity of the image data.

(a) Morphological image (values of intensity in the image pixels are between 0 and 255).

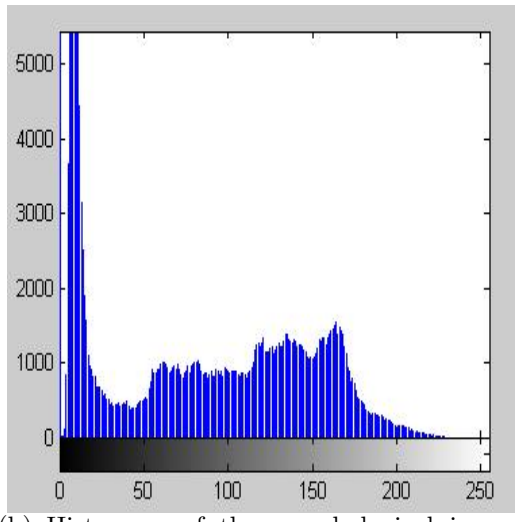

(b) Histogram of the morphological image. Frequency of image pixels (y-axis) with a given intensity from 0 to 255 (x-axis).

Figure 2.10: The image histogram does not show a clear border between signal intensities of different tissues (e.g. between myocardium and lung tissue or between myocardium and blood inside the ventricle).

PDEs and also less sophisticated segmentation methods based on the histogram analysis (see [27], chapter 6). At the same time, Figure 2.10 depicts that the image histogram analysis itself would not get a sufficient result in case of cardiac MRI data. In Figure 2.9 is shown the successful segmentation process that started from the same initial area as segmentation in Figure 2.8 using the modification (2.71).

2.7.3 Stopping criterion

The edge detector is based on the numerical solution of the evolution partial equation (see Section 2.5). Using the numerical solver we estimate the evolution of the approximate solution from the initial condition $p(0, x) = p_{ini}(x)$ with the time step τ. In this section we deal with the problem when to stop the evolving process. By the caption *stopping criterion* we mean how many time iterations have to be proceeded, so that finally the desired area will be segmented.

Generally there are two possibilities for the stopping criterion. The first one is to proceed predefined (fixed) number of iterations, the second one is to stop the evolution when the area will not evolve anymore. In our case the both approaches have advantages and disadvantages at the same time.

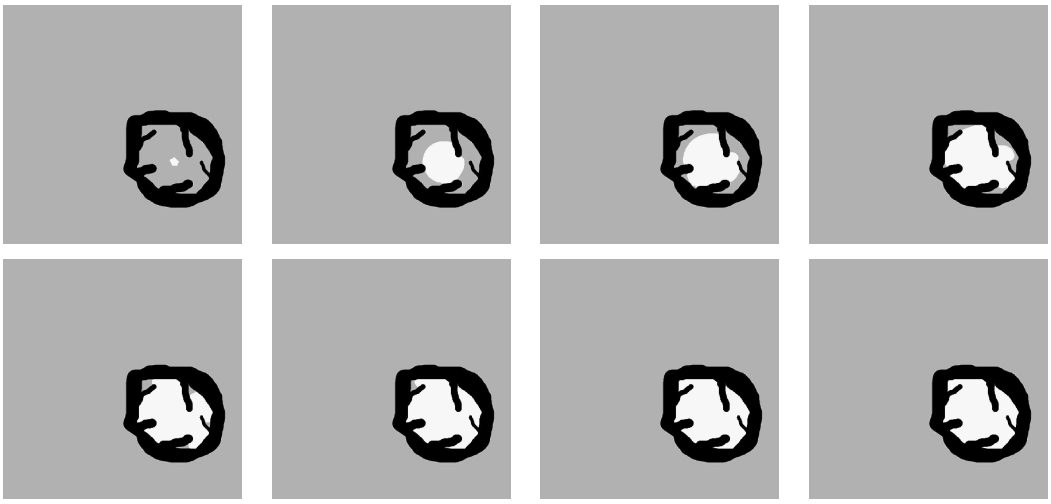

Figure 2.11: Evolution of the initial area p_{ini} according to equation (2.3), evolution time from 0 to 6 (time step τ times number of time iterations), matrix 1024 times 1024, $\xi = 0.05$, $h = 0.04$, $\lambda = 10$, $F = 5$. The evolution of the area entirely ceases in the artificial image.

Since all the images from single examination are of the similar image characteristics, we can use the predefined number of time iterations. We can estimate the number of time iterations needed for proper segmentation from the first image and then we can use this value as a fixed number of time iterations for all other images.

The better possibility is to use the automatic stopping criterion. It means to terminate the process automatically when the evolution of the segmented area ceases. Typically the computation is stopped as soon as the following inequality for the discrete values of the segmentation function holds (see [29]):

$$\frac{1}{M}\sum_{i,j}|p_{i,j}^{k+1} - p_{i,j}^{k}| \leq C\tau h^2, \tag{2.72}$$

the sum is over all grid points, M denotes the total number of grid points.

This access is entirely successful in an artificial data segmentation (see Figure 2.11 and [4]) where we do not face the problem with imperfect or even missing edges as in real MR images. In our case, such predefined threshold for ceasing the process as (2.72) is too strict. Especially low signal-to-noise ratio, limited time resolution between images and presence of the papillary muscles close to the ventricle wall (see Section 3.3) cause that although the evolution process slow down near the edges of the segmented objects, usually it does not completely stop.

In our work we finally implemented easier stopping criterion. Every N iterations (usually N is 100) we estimate the segmented area (by counting the number of pixels in the area) and compare it with the estimated area before N iterations. When the relative difference is less than certain threshold (for example less than 2% or 5%), the evolution is terminated. We also define maximal number of time iterations. After these iterations the evolution is terminated in either case. This type of the criterion with 5% threshold was used in the computation of Figures 2.7 and 2.9.

Chapter 3

Results

We implemented the segmentation algorithm from Section 2.5 in the C language. The user interface is written in MATLAB. The image data were obtained using cardiac MR images of volunteers and patients from the MR departments of hospitals IKEM[1] Prague, Na Homolce[2] Prague and Hradec Králové[3].

In this chapter we demonstrate application of the segmentation algorithm to the data from cardiac MR images obtained by MR acquisition sequences denoted as the FLASH and the trueFISP (see Section 1.2).

3.1 Segmentation of the left heart ventricle volume

We segment volume of the ventricle throughout whole cardiac cycle in an automated way.

For each image (all slices and all time frames) we use initial segmented area p_{ini} derived from the resulted segmented area of the neighbouring images (either in temporal or spatial domain). We apply numerical solver of the model governed by the equation (2.3) with an automatically given initial segmented area p_{ini} and with the choice of parameters λ, F, stopping time T according to Section 2.7.

After the ventricle segmentation of all the slices throughout the cardiac cycle, the dynamics of the ventricle volume can be described by summing the segmented areas over the left heart ventricle (see Figure 1.8). From these values a global parameter of heart contractility – *ejection fraction of the ventricle (EF)* – can be estimated (see Section 1.4.1).

[1] `http://www.ikem.cz/`
[2] `http://www.homolka.cz/en/`
[3] `http://www.fnhk.cz/`

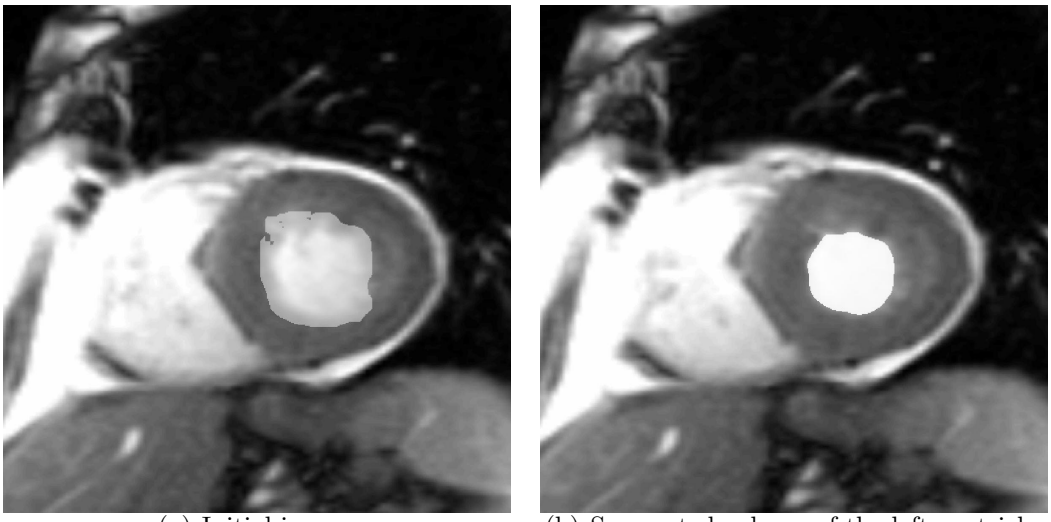

(a) Initial image. (b) Segmented volume of the left ventricle.

Figure 3.1: **Subject 01.** Example of the left heart ventricle volume segmentation. Image corresponding to the end-systole. On the left, p_{ini} automatically derived from the previous slice image, on the right the result of segmentation. Parameters of equation (2.3): $\xi = 0.09$, $\lambda = 6$, $F = -1$, time step $\tau = 0.005$. Maximal number of time iterations: 500 (according to Section 2.7.3).

Analysis of data obtained by the trueFISP imaging sequence

We describe more in detail the automated selection of the initial segmented area p_{ini}.

In each slice we start with segmentation of the image corresponding to the end-systole (minimal volume of the ventricle, see Section 1.3). As the initial area p_{ini} for this time frame image we use the segmented end-systolic image of the previous slice (see Figure 3.1). Then we proceed in segmentation of images for other time frames throughout systolic and diastolic phase of the cardiac cycle. As the initial segmented area p_{ini} we use the segmented area from the next time frame (in case of the images from the systolic phase), or the previous time frame (in case of the images from the diastolic phase, see Figures 3.2 and 3.3).

In Figures 3.1, 3.2 and 3.3 we present selected images of the heart for a patient with a good contracting ability of the myocardium. The images were obtained using the modern trueFISP acquisition sequence (see Section 1.2). We performed a few simulations with image data of this patient with different choice of the parameter λ and different accuracy of a stopping-criterion (see Figures 3.4 and 3.5), where resulted volumes of the left ventricle during a cardiac cycle are depicted). In Figure 3.6 selected images after automated segmentation

of the left ventricle of another patient are shown. Estimated volume versus time graphs are in Figure 3.9.

We explore the fact, that the quality of data obtained by the trueFISP imaging sequence is high over the whole cardiac cycle. This is the reason why we can start the segmentation from the end-systolic images. The situation differs in the images acquired by the FLASH sequence where the end-systolic images are degraded by flow artifacts (see Figure 1.3). The described algorithm of the automated choice of the initial segmented area p_{ini} is robust in the trueFISP data processing and the automated segmentation of the whole heart gives good results (see Table 3.1 and Figure 3.11). In the optimal situation, only one end-diastolic time frame (in the first slice) has to be segmented manually. That is one manual segmentation in hundreds of images segmented automatically afterwards.

Analysis of the data obtained by the FLASH imaging sequence
For this type of data we have to modify the strategy for the automated choice of the initial segmented area p_{ini}. Due to strong artifacts from the flowing blood inside the ventricle during the myocardial contraction, it is impossible to use the end-systolic image as a base for the segmentation of other time frame images (see Figure 1.3). On the contrary, the end-diastolic images have the highest quality with respect to the flow artifacts. That is why we segment them in a first order and then we continue with the other time frame images in successive steps. Unfortunately, manual corrections are necessary even in image data of high quality.

Selected images of two examined subjects using the FLASH acquisition sequence are depicted in Figures 3.7 and 3.8, subsequent estimates of volume versus time graphs in Figure 3.9. In case of the data presented in Figures 3.7 (well co-operating healthy volunteer) approximately 20% of the segmented images from the whole heart had to be corrected manually, the remaining images were segmented satisfactorily. Nevertheless, speedup of the processing (if compared with a fully manual access) for these high quality images was significant. Regarding the FLASH images of usual or lower quality, the presented algorithm is less effective in an automated ventricle segmentation.

Analysis of the image data in real clinical examinations
The ejection fraction is a parameter of great clinical interest. It is no doubt that this value has to be estimated as accurately as possible. The ejection fraction depends only on the end-systolic and the end-diastolic volumes (see Section 1.4.1). That is why we need correct segmentation of the end-systolic and the end-diastolic images. For the clinical data evaluation we use one of the two following approaches.

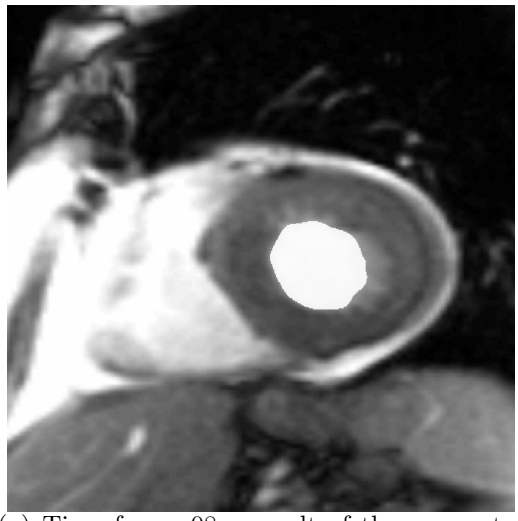

(a) Time frame 08 – result of the segmentation as an initial segmented area p_{ini} for Time frame 09.

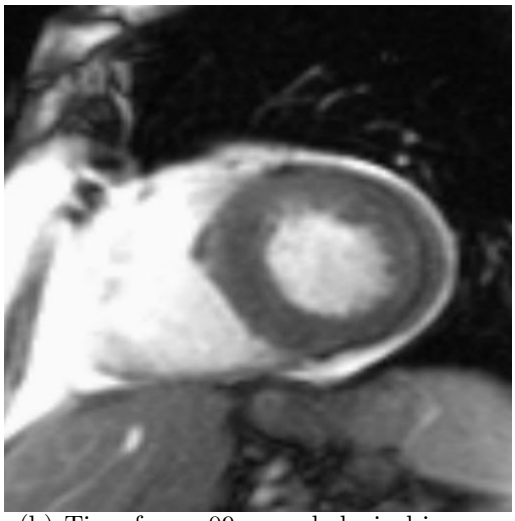

(b) Time frame 09, morphological image.

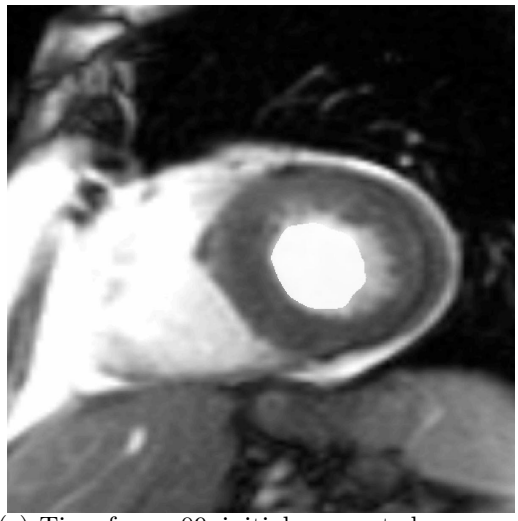

(c) Time frame 09, initial segmented area p_{ini} derived from (a).

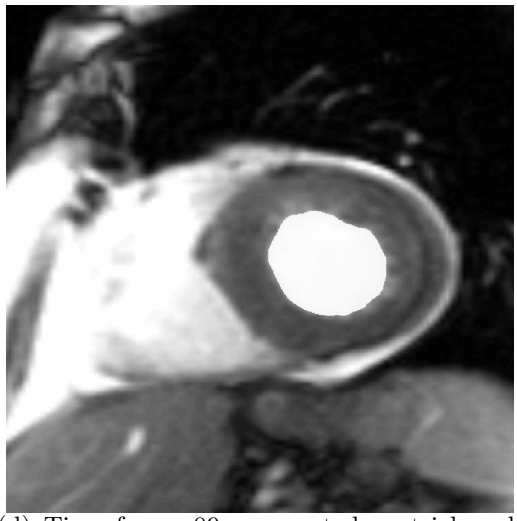

(d) Time frame 09, segmented ventricle volume.

Figure 3.2: **Subject 01.** Segmentation of Time frame 09 (image corresponding to the contracted heart). The initial segmented area p_{ini} is derived from segmented Time frame 08 depicted in (a). Parameters of equation (2.3): $\xi = 0.09$, $\lambda = 6$, $F = -1$, time step $\tau = 0.005$. Maximal number of time iterations: 500 (according to Section 2.7.3).

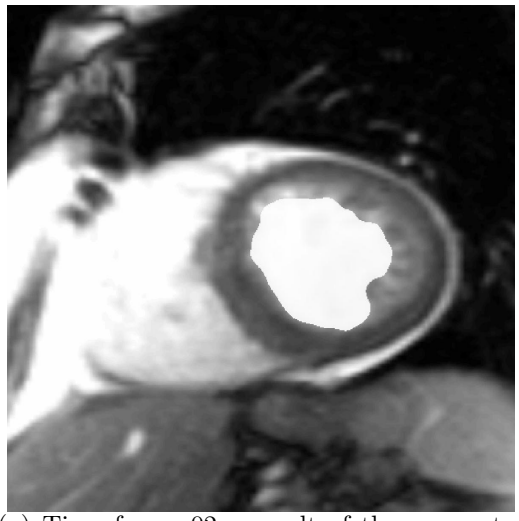

(a) Time frame 02 – result of the segmentation as an initial segmented area p_{ini} for Time frame 01.

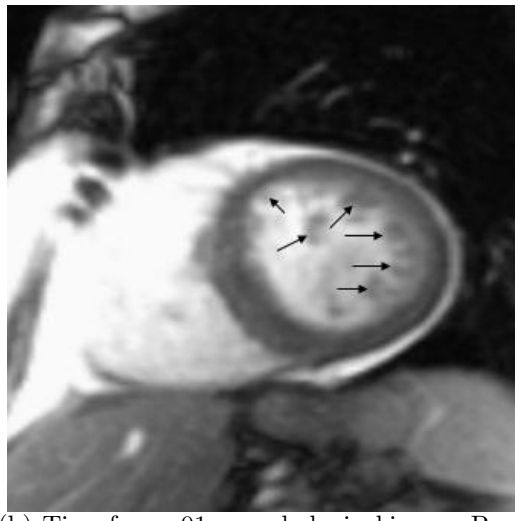

(b) Time frame 01, morphological image. Papillary muscles and non-smooth surface of the cavity marked with arrows.

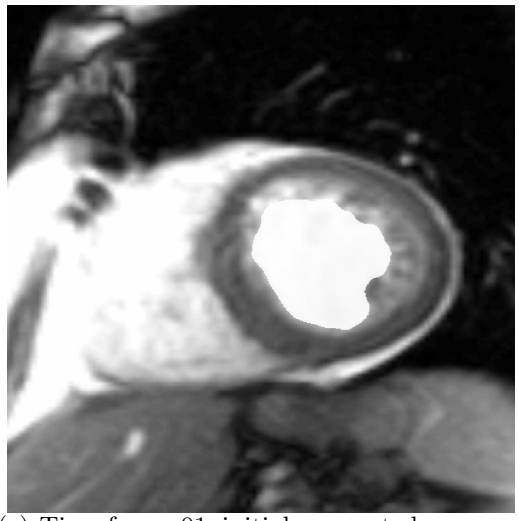

(c) Time frame 01, initial segmented area p_{ini} derived from (a).

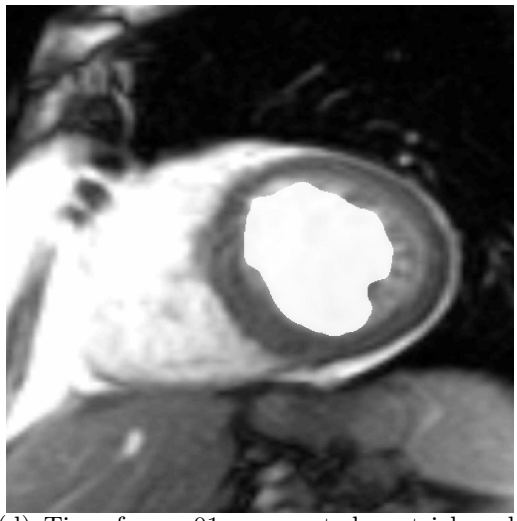

(d) Time frame 01, segmented ventricle volume.

Figure 3.3: **Subject 01.** Segmentation of Time frame 01 (image corresponding to the end-diastole – maximal volume of the ventricle). The initial segmented area p_{ini} is derived from segmented Time frame 02 depicted in (a). The non-smooth surface of the cavity causes difficulties with detection of the inner contour of the ventricle (even in case of the manual segmentation). Parameters of equation (2.3): $\xi = 0.09$, $\lambda = 6$, $F = -1$, time step $\tau = 0.005$. Maximal number of time iterations: 500 (according to Section 2.7.3).

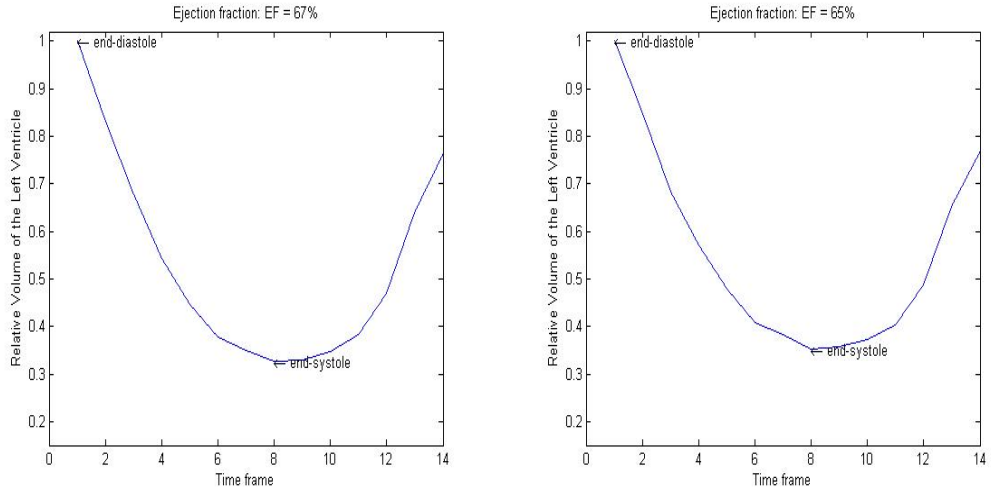

(a) $\lambda = 6$ (b) $\lambda = 30$

Figure 3.4: **Subject 01.** Comparison of the estimates of volume versus time graphs for two values of $\lambda = 6$ and $\lambda = 30$ for the same patient (image data from Figures 3.1, 3.2 and 3.3). Difference in the resulted ejection fraction is caused by the problematic detection of the inner contour of the ventricle in the slices corresponding to the base of myocardium during end-diastole (see Figure 3.3). Parameters of equation (2.3): $\xi = 0.09$, $F = -1$, time step $\tau = 0.005$.

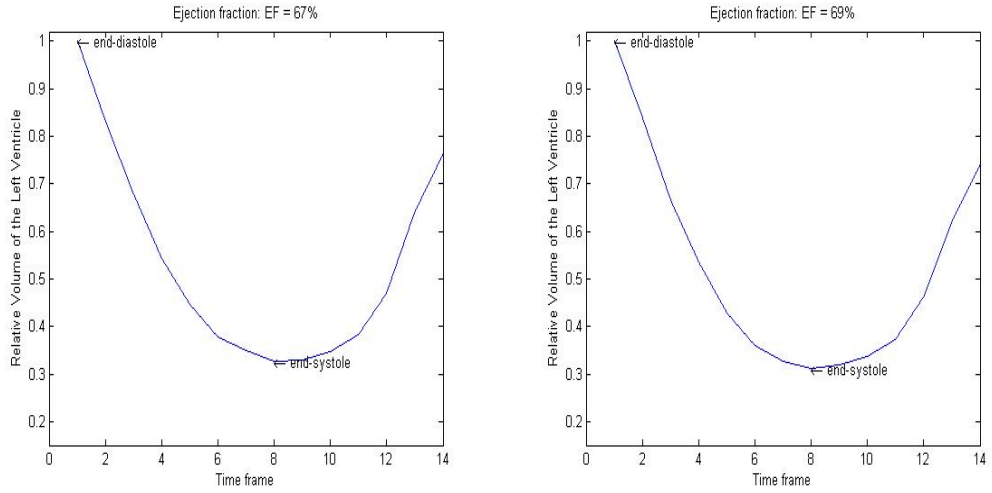

(a) Stopping criterium 5% (b) Stopping criterium 2%

Figure 3.5: **Subject 01.** Comparison of the estimates of volume versus time graphs with different accuracy of the stopping criterion (relative change of the segmented area in 100 successive time iterations of the numerical solver, see Section 2.7.3). Both shows similar results. Parameters of equation (2.3): $\lambda = 6$, $\xi = 0.09$, $F = -1$, time step $\tau = 0.005$.

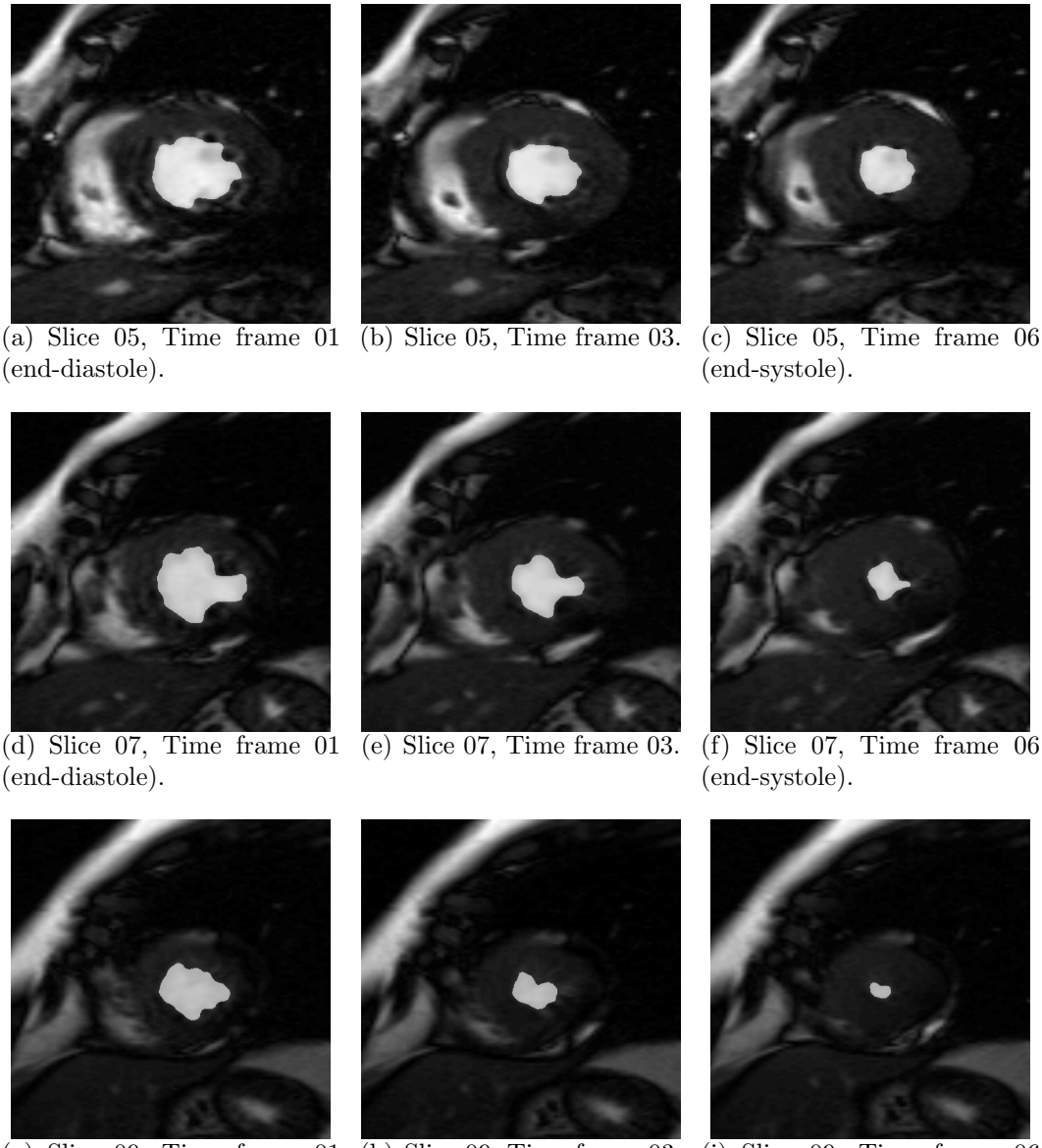

(a) Slice 05, Time frame 01 (end-diastole). (b) Slice 05, Time frame 03. (c) Slice 05, Time frame 06 (end-systole).

(d) Slice 07, Time frame 01 (end-diastole). (e) Slice 07, Time frame 03. (f) Slice 07, Time frame 06 (end-systole).

(g) Slice 09, Time frame 01 (end-diastole). (h) Slice 09, Time frame 03. (i) Slice 09, Time frame 06 (end-systole).

Figure 3.6: **Subject 02.** The trueFISP sequence. Selected images from the systolic phase of the cardiac cycle. Parameters of equation (2.3): $\xi = 0.09$, $\lambda = 30$, $F = -1$, time step $\tau = 0.005$. Maximal number of time iterations: 500 (according to Section 2.7.3).

(a) Slice 03, Time frame 01 (end-diastole).

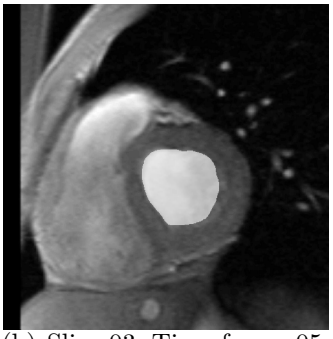

(b) Slice 03, Time frame 05.

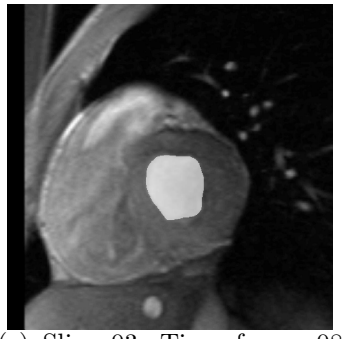

(c) Slice 03, Time frame 08 (end-systole).

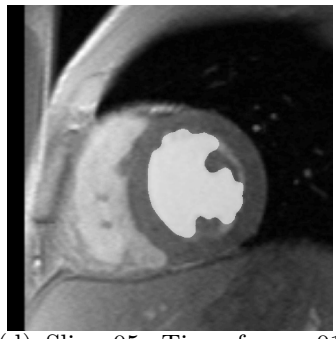

(d) Slice 05, Time frame 01 (end-diastole).

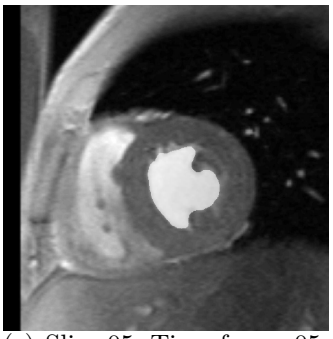

(e) Slice 05, Time frame 05.

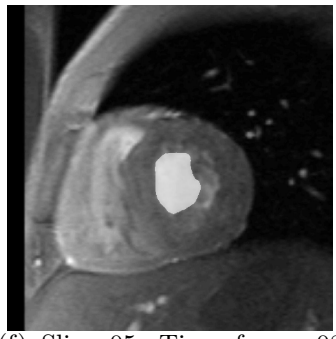

(f) Slice 05, Time frame 08 (end-systole).

(g) Slice 07, Time frame 01 (end-diastole).

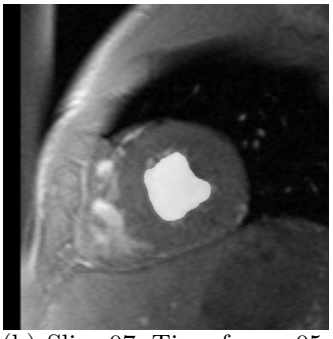

(h) Slice 07, Time frame 05.

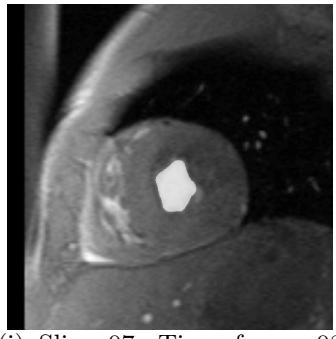

(i) Slice 07, Time frame 08 (end-systole).

Figure 3.7: **Subject 03.** The FLASH sequence. Selected images from the systolic phase of the cardiac cycle. Parameters of equation (2.3): $\xi = 0.09$, $\lambda = 6$, $F = -1$, time step $\tau = 0.005$. Maximal number of time iterations: 500 (according to Section 2.7.3).

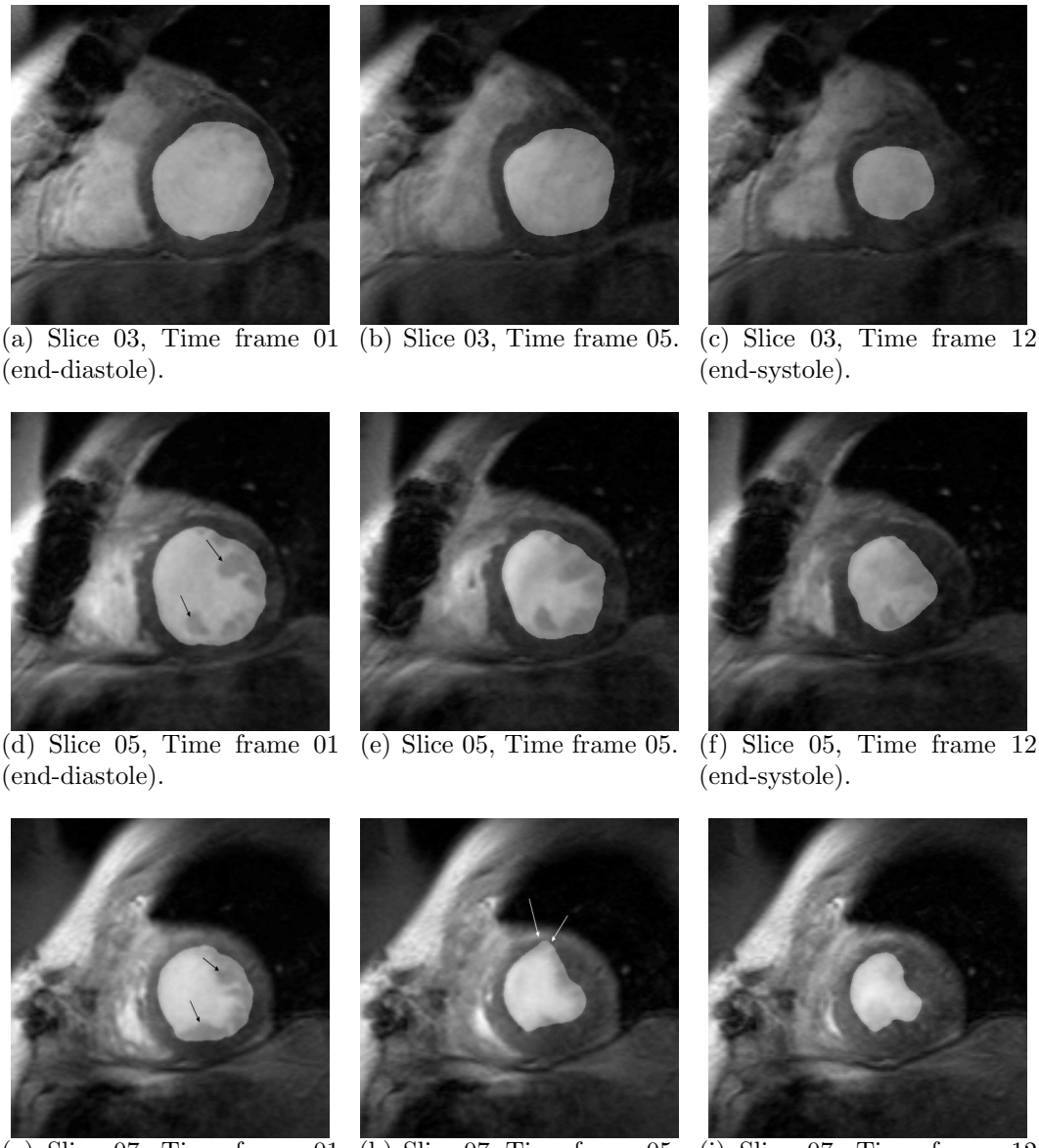

(a) Slice 03, Time frame 01 (end-diastole). (b) Slice 03, Time frame 05. (c) Slice 03, Time frame 12 (end-systole).

(d) Slice 05, Time frame 01 (end-diastole). (e) Slice 05, Time frame 05. (f) Slice 05, Time frame 12 (end-systole).

(g) Slice 07, Time frame 01 (end-diastole). (h) Slice 07, Time frame 05. (i) Slice 07, Time frame 12 (end-systole).

Figure 3.8: **Subject 04.** The FLASH sequence. Selected images from the systolic phase of the cardiac cycle. Wall thinning in the apical anteroseptal segment (Slice 07) causes difficulties with the segmentation (white arrows). Not proper segmentation of the papillary muscles (black arrows in the first time frames) finally causes overestimation of the ejection fraction (see Table 3.1). Parameters of equation (2.3): $\xi = 0.09$, $\lambda = 6$, $F = -1$, time step $\tau = 0.005$. Maximal number of time iterations: 500 (according to Section 2.7.3).

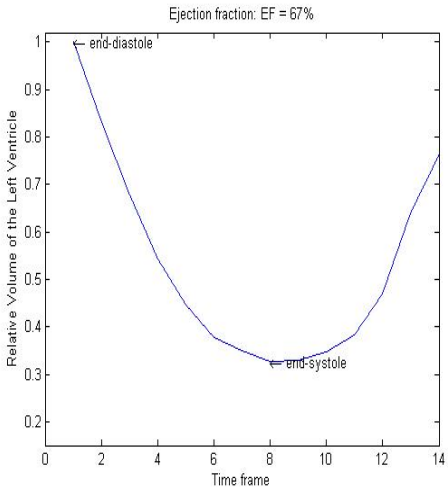

(a) Subject 01, EF = 67% (normal value).

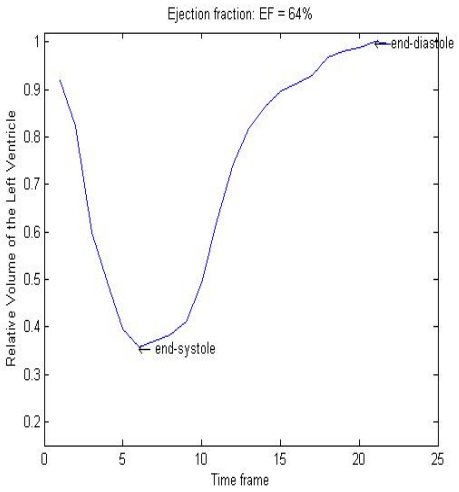

(b) Subject 02, EF = 64% (normal value).

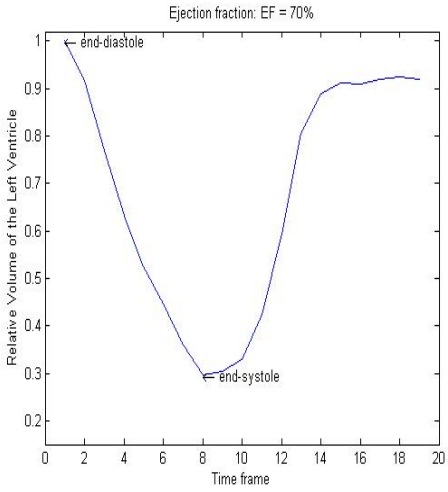

(c) Subject 03, EF = 70%(normal value).

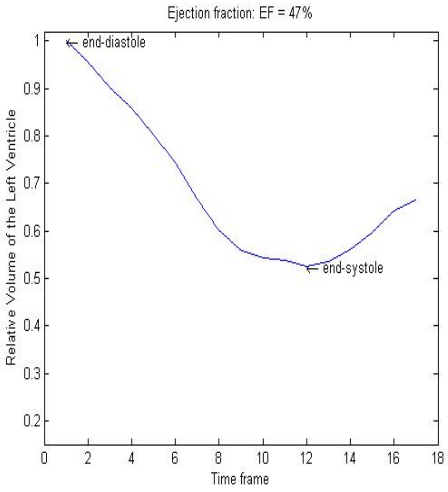

(d) Subject 04, EF = 47% (decreased EF – patient after myocardial infarction).

Figure 3.9: Volume versus time graphs of the examined subjects. In either case, the whole systolic phase and at least part of the diastolic phase of cardiac cycle were analyzed. Segmentations were proceeded in an automated way with corrections in case of the images obtained by the FLASH acquisition sequence (Subject 03 and Subject 04).

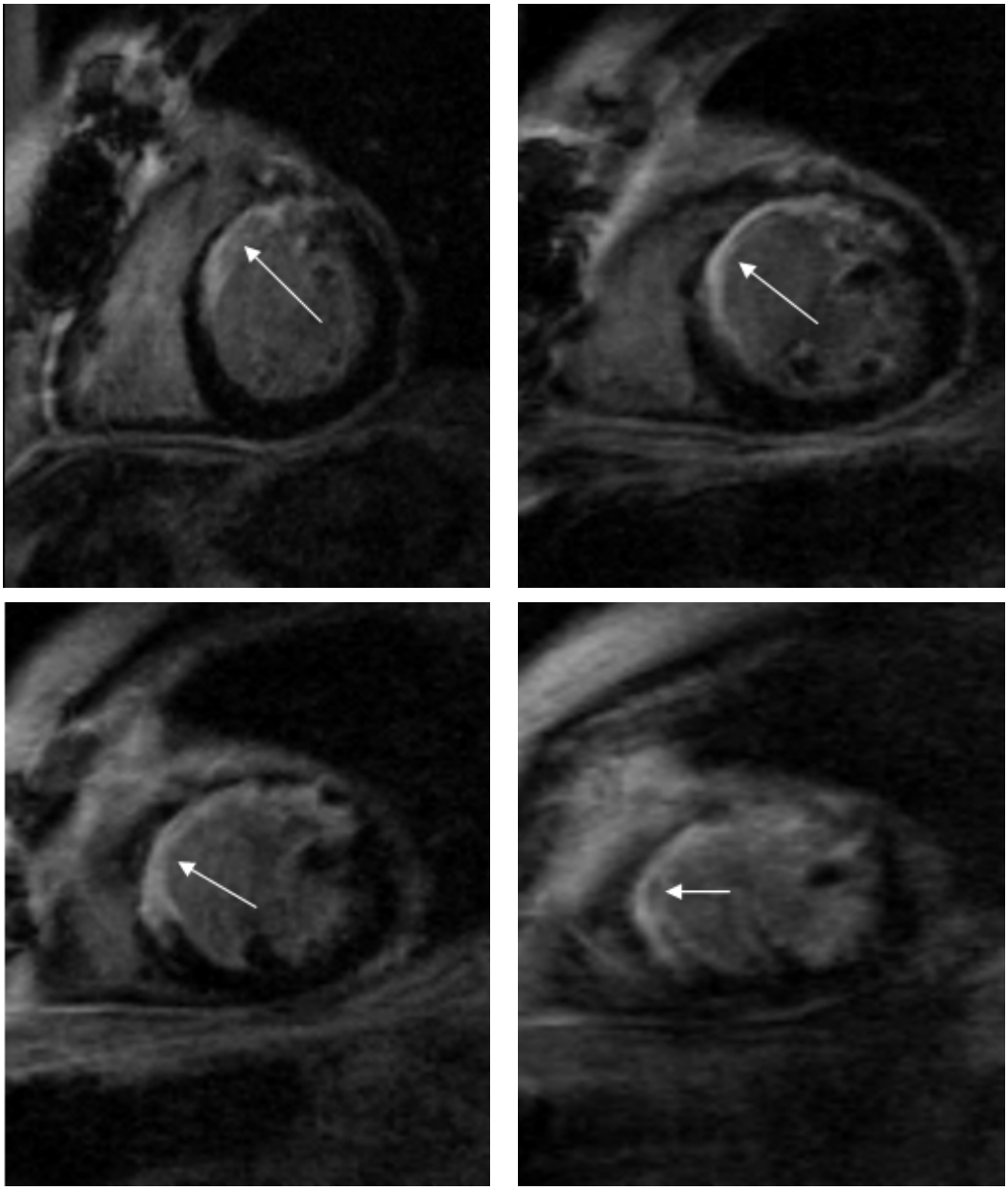

Figure 3.10: **Subject 04.** Late enhancement effect (see Section 1.2) in the anteroseptal segments shows extended nonviable tissue (arrows) as the consequence of myocardial infarction. This is the cause of the local wall thinning and decreased ejection fraction of the left ventricle.

One possibility is to apply directly the algorithm of an automated choice of the initial segmented area p_{ini}, as described in this section. Afterwards, results of the segmentation of the end-systolic and the end-diastolic images are checked and eventually corrected.

More often, we segment these crucial images manually in advance. Number of slices covering the ventricle volume is approximately 10. Fortunately, it is not very high number and we can process all the end-systolic and the end-diastolic time frames manually. These are 2 images in approximately 20 time frames per each slice. The remaining images are segmented in an automated way using the initial segmented area derived from these manually processed images. Table 3.1 shows that for images of high quality the ejection fraction does not differ too much from the exact value obtained by the manual segmentation. This is also depicted in Figure 3.11 for a patient denoted as Subject 02.

Table 3.1: Comparison of the ejection fraction estimated by a fully automatic access and by manual segmentation of the end-diastolic and the end-systolic volumes of the ventricle (evaluated only for the trueFISP data). TF 03 and TF 04 denote two more healthy volunteers that were examined using the trueFISP sequence.

	Fully automatic (EF)	Manual (EF)	Remark
Subject 01	62%	69%	Patient
Subject 02	64%	65%	Patient
TF 03	58%	58%	Healthy volunteer
TF 04	62%	67%	Healthy volunteer

Due to this strategy for processing of the image data, we give to clinical physicians the accurate value of the ejection fraction and a very probable estimate of the volume versus time graph as an additional information.

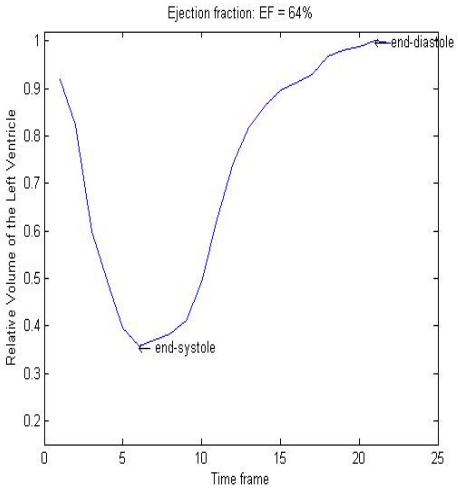

(a) Fully automatic access.

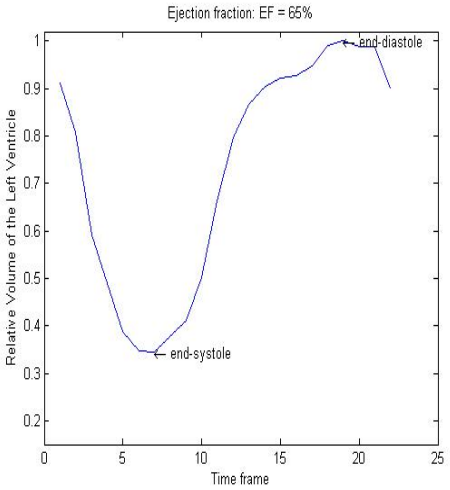

(b) Manual segmentation of the end-diastolic volume and the end-systolic volume, remaining images segmented in an automated way.

Figure 3.11: **Subject 02.** Volume versus time graphs estimated applying fully automated access for the image segmentation (a) or manual segmentation of the end-diastolic and the end-systolic volumes (b). Calculated ejection fractions are 64% in case (a) and 65% in (b).

3.2 Segmentation of the wall of the left heart ventricle

We segment the wall of the left heart ventricle, so that local parameters of the wall thickening during heart contraction can be estimated. In this section we process only the trueFISP data, since the signal inhomogeneities in the wall of the FLASH image data make the algorithm less effective.

The segmented wall is given by the intersection of the areas with the boundaries given by the inner and the outer contour of the ventricle (see Figure 1.7(b)). Both areas have to be estimated. Next, we deal with the segmentation of these areas.

Detection of the inner contour of the ventricle
For detection of the inner contour of the ventricle in the slices corresponding to the base or the apex of the heart (where papillary muscles are absent), we use directly result of the ventricle volume segmentation from Section 3.1. This access cannot be used in the mid-cavity slices, since the papillary muscles are situated inside this part of the ventricle[4] and they were excluded from the segmentation of the heart ventricle volume. Now, the papillary muscles have to be included into the segmented area. For this, the following scheme is applied.

We use the initial segmented area p_{ini} covering the whole ventricle volume. It is derived from the neighbouring segmented area which is slightly expanded, so that it covers the whole ventricle volume. Then the segmented area shrinks (according to the equation (2.3) with the external force $F < 0$), so that the inner contour of the ventricle is detected (see Figure 3.12).

Unfortunately, after a slight expansion of the initial segmented area we could have difficulties with detection of the inner contour of the ventricle. The outer contour may be detected instead of the inner one (especially in patients with wall thinning, e.g. after myocardial infarction). In Section 3.3 we describe a problem of the differentiation of the papillary muscles during the heart contraction when they fuse with the contracted myocardium. The proper detection is often impossible in an automated way. Both these problems are difficult to solve generally for each examined subject. Usually, manual correction are necessary.

Detection of the outer contour of the ventricle
In the previous step, the whole ventricle cavity (including the papillary muscles) was segmented. By slight expansion of this segmented area we obtain the initial segmented area p_{ini} for the segmentation of the outer contour of the ventricle

[4]See Section 1.3 and Figure 1.4.

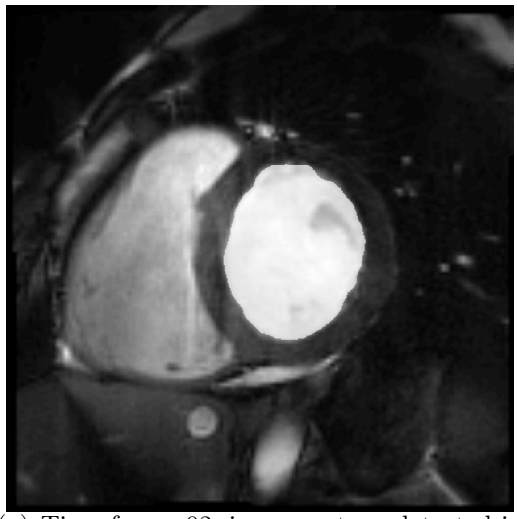

(a) Time frame 02, inner contour detected in a previous segmentation step.

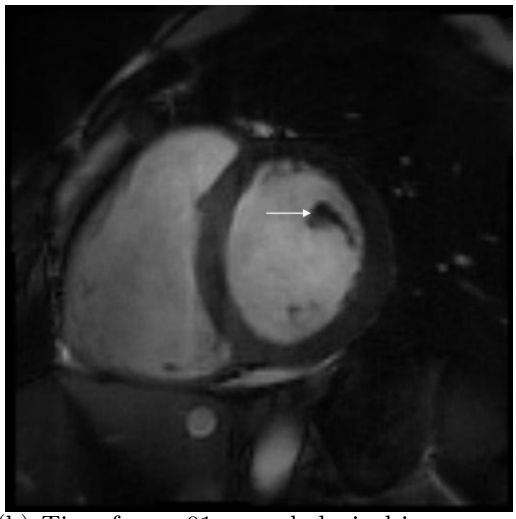

(b) Time frame 01, morphological image, anterior papillary muscle marked with an arrow.

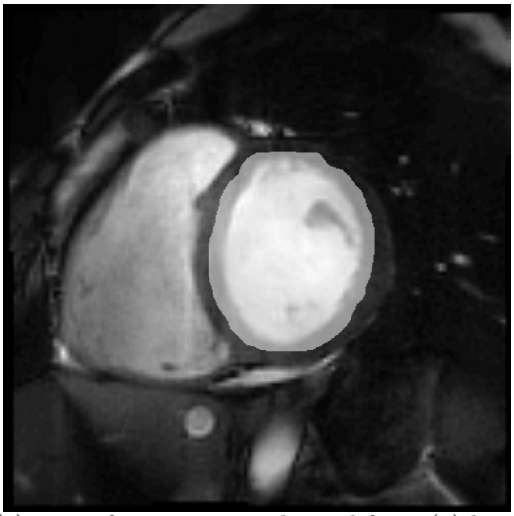

(c) Time frame 01, p_{ini} derived from (a) by a slight expansion of the segmented area.

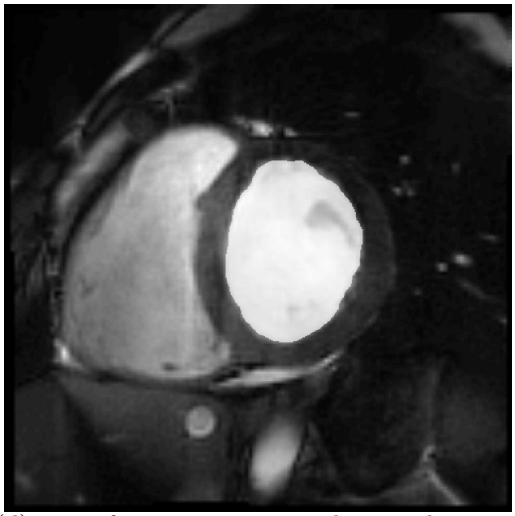

(d) Time frame 01, segmented ventricle cavity (papillary muscles included).

Figure 3.12: **Subject 05.** Detection of the inner contour of the ventricle in Time frame 01. Initial segmented area p_{ini} is derived from the neighbouring time frame image and covers the whole ventricle volume. It shrinks to the inner contour of the ventricle. Parameters of equation (2.3): $\xi = 0.09$, $\lambda = 6$, $F = -1$, time step $\tau = 0.005$. Maximal number of time iterations: 1000 (according to Section 2.7.3).

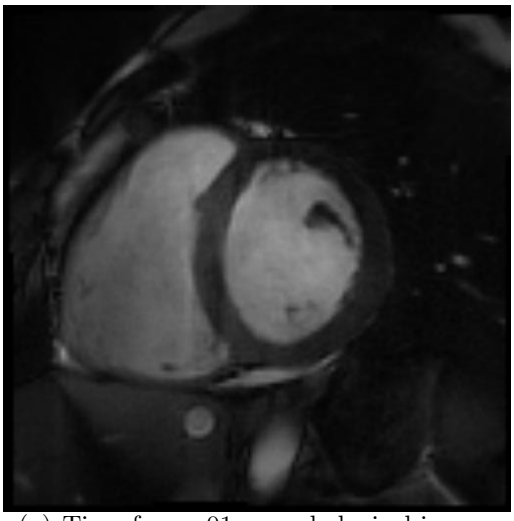

(a) Time frame 01, morphological image.

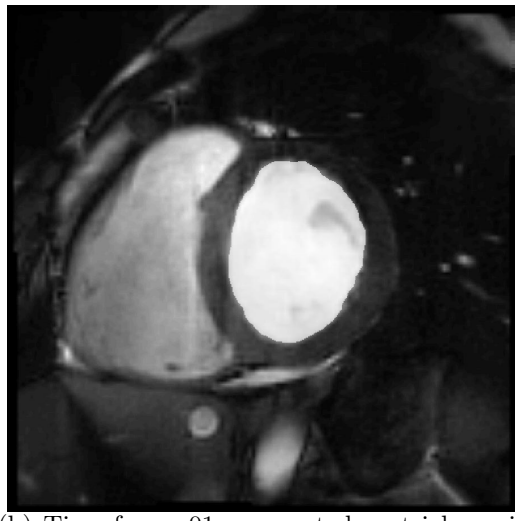

(b) Time frame 01, segmented ventricle cavity.

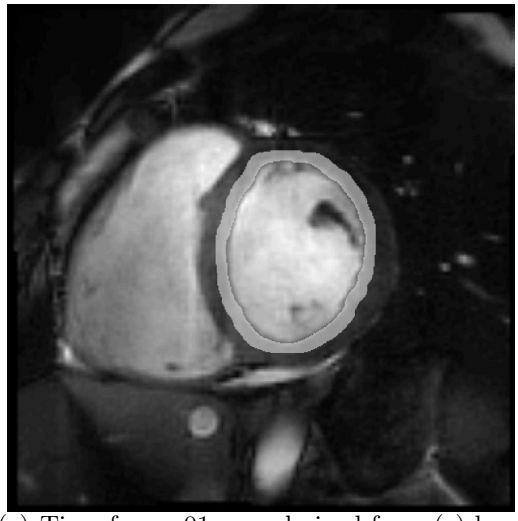

(c) Time frame 01, p_{ini} derived from (c) by a slight expansion of the segmented area.

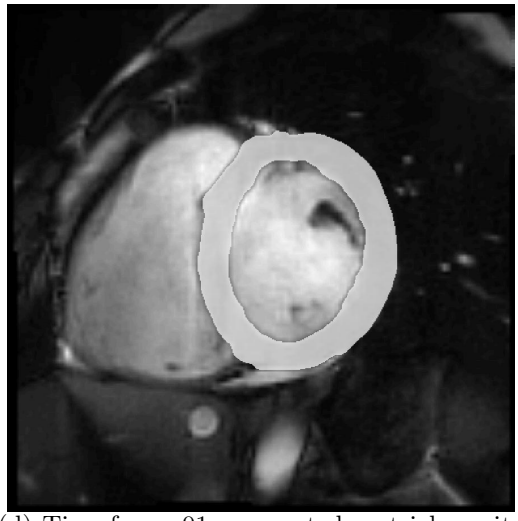

(d) Time frame 01, segmented ventricle cavity (papillary muscles included).

Figure 3.13: **Subject 05.** The outer contour detection and the wall segmentation. Initial segmented area p_{ini} is derived from the segmented ventricle cavity. We fix $p(t,x) = 0$ inside the cavity. Parameters of equation (2.3): $\xi = 0.09$, $\lambda = 6$ and $F = 1$ for first 500 iterations, $\lambda = 60$ and $F = 0.5$ for subsequent iterations, time step $\tau = 0.005$. Maximal number of time iterations: 1000 (according to Section 2.7.3).

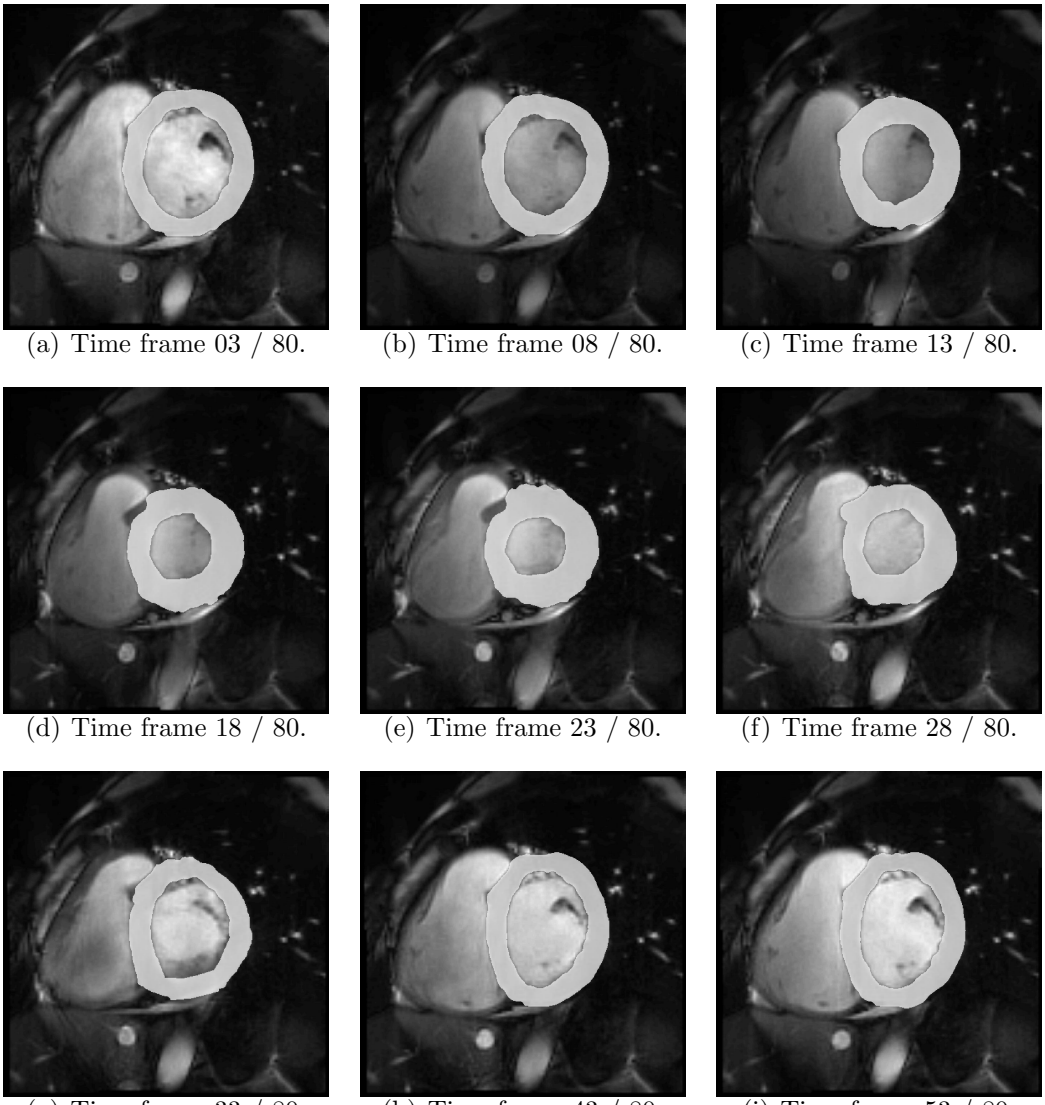

(a) Time frame 03 / 80. (b) Time frame 08 / 80. (c) Time frame 13 / 80.

(d) Time frame 18 / 80. (e) Time frame 23 / 80. (f) Time frame 28 / 80.

(g) Time frame 33 / 80. (h) Time frame 43 / 80. (i) Time frame 53 / 80.

Figure 3.14: **Subject 05.** Image data acquired with high temporal resolution (80 time frame images per single cardiac cycle – corresponding approximately to a temporal resolution of 15ms per a time frame). Selected images of one mid-cavity slice in through the cardiac cycle with the segmented wall of the left ventricle. Parameters of equation (2.3) are the same as in Figure 3.13.

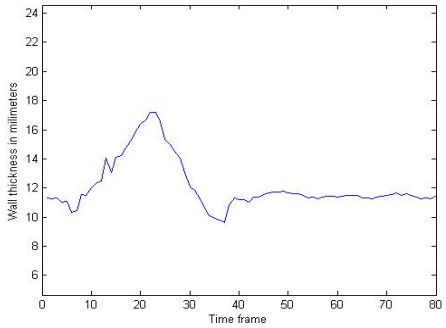

(a) Segment 07 (mid anterior).

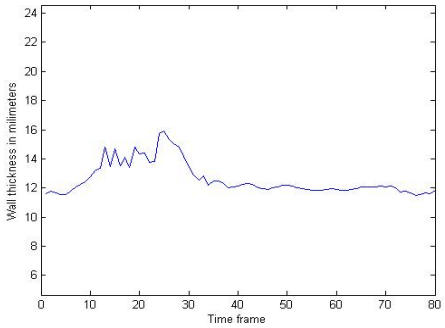

(b) Segment 08 (mid anteroseptal).

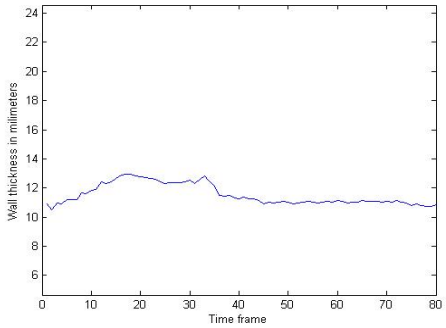

(c) Segment 09 (mid inferoseptal).

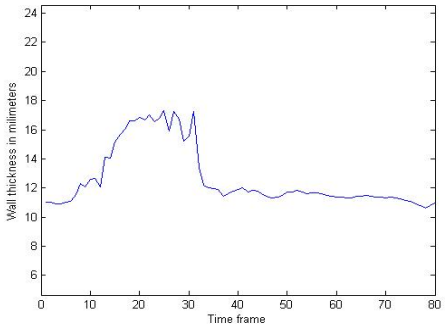

(d) Segment 10 (mid inferior).

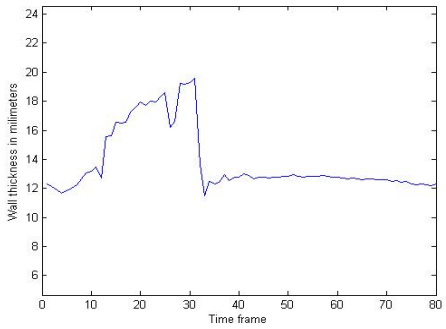

(e) Segment 11 (mid inferolateral).

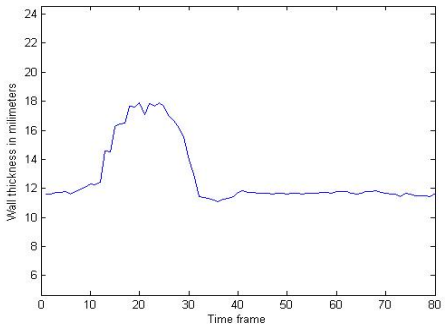

(f) Segment 12 (mid anterolateral).

Figure 3.15: **Subject 05.** Wall thickness versus time graphs for the slice depicted in Figure 3.14 The ventricle is divided into the segments according to American Heart Association (see Figure 1.9). Presented graphs depict local kinetic properties of the myocardium (radial thickening of the wall greater than 30% stands for normokinetic myocardium, see Section 1.4). High temporal resolution makes possible to record timing of the contraction of heart myocardial segment (it may show e.g. local delay in the contraction due to conductive pathway diseases).

(see Figure 2.1(b)). Then the area is evolving under the equation (2.3) with the parameter $F > 0$. We fix $p(t, x) = 0$ inside the ventricle cavity, so that the finally the wall of the ventricle is segmented (see Figure 3.13).

Analysis of the image data in real clinical examinations
In a similar way as in ejection fraction estimation in Section 3.1 we combine both, manual and automated access to the problem of estimation of the parameters of the wall thickening during the heart contraction. The inner contour of the ventricle in the slices with the papillary muscles usually has to be segmented manually. Other segmentations are proceeded automatically but with the checking afterwards. Number of manual corrections depends on the quality of the image data. Using up-to-date MR sequences for examination of the heart dynamics (such as the trueFISP sequence), with sufficient quality of the input data from the examined subject, the speed-up of the processing in comparison with a fully manual access is significant. Figures 3.14 and 3.16 show images with the segmented wall of the ventricle during the heart contraction, Figures 3.15, 3.17, 3.18 and 3.19 depict radial thickening of the ventricle wall during the contraction estimated from the segmented images of the examined subjects. Finally, Figure 3.20 compares the wall thickness in a single examined subject between two subsequent examination.

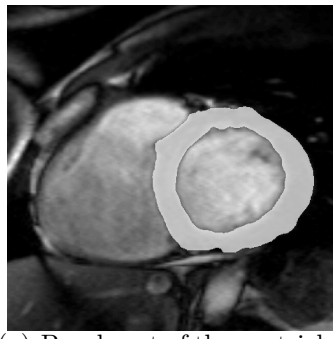

(a) Basal part of the ventricle, Time frame 01 (end-diastole).

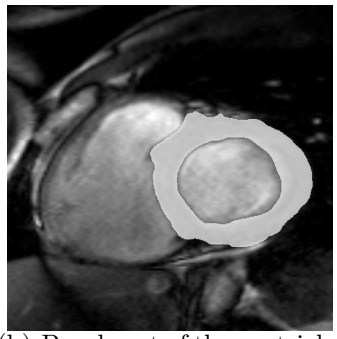

(b) Basal part of the ventricle, Time frame 03.

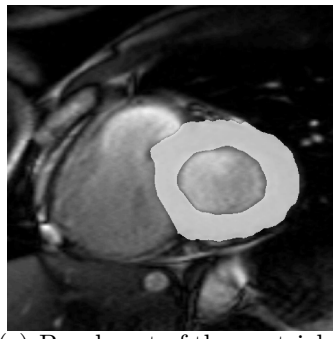

(c) Basal part of the ventricle, Time frame 05 (end-systole).

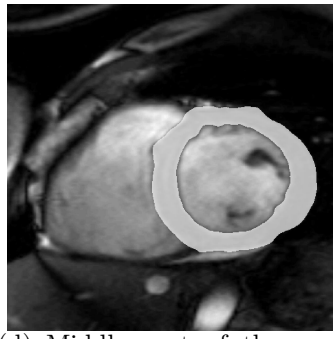

(d) Middle part of the ventricle, Time frame 01 (end-diastole).

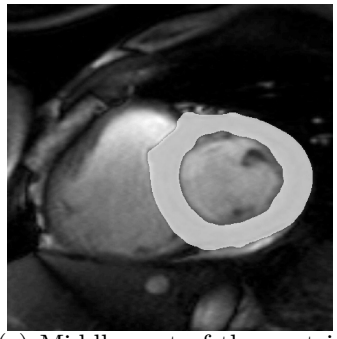

(e) Middle part of the ventricle, Time frame 03.

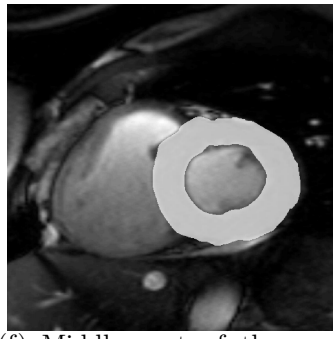

(f) Middle part of the ventricle, Time frame 05 (end-systole).

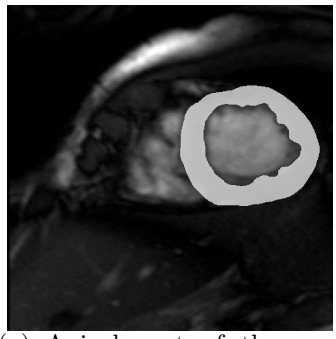

(g) Apical part of the ventricle, Time frame 01 (end-diastole).

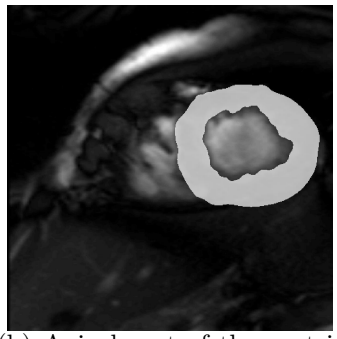

(h) Apical part of the ventricle, Time frame 03.

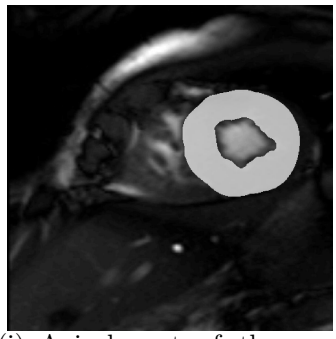

(i) Apical part of the ventricle, Time frame 05 (end-systole).

Figure 3.16: **Subject 06.** Selected images from the systolic phase of the cardiac cycle. Parameters of equation (2.3) are the same as in Figure 3.13.

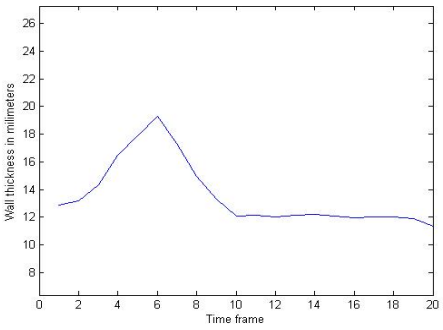

(a) Segment 01 (basal anterior).

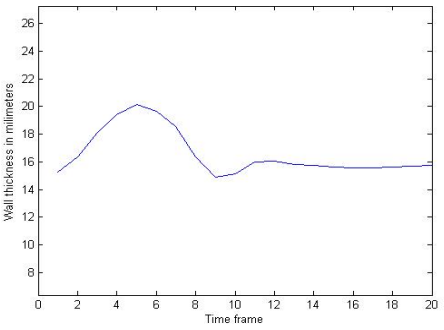

(b) Segment 02 (basal anteroseptal).

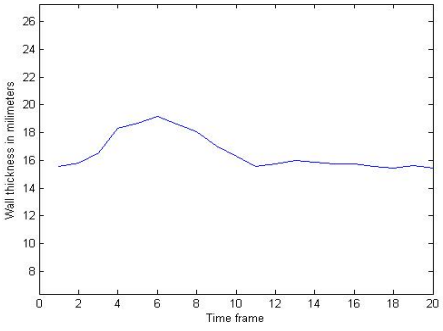

(c) Segment 03 (basal inferoseptal).

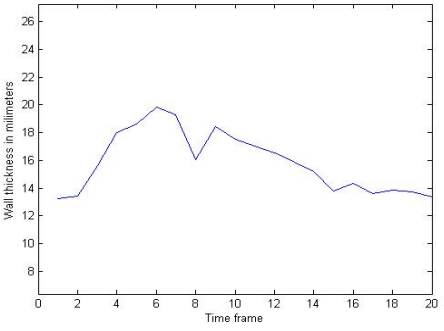

(d) Segment 04 (basal inferior).

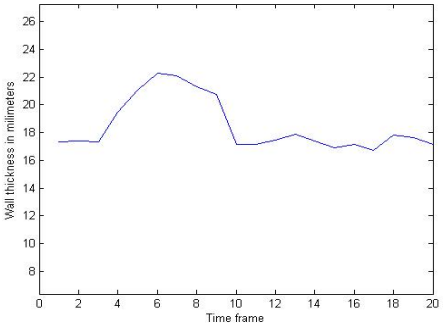

(e) Segment 05 (basal inferolateral).

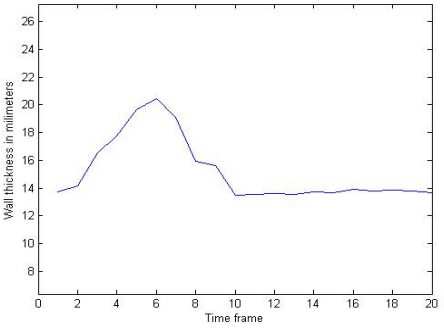

(f) Segment 06 (basal anterolateral).

Figure 3.17: **Subject 06.** Wall thickness versus time graphs in a basal part of the heart corresponding to images in Figures 3.16 (a)-(c). The ventricle is divided into the segments according to American Heart Association (see Figure 1.9).

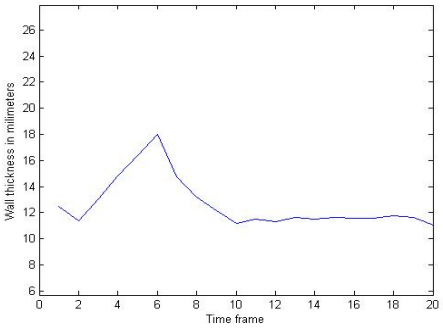

(a) Segment 07 (mid anterior).

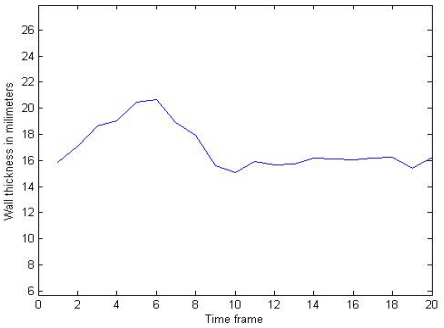

(b) Segment 08 (mid anteroseptal).

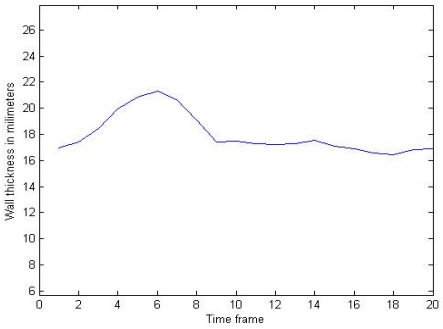

(c) Segment 09 (mid inferoseptal).

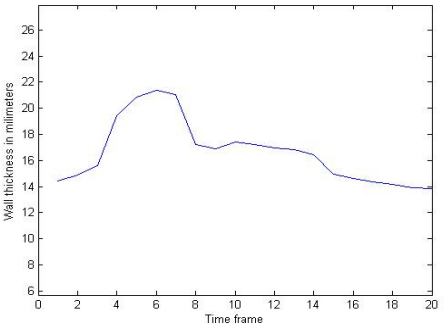

(d) Segment 10 (mid inferior).

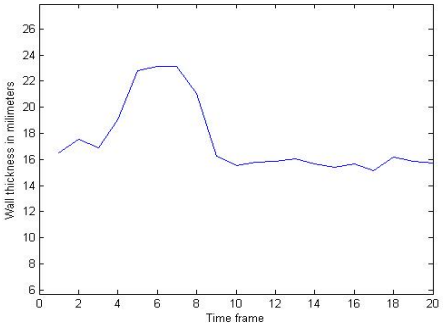

(e) Segment 11 (mid inferolateral).

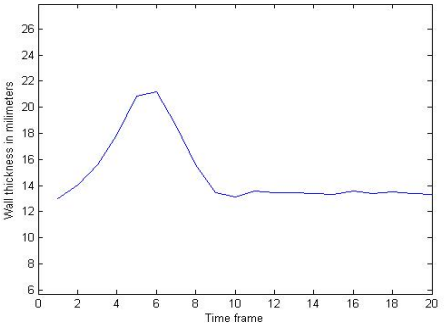

(f) Segment 12 (mid anterolateral).

Figure 3.18: **Subject 06.** Wall thickness versus time graphs in a middle part of the heart from Figures 3.16 (d)-(f). The ventricle is divided into the segments according to American Heart Association (see Figure 1.9).

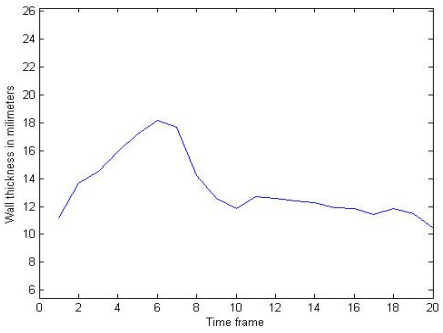

(a) Segment 13 (apical anterior).

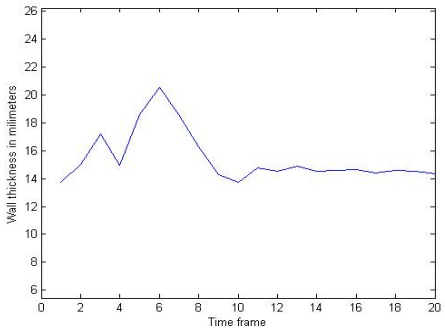

(b) Segment 14 (apical septal).

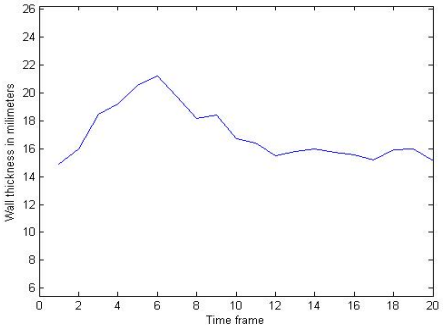

(c) Segment 15 (apical inferior).

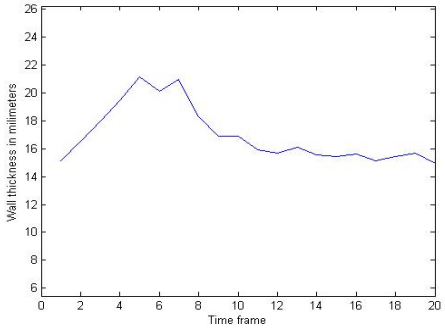

(d) Segment 16 (apical lateral).

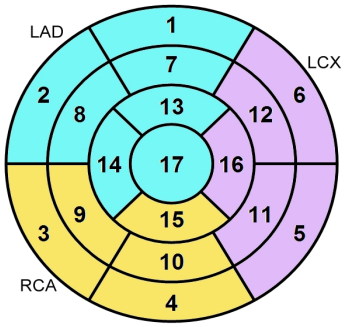

(e) 'Bull eye'.

Figure 3.19: **Subject 06.** Wall thickness versus time graphs in a basal part of the heart from Figures 3.16 (g)-(i). The ventricle is divided into the segments according to American Heart Association (see (e) and Figure 1.9).

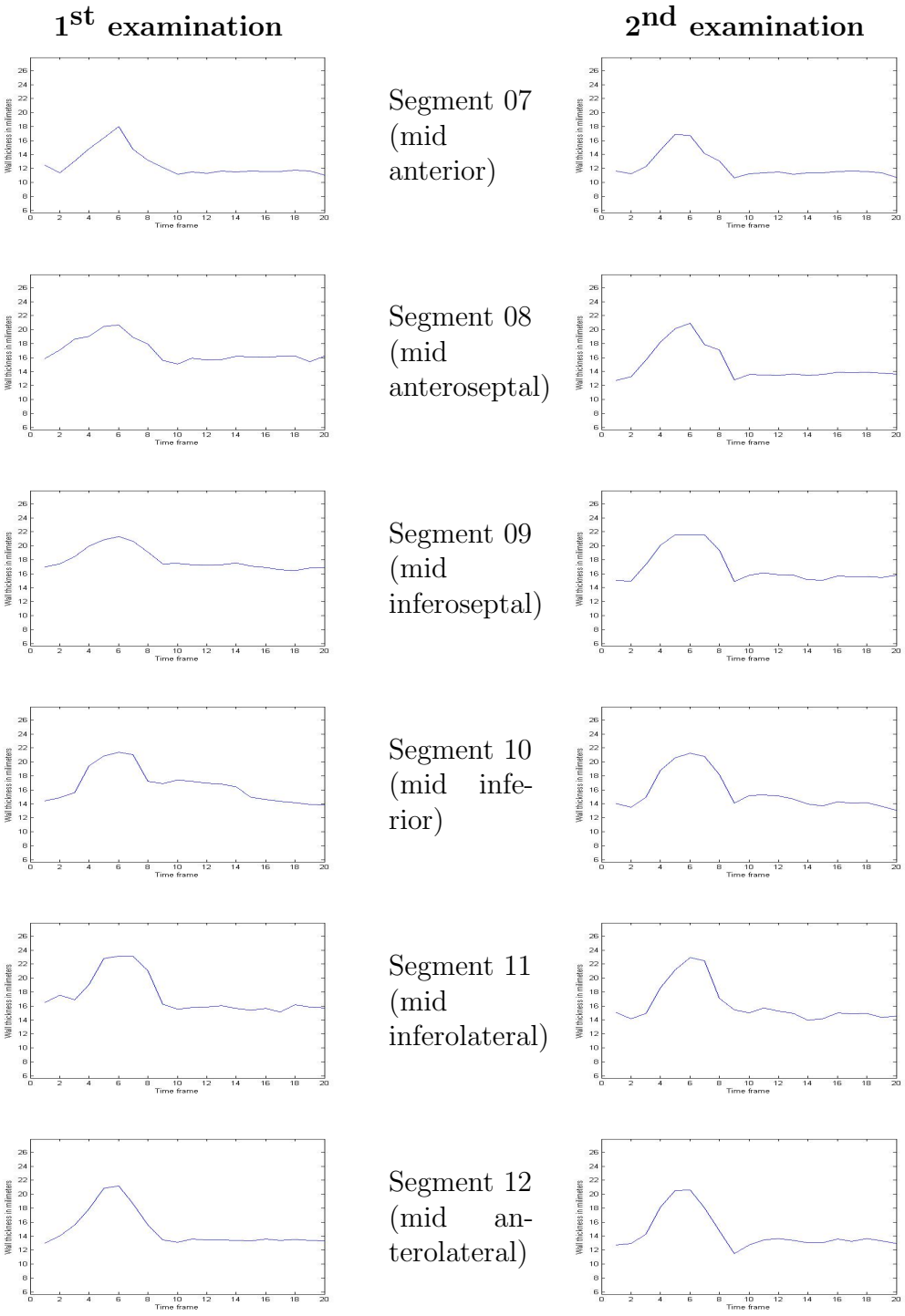

Figure 3.20: **Subject 06.** Comparison of wall thickness versus time graphs corresponding to the mid-cavity segments of the heart in two subsequent examinations. Progress of the disease may be described by the parameters of wall thickening.

3.3 Segmentation difficulties

In this section we deal with some difficulties in the automated segmentation of the cardiac MR images. They are given by technical problems of the data acquisition, due to clinical status and co-operativity of the examined subject and finally due to intrinsic anatomical facts. We refer to the results and figures from the previous section to demonstrate the difficulties.

The quality of acquired data can be evaluated with such indices as signal-to-noise or contrast-to-noise ratio. In Section 1.2 we noted that usually two types of imaging sequences are used for dynamic examination of the heart using magnetic resonance imaging – the FLASH and the trueFISP sequences. Although the efficiency of the segmentation process was much better using the input data of the up-to-date trueFISP imaging sequence, even the FLASH data may be satisfactory for the segmentation of the ventricle volume.

Both sequences are triggered by the electrocardiogram (ECG) or the peripheral pulse of the examined subject. Some of the patients have irregularities in the cardiac rhythmicity (arrhythmias). This causes the triggering to be not optimal and negatively influences the quality of images.

The data are acquired during a breath-hold period. Clinical status (and sometimes even bad co-operativity) of patients does not allow for longer breathless period. This adds motion artifacts into the images. The clinical interpretation of such images is difficult (and sometimes even impossible). The breath-hold period can be shortened but subsequently with worse temporal or spatial resolution of the images. New MRI techniques for image acquisition using breath navigator remove this difficulty.

Restricted temporal resolution causes image blurring during the period of the fastest part of the ventricle contraction. The inner contour of the ventricle is indistinguishable even for a naked eye (see Figure 1.3). Using the stopping criterion according to Section 2.7.3 (not extremely strict criterion with the specified maximal number of iteration), we usually obtain satisfactory results.

Finally, we mention intrinsic anatomical facts that complicate the segmentation process. In the mid-cavity slices, part of the ventricle volume is occupied by the papillary muscles (see Section 1.3 and Figure 1.5). In principle, one has to decide which type of the inner contour should be taken (see Figure 1.7). In Figure 3.22 we can see the segmentation including or excluding the papillary muscles. Usually, one can exclude papillary muscles from the resulted ventricle volume segmentation and also from the ventricle wall segment. The problem is that although the papillary muscles are easy to distinguish in the end-diastolic scans, it is sometimes impossible to distinguish them in the scans from the contracted heart since the muscles are attached to the ventricle wall (see Figure 3.21).

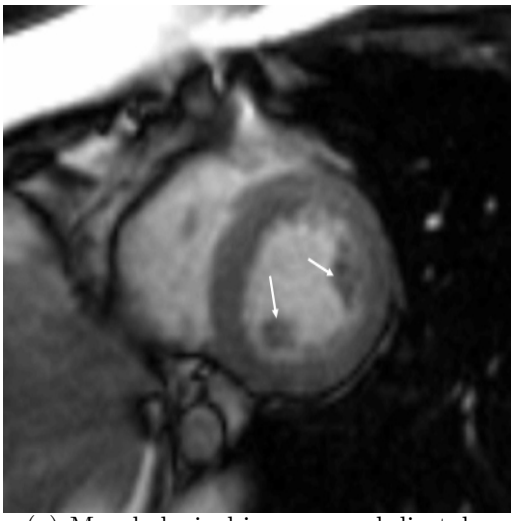

(a) Morphological image – end-diastole.

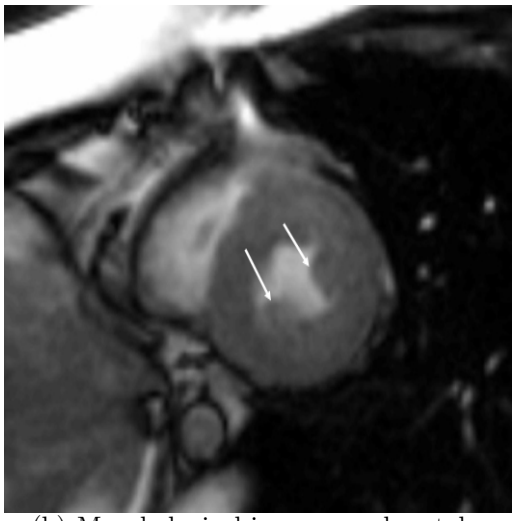

(b) Morphological image – end-systole.

Figure 3.21: In end-diastolic images the papillary muscles can be distinguished in the ventricle volume as two oval elements close to the ventricle wall (arrows). In the systolic images the papillary muscles are attached to the ventricle wall.

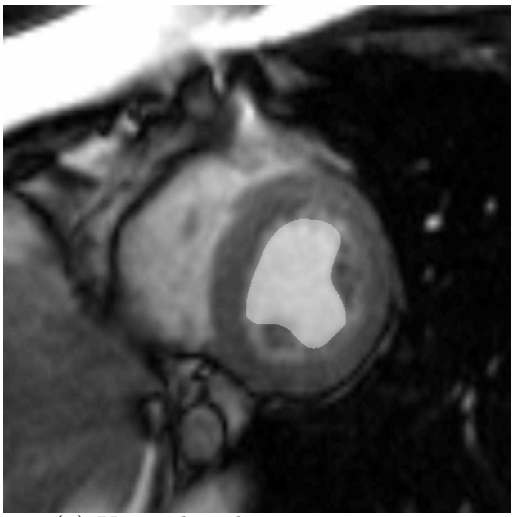

(a) Ventricle volume segmentation.

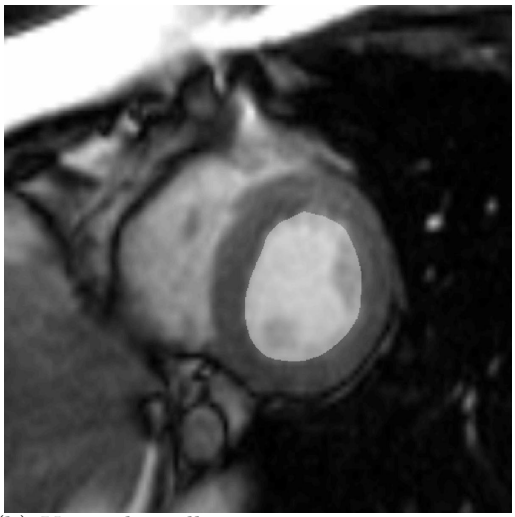

(b) Ventricle wall segmentation – estimation of the inner contour.

Figure 3.22: In case of the ventricle volume segmentation, papillary muscles should be excluded. In case of the segmentation of the ventricle wall, papillary muscles have to become parts of the segmented area.

For marking of the outer contour of the ventricle there may be difficulties in the contrast between the wall and the surrounded tissue. There is an excellent contrast between the myocardium and the lung tissue (black area around the heart). On the other hand, it is more difficult to distinguish between myocardial and hepatic tissue (on the inferior wall of the heart) or the junction of left and right ventricle.

Concerning our algorithm, it is successful in the estimation of the outer contour of the ventricle. Usually problems with the papillary muscles in the middle slices have to be corrected manually.

Chapter 4

Discussion and Conclusion

4.1 Discussion

The segmentation algorithm was applied to the real images of the heart acquired by magnetic resonance imaging. We attempted to segment left heart ventricle volume and the ventricle wall in an automated way.

The cardiac MRI data (CINE sequence) are not true three-dimensional data, since the position of the neighbouring slices are not exactly matching. It is caused by the fact, that data from different slices are acquired in different breath-hold periods of an examined subject and the breath-holds are not absolutely reproducible. Therefore, a fully three-dimensional access is not directly applicable for our cardiac MR images and we solve a two-dimensional problem for each slice separately.

We applied the algorithm to image data obtained using two MR acquisition sequences – the FLASH and the trueFISP (see Section 1.2). Automated data analysis of the healthy volunteers were successful with minimal manual corrections (due to an excellent quality of images). Unfortunately, cardiac patients who are examined at MRI departments have usually serious heart pathology. As we described in Section 3.3, the quality of the acquired images is lower and makes the automated process to be less stable. Manual corrections are necessary, as we presented in the previous chapter.

Concerning the segmentation of the ventricle volume, it was possible to successfully segment both types of data (the FLASH and the trueFISP) although the efficiency of the automated process for the FLASH data was limiting. Data acquired using the up-to-date trueFISP imaging sequence were analyzed with better results (in some cases, no manual corrections were necessary). It is due to a higher signal-to-noise ratio and better signal homogeneity of the flowing blood inside the ventricle (see Figure 1.3).

Segmentation of the wall of the left ventricle is a more difficult problem.

Concerning the detection of the outer contour of ventricle, the signal inhomogeneity of the ventricle wall in the FLASH data does not make possible to use the presented algorithm for the successful automated segmentation of the wall in this kind of images. Therefore, we processed only the trueFISP data.

For the wall segmentation, both the outer and the inner contour of the ventricle have to be detected. Our segmentation model does not make possible to differentiate the papillary muscles in the mid-cavity slices of the ventricle during the contraction (see Section 3.3). Since the papillary muscles have to be excluded from the segmented wall, it is usually necessary to segment the inner contour in these slices manually.

In our work we also dealt with non-constant choice of parameters λ and F in the equation (2.3). We tried to choose these parameters with respect to the non-constant signal-to-noise ratio in the images. We prefer data acquisition with the quality as high as possible. In the application, especially modification in non-constant F is necessary.

Choice of the stopping time of the evolution depends on other parameters of equation (2.3) (namely λ, F, ξ, h, τ). Usual approach is to terminate the evolution when the change of the segmentation function p is below a specified threshold. Due to many irregularities in our images we choose a less strict stopping criterion – evaluating only the area of the segmented object and ceasing the process when the change of the area is below a specified threshold. We prevent extremely long evolution using a fixed maximal number of time iteration. This number is estimated in the assisted segmentation of the first image and then used for automated segmentation of all other images in the examination.

4.2 Conclusion

Cardiac MRI data segmentation is an important part of the MR data post-processing. In our case number of acquired images from single examination exceeds 200. This number is too high to segment all the images manually. However, the data character of cardiac MR images (such as limited signal-to-noise and contrast-to-noise ratio, motion and pulsation artifacts) makes the automated segmentation to be a rather difficult task.

In the presented work we adapted the segmentation model described in [4] to the problem of cardiac MRI data segmentation. The advantage of the algorithm is a well reasoned segmentation scheme due to mathematical analysis of the governing equation.

In the work we have achieved to adapt the segmentation model for:

- Estimation of the volume of the ventricle during the whole cardiac cycle

with subsequent estimation of the ejection fraction of the left heart ventricle.

- Detection of the inner contour of the ventricle wall in the slices where the papillary muscles are absent (slices corresponding to the basal and apical part of the heart). Manual corrections are necessary in the mid-cavity slices.

- Detection of the outer contour of the ventricle wall (after manual or automated detection of the inner contour) in majority of slices with subsequent estimation of parameters of wall thickening during the heart contraction.

An algorithm for medical data segmentation has to be successful in detection of objects in the image and also it has to be fast enough, so that physicians would benefit from its usage. On a standard 2GHz PC, our algorithm segments the ventricle volume in one image in about 20 seconds[1]. It is certain that, there is available software for an image segmentation that offers good results even in a shorter time. Unfortunately, all the algorithms have some problems with the analysis of real patients data. Our algorithm also has difficulties with automated segmentation of some images. On the other hand, we have shown that even the presented segmentation model can be used for this task and with eventual combination with some other techniques, it may become efficient.

In future new techniques in magnetic resonance imaging will certainly make possible to get cardiac MR dynamic images with better spatial and temporal resolution. These images might improve the diagnostic possibilities. For example cardiac pathologies could be better localized or the heart function (dysfunction) could be better described using cardiac stress–strain model, fluid–structure interaction, etc. The description as accurate as possible is important for the indication of proper treatment modalities. Number of commonly acquired images from a single examination with better resolution may rise to thousands. Then an automation of the procedure of the heart segmentation will be a fundamental part of data acquisition.

Finally, we can conclude that we adapted the segmentation scheme from [4] to the problem of cardiac MRI data evaluation and presented the model to a people working on image processing in fields of magnetic resonance imaging. The segmentation algorithm is efficient in automated segmentation of the heart ventricle volumes and wall of the left heart ventricle (with eventual minor manual correction). The goal of the work is an automatic algorithm for image processing helpful in clinical examinations.

[1]Using the numerical grid with 300 x 300 degrees of freedom, time step $\tau = 0.005$, 300 time iterations.

Bibliography

[1] Allen S. and Cahn J.: *A Microscopic Theory for Antiphase Boundary Motion and its Application to Antiphase Domain Coarsening*, Acta Metall. 27, (1979) 1084-1095.

[2] Aubert G., Kornprobst P.: *Mathematical problems in image processing*, Springer-Verlag, New York, 2002.

[3] Beneš M.: *Diffuse-interface treatment of the anisotropic mean–curvature flow*, Appl. Math. 48 (6) (2003) 437-453.

[4] Beneš M., Chalupecký V., Mikula K.: *Geometrical image segmentation by the Allen-Cahn equation*, Applied Numerical Mathematics 51 (2) (2004) 187-205.

[5] Beneš M. and Mikula K.: *Simulation of anisotropic motion by mean curvature – comparison of phase field and sharp interface approaches*, Acta Math. Univ. Comenianae Vol. LXVII, 1(1998), 17-42.

[6] Beneš M.: *Phase–field model of of microstructure growth in solidification of pure substances*, PhD thesis, Faculty of Nuclear Sciences and Physical Engineering , Czech Technical University in Prague, 1997.

[7] Beneš M.: *Numerical Simulation of Microstructure Growth in Solidification*, Habilitation Thesis, Faculty of Nuclear Sciences and Physical Engineering, Czech Technical University in Prague, 2002 (in Czech).

[8] Bernstein M. A., King K. F., Zhou X. J.: *Handbook of MRI pulse sequences*, Elsevier Inc., 2004.

[9] Bogaert J., Dymarkowski S., Taylor A. M.: *Clinical cardiac MRI*, Springer-Verlag, Berlin Heidelberg, 2005.

[10] Cerqueira M. D., Weissman N. J., Dilsizian V. et al.: *Standardized myocardial segmentation and nomenclature for tomographic imaging of the heart: A statement of healthcare professionals from the Cardiac Imaging Comittee*

of the Council on Clinical Cardiology of the American Heart Association, Circulation 105 (2002) 539-542.

[11] Chabiniok R., Tintěra J.: *Cardiac MRI data segmentation using the partial differential equation of Allen–Cahn type*: Proceedings of the Czech—Japanese Seminar in Applied Mathematics 2006, Czech Technical University in Prague, September 14-17, 2006 (in press).

[12] El-Berbari R., Kachenoura N., Redheuil A., Block I., Mousseaux E., Frouin F.: *Using cine MR images to evaluate myocardial infarct transmurality on delayed enhancement images*, Biomedical Imaging: Macro to Nano, 3rd IEEE International Symposium, April 6-9, 2006, pp. 145 - 148.

[13] Kufner A., John O. and Fučík S.: *Functional spaces*, Academia Prague, Prague 1977.

[14] Grisvard P.: *Elliptic problems in nonsmooth domains*, Pitman, Boston, 1985.

[15] Guyton A. C., Hall E. H.: *Textbook of medical physiology,* 10^{th} *ed.*, W. B. Saunders Company, 2000.

[16] http://www.ikem.cz/

[17] Junqueira L. C., Carneiro J., Carneiro J.: *Basic histology,* 11^{th} *ed.*, McGraw-Hill Companies, 2005.

[18] Liang Z., Lauterbur P. C.: *Principles of magnetic resonance imaging*, Institute of Electrical and Eloctronics Engineers, Inc. 3 Park Avenue, New York, 2000.

[19] Lions J. L.: *Quelques Méthodes aux Résolution des Problèmes Nonlinéaires*, Dunod GauthiersVillars, Paris, 1969.

[20] Martini F. : *Fundamentals of Anatomy and Physiology*, Benjamin Cummings, 2005.

[21] Mikula K., Sarti A., Sgallari F.: *Co-volume level set method in subjective surface based medical image segmentation*, book chapter in *Handbook of Medical Image Analysis: Segmentation and Registration Models*, (J.Suri et al., Eds.), Springer, New York, 2005, pp. 583-626.

[22] Osher S., Fedkiw R.: *Level set methods and dynamic implicit surfaces*, Springer Verlag, New York, 2003.

[23] Perona P., Malik J.: *Scale space and edge detection using anisotropic diffusion*, IEEE Trans. Pattern Anal. Mach. Intell. 12 (1990) 629-639.

[24] Pratt W. K.: *Digital image processing (3rd ed.)*, John Wiley, New York, 2001.

[25] Roubíček T.: *A generalization of the Lions–Temam compact imbedding theorem*, Čas. Pěst. Matem. 115 (1990) 338-342.

[26] Roubíček T.: *Nonlinear partial differential equations with applications*, Birkhäuser Verlag, Basel 2005.

[27] Russ J.C.: *The image processing handbook,* 3^{rd} *ed.*,CRC Press LLC, 1999. New York, 2003.

[28] Sainte-Marie J., Chapelle D., Cimrman R., Sorine M.: *Modeling and estimation of the cardiac electromechanical activity*, Computer and Structures 84 (2006) 1743-1759.

[29] Zhao H.K., Osher S., Chan T., Merriman B.: *A variational level set approach to multiphase motion*, J. Comput. Phys. 127 (1996) 179–195.